Atomic Physics of Hot Plasmas

Rolf Mewe

Space Research Organization Netherlands (SRON), Sorbonnelaan 2,
NL-3584 CA Utrecht, The Netherlands

Abstract. Plasma with temperatures above a million Kelvin is common in the Universe. It exists for a large part in the intergalactic space, but is also found in a variety of sources which range from optically thin to optically thick. X-ray spectral modeling is an important tool to study the physical parameters of such hot plasmas. In this paper the general procedure of such a modeling is briefly considered and various processes that generate X rays in hot cosmic plasmas are reviewed. Several plasma models, such as the coronal, nebular, and optically thick models are discussed with emphasis on the optically thin coronal model. Various effects of relaxing the restrictions of this model such as those arising from high density, optical depth, and transient ionization are discussed. Most of this paper is dedicated to the atomic physics of calculating X-ray spectra from optically thin plasmas: the ionization balance, the rate coefficients for ionization and recombination, and line excitation, including the formation of dielectronic recombination satellite lines. Finally, the diagnostics of plasma properties such as electron temperature and density, ionization balance, differential emission measure, and non-Maxwellian electron distributions is discussed.

1 Introduction

During the past decades, the results from a sequence of X-ray space missions with ever increasing sensitivity and spectral and spatial resolutions have demonstrated the existence of thermal X-ray emission from hot plasmas above a million Kelvin in a large variety of astrophysical sources including optically thin sources like solar and stellar coronae, clusters of galaxies, supernova remnants, the tenuous intergalactic and interstellar space, and at higher densities also accretion powered sources such as compact X-ray binaries, cataclysmic variables, and active galactic nuclei, where a central X-ray emitting region is surrounded by a cooler medium that is partially photo-ionized.

In modeling these various types of sources, X-ray spectroscopy has proven an invaluable tool. Motivated by the X-ray observations, various authors have developed computer codes in the past in order to explain the observed X-ray emission and to understand the physics of the emitting objects, for optically thin plasmas [e.g., Raymond & Smith 1977 (RS); Mewe & Gronenschild 1981 (MG); Masai 1984; Mewe et al. 1985a; Landini & Monsignori Fossi 1990] or for photo-ionized plasmas (e.g., Kallman& McCray 1982; McCray 1984; see also the Chapter by D. Liedahl).

In part I I consider briefly several thermal and non-thermal processes that can generate X rays in hot plasmas, compare different plasma models, and discuss the general procedure of spectral modeling. I concentrate on the coronal model of a tenuous plasma applicable to hot, optically thin, thermal plasmas in equilibrium. In part II I deal with the basic atomic physics underlying the computation of the ionization balance in a coronal plasma, i.e. the rate coefficients for ionization and recombination. In part III the formation of line and continuum X-ray spectra of optically thin plasmas is considered, in particular the line excitation processes. Finally, part IV deals with the diagnostics of plasma parameters such as electron temperature and density, differential emission measure, and the diagnostics of dielectronic satellite lines including non-Maxwellian electron distributions.[1] Recent reviews on plasma spectroscopy have been given by Kahn & Liedahl (1995), Raymond & Brickhouse (1996), and Griem (1997).

I. X-ray Spectral Modeling of Hot Plasmas

2   Radiation Processes and Plasma Models

In nature, X rays are produced by a variety of processes which may be classified roughly as *thermal* or *non-thermal* processes. The emission mechanisms include blackbody radiation, bremsstrahlung (thermal or nonthermal), line emission, recombination radiation, synchrotron radiation, and inverse Compton radiation (for more details and literature, e.g., Mewe 1992). Observations of certain features of the X-ray flux, such as its spectral energy distribution, emission lines, absorption edges, and degree of polarization, may reveal the dominant emission mechanism in the source. X-ray emission usually results from an electron-photon process. If the energy of the generating electron is thermal in nature, i.e. the electrons are described by a Maxwellian energy distribution characterized by a certain temperature T, we speak of *thermal* processes. Temperatures of a million Kelvin or more are required. The most important processes are line and continuum emission from optically thin plasmas and blackbody radiation from optically thick plasmas. *Nonthermal* radiation is produced when the electrons are non-thermal in nature (e.g., occur in beams). The most important processes for non-thermal X-ray emission in cosmic sources involve the acceleration of (relativistic) electrons in magnetic fields (synchrotron radiation or magnetic bremsstrahlung), and

---

[1] A few useful textbooks for background studies are: Herzberg (1944); Condon & Shortley (1970) [general atomic spectroscopy]; Griem (1997) [plasma spectroscopy]; Kahn & Liedahl (1995); Raymond & Brickhouse (1996), and Peacock (1996) [review articles on plasma spectroscopy]; and Pal'chikov & Shevelko (1995) [atomic data on highly ionized atoms].

the interaction of energetic electrons with visible, infrared, or microwave photons (inverse Compton radiation), or the production of bremsstrahlung and line emission by the deceleration of electron beams as a result of Coulomb interaction with ions in solar and stellar flare plasmas (cf. the Chapters by Longair, and Liedahl).

All processes are given in Table 1 of Mewe (1992), together with examples of the cosmic sources in which they occur, but here we summarize only the radiation processes in optically thin plasmas (such as stellar coronae, supernova remnants, hot interstellar matter, intra-cluster gas, normal galaxies and galactic halos). Note that the first two processes are usually the most important ones.

- Thermal bremsstrahlung continuum produced by a transition of a free plasma electron between two continuum states above the ionization limit of the ion: energy spectrum $\propto T^{-\frac{1}{2}}e^{-E/kT}$. Dominant at $T \gtrsim 10^8$ K.
- Discrete line emission (electronic transition between two bound levels of the ion). Dominant at $T \lesssim 5 \ 10^7$ K. Collisionally excited spectral lines from highly ionized atoms are signatures of the thermal nature of hot plasmas.
- Radiative recombination continuum (capture of the electron into a bound state of the ion) with emission edges that fade out for $T \gtrsim 10^7$ K, when bremsstrahlung dominates.
- Dielectronic recombination lines (capture of a free electron into a doubly excited ion state through simultaneous excitation of a bound electron of the ion).
- Two-photon continuum (simultaneous emission of two photons from a metastable state).

Astrophysical plasmas are usually discussed in terms of the three thermal models presented in Table 1 or in terms of combinations thereof. Since the discovery in 1948 of X rays from the solar corona. Elwert (1952) started his pioneering work by applying the optically thin model to the solar corona, and this is therefore designated as the *coronal model*. The *nebular model* is the X-ray analogon of a planetary nebula, in which a central continuum source photoionizes the surrounding gas. This, and the optically thick *atmosphere model* can be applied to the important classes of X-ray binary sources containing a compact object, such as a white dwarf (WD), neutron star (NS), or black hole (BH). In practice, we may encounter a mixture of all models because in many cases the observed sources are not spatially resolved, which impedes the disentanglement of emission regions with different model properties. For example, low-resolution spectral observations with the Objective Grating Spectrometer on the *Einstein* observatory of twenty bright galactic X-ray binaries revealed blended line emission (and absorption) features from highly ionized atoms which can neither be explained by photoionization nor by coronal models (Vrtilek et al. 1991). Probably the features are observed

from a mixture of various distinct - and spatially unresolved - "coronal" and "nebular" regions.

How can we discriminate between different models such as the coronal and nebular models? For this we need spectroscopy with very high resolution ($\lesssim 0.05$ Å) such as provided by NASA's Advanced X-ray Astrophysics Facility *AXAF* and ESA's X-ray Multi-Mirror Mission *XMM*, space missions that are expected to fly near the end of this century.[2] First, it is possible to disentangle the different line emission regions by the Doppler measurement of line velocities as a function of binary phase and, second, to resolve the detailed differences in the spectra due to the different line formation processes in the two models.

Table 1. Comparison between plasma models

	Coronal Model	Nebular Model	Atmosphere Model
Assumptions	Optically thin; collisional ionization & collisional excitation	Optically thin/thick; photo-ionization & -exc., and el. scatt. by radiat. from ext. X-ray source	Optically thick; collisional ionization
Examples	-stellar coronae & flares -SNRs (transient) -clusters of galaxies	-compact objects (WD, NS,BH in X-r.binaries) -stellar winds -AGNs	-photosphere of hot O stars -hot DA WDs -NS
Model parameters	$-EM=\int n_e N_{\rm H} dV$ or $-DEM = n_e N_{\rm H} dV/d\log T$ $-T$ (controlled externally) $-n_e$ (dens.-sensitive lines) -abundances	$-\xi = L_{\rm X}/nr^2$ (ioniz. par.) $-(L_{\rm X} n)^{1/2}$ (continuum opt. depth) $-n_e$ -abundances	$-T_{\rm eff}$ $-g$ -abundances
Characteristics	Spectra with emiss.lines excited by electron coll.; He-like singl./tripl.ratio & Fe XVII-XIX lines discriminate between coronal/nebular model	Spectra with emission & absorption lines formed by recombination; *many* ion stages at low T	Spectra with ionization absorption edges/lines and continuum
Problems	-atomic rates -non-stationary ionization balance	T is not free parameter, but is determined by local energy equations	-NS comptonization (Monte Carlo calc.) -layered atmosphere -non-LTE effects

In the coronal model the heat input is coupled directly to the ions and free electrons, and its characteristic parameters are (electron) temperature T, ele-

---

[2] See also the Chapter by Paerels.

ment abundances, and (differential) emission measure $(D)EM$ (cf. Sect. 14). At given T only one or two ionization stages of a given element are abundant. In the nebular model T is not a free parameter, but instead is determined by absorption and emission in the gas of the incident radiation from an external X-ray source embedded in the gas. The gas is primarily ionized by inner-shell photoionization. As a result, a wider range of ionization stages of a given element can simultaneously occur and the elements are more highly ionized ("overionized") at a given temperature than they would be in the coronal model. In a photo-ionized plasma the excitation of lines is dominated by radiative recombination (with cascades) and photo-excitation as opposed to collisional excitation from the ground state in a coronal plasma. Therefore, high-resolution spectra of X-ray photoionized plasmas can appreciably differ from those of collisionally ionized plasmas with similar ion concentrations.

Liedahl et al. (1991) have developed a useful diagnostic to distinguish between coronal and nebular models using high-resolution Fe L-shell $3 \rightarrow 2$ spectra (from Fe XVII–XIX ions) at ~ 1 keV on the basis of the different line formation processes in a coronal plasma (collisionally excited $3d$ lines at T a few MK) and a nebular plasma (recombination-cascade-populated $3s$ lines at T about 0.1 MK).

3   Spectral Modeling of Optically Thin Plasmas

3.1   General scheme

We need to assume a model to infer from the observations the relevant physical parameters including electron temperature, emission measure, density distributions, ion and elemental abundances, mass motions, and the nature of the ambient radiation field. The usual procedure is to apply a forward modeling technique by convolving theoretical model spectra with the instrumental response and to vary the model parameters in order to optimize the fit of the model to the observational data. A common approach is to consider first a simplified plasma model for the X-ray source, neglecting much of the complexity of the temperature and density structure and of the effects of opacity, and to synthesize such models into successively more sophisticated approximations of the source model. The processing flow diagram in Fig. 1 illustrates the spectral modeling.

3.2   Spectral fitting with SPEX

The advent of the new series of X-ray satellites with high sensitivity and spectral resolution such as *EUVE, ASCA, BeppoSAX, AXAF* (1998), *XMM* (1999), *Spectrum X-γ* (1999), and *ASTRO-E* (2000) strongly demands the availability of spectral codes with higher accuracy and more detail than before. Since 1992 a completely new software package **SPEX (SPEctral X-**ray
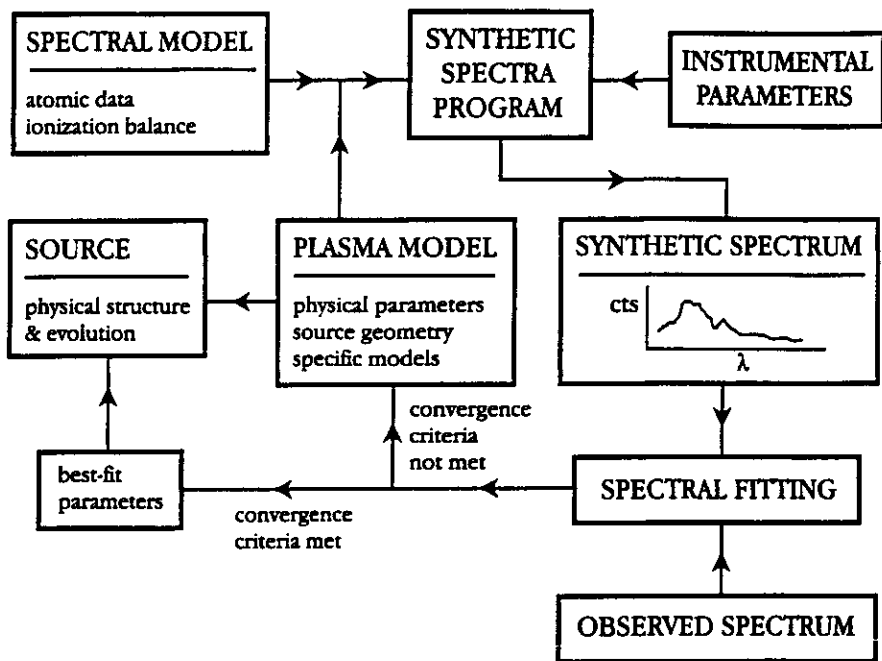
Fig. 1. Processing flow diagram of spectral modeling of optically thin plasmas (from Mewe & Kaastra 1994).

and UV modeling & analysis software package) was designed and developed at our SRON institute to model and fit complicated spectra of hot astrophysical plasmas (Kaastra, Mewe & Nieuwenhuijzen 1996). It encompasses a number of modules for the computation of physical parameters and associated emergent spectra of optically thin plasmas in *collisional ionization equilibrium* (**CIE**) (Mewe et al. 1985a, 1986; Kaastra & Mewe 1993; Mewe & Kaastra 1994) ranging from simple one-temperature to more complicated models, such as stellar coronal loop structures and supernova remnants [also including transient ionization effects, so-called *non-equilibrium-ionization* (**NEI**) models], photoionized plasmas, and optically thick plasmas. Moreover, it contains a variety of differential emission measure (DEM) analysis methods for optically thin plasmas (cf. Sect. 14).

The model spectra can be convolved with instrumental response functions. Different spectral fitting procedures are available. Also simple models (e.g., power law, blackbody, delta functions, and Gaussian lines, and in the future also photoionization models) are included. SPEX has been installed at the

High Energy Astrophysics Science Archive Research Center (HEASARC) of NASA since 1995, and in a more updated version at our institute since 1996. Calculations for the Fe-L complexes have been *preliminarily* updated using results from the HULLAC code at Livermore (Liedahl, Osterheld & Goldstein 1995), and various other improvements have been made (Mewe, Kaastra & Liedahl 1995a).

Several earlier versions of our optically thin plasma code have been implemented as the "Mewe" code at various institutes and in the widely distributed spectral-fitting package XSPEC. The latest version of the code – which contains the updates mentioned above – was installed in 1995 under the name "MEKAL" (Mewe–Kaastra–Liedahl) in XSPEC (version 8.3) of HEASARC.

4   The Coronal Model

The coronal model is a familiar standard model that was first applied to the *solar corona* (Elwert 1952). It implies the following assumptions:

- The plasma is optically thin, so that the X rays are not attenuated by the interaction with the atoms or ions in the plasma, and do not affect the populations in the bound atomic levels.
- The gas density is sufficiently low so that the excited state populations are negligible compared to the ground state population.
- Radiation losses are balanced by non-radiative (mechanical) heating.
- The plasma electrons and the ions are relaxed to Maxwellian energy distributions with a common temperature, T, a free parameter controlled by external processes.
- The gas is assumed to be in a steady state of statistical equilibrium both for the bound atomic states and for the ionization balance.

Assumption (1) implies that the emergent X-ray spectrum faithfully represents the microscopic emission processes in the plasma and therefore is directly linked to the physical conditions in the plasma. It further implies that *photo-excitation* and *photo-ionization* (processes that are very important in nebular-type plasmas) are neglected here.

Assumption (2) may break down in the case of metastable levels which then should be taken into account separately.

Assumption (3) is valid for cosmic sources such as stellar coronae and supernova remnants which are heated by non-radiative processes that include e.g., magnetic-field annihilation, MHD waves, and shock waves.

Assumption (4) implies that the electron-electron relaxation time $t_{ee} \approx 0.01 T^{3/2} n_e^{-1}$ (s) [Spitzer 1962; T in K, electron density, n_e, in cm^{-3}] is short enough to ensure a Maxwellian velocity distribution for the electrons, unless the time scales for energy loss or gain, or particle containment are smaller than t_{ee}. If the mechanisms of energy supply to the plasma preferentially heat

one kind of particles (e.g., heavy ions in shocks or electrons in microturbulent plasmas) ion and electron temperatures may differ significantly, if the Coulomb collision equilibration time (Spitzer 1962) $t_{ei} \approx 10\ T^{3/2}n_e^{-1}$ (s) is too long, unless plasma instabilities reduce the equilibration time scale (e.g., in the turbulent shock front in supernova remnants; Mewe 1984).

In order to keep the plasma in a steady state, the heating is balanced by the cooling due to line and continuum emission and the ionization equilibrium must be reached (assumption 5). Line emission is mainly due to electron impact excitation followed by spontaneous decay of a bound level within a highly ionized atom, while continuum emission is produced by the interaction of a free electron with an ion either by a free-free transition between two continuum states, a free-bound transition, or a two-photon process.

In the other extreme case of a *high-density* plasma in Local Thermodynamic Equilibrium (*LTE*) every atomic process is as frequent as its inverse process: we call this *the Principle of Detailed Balancing (PDB).*[3]

In an optically thin plasma the radiation which originates in the interior escapes the plasma so that each collision process cannot be balanced by its inverse collision process as in the LTE model. A simple description is then only possible if we assume that the electron density and the radiation field intensity are so small that an excited atom will decay by spontaneous radiation and an ionized atom will recombine by radiative or dielectronic recombination. The stationary ionization state in the coronal model is established by a balance between electron impact ionization and excitation-autoionization, and radiative and dielectronic recombination; the electron density is too low for *3-body recombination* (the inverse process of collisional ionization) with dielectronic or radiative recombination. Such a plasma is said to be in *collisional ionization equilibrium* (CIE).

Examples of steady coronal plasmas:

– stellar coronae;

– hot gas in interstellar and intergalactic medium;

– clusters of galaxies.

A transient, but optically thin plasma such as a supernova remnant is an example of *non-ionization equilibrium* (NEI) (cf. Sect. 4.1.3).[4]

High-resolution soft X-ray (5–140 Å) spectroscopy (e.g., with *AXAF* and *XMM*) will allow detection and identification of a multitude of prominent spectral features from nearly all ion stages of many abundant elements, including the K-shell transitions of C, N, O, Ne, Mg, and Si, and the L-shell transitions of Si, S, Ar, Ca, Ni, and Fe. The interpretation of such an X-ray

---

[3] We can use the PDB to derive the relation between the atomic rate coefficients of two inverse processes which is independent of the equilibrium (cf. Sections 7.1, 7.2, and 8.1.2).

[4] Though strictly speaking assumption (5) excludes this category of transient plasmas from the coronal model, all rate coefficients valid for optically thin plasmas can also be used in this case.

spectrum requires a detailed knowledge of the ionization, recombination and excitation rates involved.

It is obvious that the physical parameters can be inferred only at the accuracy level of the available rates of ionization, recombination and excitation. Later on I discuss the expected accuracy of these data, but I may also refer to Raymond (1988) and Mewe (1990) who have discussed the atomic physics of the ionization balance and the line excitation.

4.1   Deviations from the coronal CIE model approximation

Apart from the uncertainty in the basic atomic parameters other uncertainties can arise from the simplifying assumptions we have made in the coronal model. Mewe (1990) and Raymond (1988) have discussed the effects of relaxing the restrictions for the simple steady optically thin model by considering effects of photo-ionization, optical depth, resonance line scattering, high density, non-Maxwellian velocity distributions, and non-equilibrium ionization (NEI) in a transient plasma. I consider the effects of optical depth, high density, and of NEI and mention briefly the effect of a non-Maxwellian velocity distribution. For more details I refer to the above papers.

4.1.1 Optical-depth effects: criteria for the optically thin approximation. In the coronal model we assume that the plasma is optically thin, so that the observed intensities and plasma emissivities are directly proportional. Once some radiation is absorbed, radiative transfer must be considered.

In the extreme case of very density plasmas, e.g., those present in the inner regions of accretion flows on compact objects such as hot white dwarfs and neutron stars, the source is optically thick to both continuum and line radiation. The spectrum will resemble, at very high optical depths, blackbody emission.

At intermediate optical depths, the spectral formation is influenced by complicated radiation transfer effects as well as by fundamental atomic processes. Discrete spectral structure is expected which can provide much information about the source (Ross 1979). For X-ray emitting plasmas, Compton scattering plays a significant role as well, and transfer through the scattering plasma will broaden and shift line profiles and alter the continuum distribution, depending on temperature and column density (Lightman et al. 1981).

For the optically thin approximation we apply the criterion that the intensity of a given type of radiation should not differ from the value obtained from the optically thin approximation by more than 10%, which can be expressed as (e.g., Cooper 1966):

$$\tau_\lambda(D) \lesssim 0.2 \ , \tag{1}$$

where $\tau_\lambda = \alpha_\lambda D$ is the optical depth at wavelength λ, α_λ the linear absorption coefficient (cm^{-1}) and D the typical dimension (cm) of the (homogeneous)

plasma. I evaluate criterion (1) for the following radiation processes which may contribute to the optical depth (ignoring stimulated emission or stimulated recombinations) [cf. Cooper 1966; Wilson 1962]:

(i) photo-absorption of line radiation,

(ii) photo-absorption of recombination radiation,

(iii) photo-absorption of bremsstrahlung,

(iv) scattering by free electrons.

(i). For line radiation, resonance line absorption is most serious. For a Doppler broadened line profile, the application of criterion (1) to the central wavelength λ (Å) gives [expressing the density $N_{Z,z}$ of the absorbing ion Z^{+z} of element Z in terms of the electron density n_e (cm^{-3}), the ion fraction $\eta_{Z,z}$ and the element abundance $A_Z = N_Z/N_H$, i.e. $N_{Z,z} = 0.85 n_e \eta_{Z,z} A_Z$ for a plasma with cosmic abundances]:

$$Dn_e \lesssim 2\ 10^{13} \frac{\sqrt{T_i/M_i}}{\lambda f \eta_{Z,z} A_Z}\ (\text{cm}^{-2})\ , \tag{2}$$

where f is the absorption oscillator strength of the line, T_i(K) the ion temperature and M_i the ion mass number. For example, for λ=20Å, f=0.5, η=0.5, A_Z=10^{-4}, T_i=3 10^6 K, and D=10^8 cm, we have $n_e \lesssim 2\ 10^{11}$ cm^{-3}, which emphasizes the importance of considering very carefully opacity effects in solar and stellar flare and active region conditions. This criterion will be relaxed when additional line broadening from Stark $[\Delta\lambda_S \sim 4\ 10^{-18}\lambda^2 n_e^{2/3}(z+1)^{-1}]$ or Zeeman effect $[\Delta\lambda_Z \sim 10^{-12}\lambda^2 B]$ becomes comparable to the Doppler broadening $(\Delta\lambda_D \sim 7\ 10^{-7}\lambda\sqrt{T_i/M_i})$ at sufficiently large plasma densities or magnetic fields (B in Gauss, line widths $\Delta\lambda$ and wavelengths in Å).

When the plasma becomes optically thick ($\tau \gtrsim 1$) the effect on the intensity of the resonance line is determined by the processes competing with the spontaneous radiative decay to the ground level. In a high-density plasma a resonance photon will be completely destroyed after an absorption, but in a low-density plasma (with $\tau > 1$) the situation can exist that each time a photon is absorbed, only a small fraction b ($\ll$1) is destroyed. Since, on average, a photon is absorbed and re-emitted ("scattered") $\sim \max(\tau, \tau^2)$ times before escaping, the plasma can still be considered effectively optically thin as long as $b\tau \ll 1$ (e.g., Hearn 1966). E.g., for Lyman α, where the loss occurs through electron excitation to the next higher level, $b \sim 2\ 10^{-23}\lambda^3 T^{-1/2} n_e$, but for Lyman β the situation is completely different because here the main process competing with Lyman β emission is Balmer α emission, hence $b \sim 0.44$, independent of temperature and density.

If the emitting region is not spherical (e.g., a long thin coronal magnetic flux tube), the effects of resonant scattering can drastically enhance the intensity in the direction of the shortest plasma dimension where the re-emitted photons (from absorption in the longitudinal direction) more readily escape (e.g., Acton & Brown 1978; Sylwester et al. 1986, and discussion by Raymond

1988). In principle, one can extract from the spectra information about the geometry of the source, although the interpretation can be quite complicated.

(*ii*). For photoexcitation we obtain approximately for transitions from the ground state to the absorption edge (where the absorption is maximum):

$$Dn_e \lesssim 5 \; 10^{16} \frac{(z+1)^2}{\eta_{Z,z} A_Z} \; (\text{cm}^{-2}) \; . \tag{3}$$

Breakdown of criterion (3) occurs in an important class of cosmic X-ray sources involving *photoionized nebulae*, such as accretion-powered sources like X-ray binaries, cataclysmic variables, and active galactic nuclei, where a central X-ray emitting region is surrounded by a cooler, partially ionized medium, and hot shocks in the winds of early-type stars.

In all these cases photoelectric absorption edges will substantially modify the emergent X-ray spectrum particularly at longer wavelengths. High-resolution spectral measurements of the strength of K-shell absorption edges in combination with emission lines produced by recombination, provide information on the geometry of the medium surrounding the source along the line of sight. The nebular model (e.g., Holt & McCray 1982; McCray 1984; Kallman & McCray 1982) is the X-ray analogue of a planetary nebula, in which a central continuum source ionizes the surrounding gas. The gas may be optically thick to photoabsorption but not to electron scattering. The ionization and temperature structure of the gas are established by a stationary balance between photoionization (collisional ionization can be neglected) and heating due to the central X-ray source and, on the other hand, (radiative plus dielectronic) recombination and charge exchange and cooling of the gas. When the gas is optically thin, the local radiation field is determined by geometrical dilution of the source spectrum. Then the local state of the gas (at radius R from the central X-ray source) can be parametrized in terms of the scaling parameter $\xi = L/nR^2$ [L is total luminosity of the central source, n is the local gas density; when electron scattering also is important, the ionization parameter is defined as $\xi = L/nR^2\tau$, where τ is the electron scattering optical depth (Ross 1979; Fabian & Ross 1981)].

The model can be applied to a wide variety of astrophysical X-ray sources and ranges from optically thin to optically thick in the photoionization continuum of abundant elements. In the latter case, the transfer of continuum radiation should be taken into account which yields one additional parameter $(Ln)^{1/2}$ which characterizes the continuum optical depth at a given value of ξ. The photoionization model is treated in detail in the Chapter by D. Liedahl.

(*iii*). Using the free-free absorption coefficient (e.g., Spitzer 1962; Cooper 1966), criterion (1) reduces to

$$Dn_e^2 \lesssim 1.5 \; 10^{46} \, T^{1/2} \lambda^3 \bar{G}_c^{-1} \; (\text{cm}^{-5}) \; , \tag{4}$$

where T is the electron temperature (K) and $\bar{G}_c$ the average Gaunt factor (Mewe et al. 1986). The criterion is best evaluated for the region of maximum

bremsstrahlung emission, i.e. for $h\nu \sim 2kT$, or $\lambda T \sim 10^8 \text{Å K}$ [here $G_c \sim 1$ for a plasma with cosmic abundances (Mewe et al. 1986)].

(*iv*). For electron scattering to produce no appreciable optical depth, the Thomson cross section ($\sigma_T = 6.65 \ 10^{-25} \text{ cm}^2$) gives

$$Dn_e \lesssim 3 \ 10^{23} \ (\text{cm}^{-2}). \tag{5}$$

For the case of plasmas in which Compton scattering dominates I refer to the Chapter by D. Liedahl.

With the above criteria (*i*)–(*iv*) we can estimate when the intensity at a given wavelength differs by more than 10% from the optically thin value. Examination of these criteria indicates that criterion (*i*) is often most severe and criterion (*ii*) will be so in photoionized plasmas, while the criteria (*iii*) and (*iv*) will break down only for very dense plasmas in compact X-ray sources (powered by accretion onto a neutron star or black hole) where Compton scattering plays a significant role.

4.1.2 High-density effects: transition from coronal to thermal model.
The ionization distribution in a low-density coronal plasma is very different from that described by the *Saha equation* (e.g., Unsöld 1955; Allen 1973; Griem 1964, 1997) in a very dense plasma in thermodynamic equilibrium which, e.g., for a hydrogenic plasma reads (Z^{+z} is hydrogenic ion with ionization energy χ_z, $Z^{+(z+1)}$ is bare nucleus of charge number $z + 1 = Z$), omitting subscript Z:

$$\frac{N_{z+1}n_e}{N_z} = \frac{2w_{z+1}}{w_z}\left(\frac{2\pi m_e kT}{h^2}\right)^{3/2}\exp\left(-\frac{\chi_z}{kT}\right) =$$
$$4.8294 \ 10^{15} \ \frac{w_{z+1}}{w_z} \ T^{3/2} \exp\left(-\frac{1.5789 \ 10^5 Z^2}{T}\right) \ , \tag{6}$$

where T is in K and n_e in cm^{-3}, and the usual symbols are used for the fundamental physical constants. For the ratio of the statistical weights (or more generally partition functions) we can take $w_{z+1}/w_z = 1/2$ in the hydrogenic case. Whereas in the coronal approximation N_{z+1}/N_z is independent of n_e, this ratio varies as $\sim n_e^{-1}$ in the high-density limit. Clearly, in the latter case Eq. (6) predicts for low-Z ions at lower densities a much higher degree of ionization (i.e. larger N_{z+1}/N_z) compared to the coronal model (cf. Eq. 13) in which the ions of a given ionization stage can exist at much higher temperatures. From approximate hydrogenic formulae (Wilson 1962; Griem 1964, 1997; McWhirter 1965) it can be estimated whether coronal conditions are valid or not. The coronal domain is roughly bounded by the condition (deviations from coronal ionization balance less than about a factor of two):

$$n_e \lesssim 4 \ 10^4 \ (z + 1)^2 \ T^2 \ (\text{cm}^{-3}), \tag{7}$$

whereas the extreme high-density limit is reached at densities approximately

$$n_e \gtrsim 1.4 \ 10^{15} \, (z+1)^6 \, T^{1/2} \ (\text{cm}^{-3}), \tag{8}$$

where T is the electron temperature in K. The latter condition for complete Local Thermal Equilibrium (LTE) may be relaxed by about two orders of magnitude if the resonance transitions are self-absorbed and become optically thick, because this effectively reduces the radiative population rate (e.g., Mewe 1967, 1970).

In the region intermediate between the coronal and thermal domains, the situation is complicated, and the problem is to solve the differential equations describing the population and depopulation of many bound levels [e.g., reviews by Cooper (1966) and Wilson (1962)]. Moreover, if the plasma is neither optically thin nor thick towards the resonance lines, the rate coefficients depend also on the optical depths and an exact computation would require a solution of the level population rate equations coupled with the equations of radiative transfer.

Because collisional rates between bound levels increase with principal quantum number, and corresponding radiative decay rates decrease, the upper bound states near the ionization limit are strongly collisionally coupled to the continuum of free electrons and weakly coupled to the ground state, whereas for the lower levels the reverse is the case. From the work by Wilson (1962) the physical picture emerged that the thermal equilibrium in the continuum extends down to the upper bound levels owing to the high collisional rates between the upper bound levels and the continuum. Since this is imposed on the upper levels by the free electrons, the thermal equilibrium of the bound levels is linked to the continuum and their populations are given by Saha-Boltzmann equations. There is therefore a certain level n_t in the ion, for which upward collisional rates balance the downward radiative decay rates. It is known as the *thermal limit* (TL) because it defines the limit above which the levels are in thermal equilibrium with the continuum and below which the level distributions are approximately coronal. For low n_e, the TL is very close to the ionization limit (coronal approximation valid), for increasing n_e the TL drops until, at sufficiently high densities it reaches the ground level ($n_t=1$, LTE). For a hydrogenic ion Z^{+z} in an optically thin plasma the thermal limit is given by (Wilson 1962):

$$n_t^7 = 1.4 \ 10^{15} \, (z+1)^6 \, T^{1/2} n_e^{-1}. \tag{9}$$

For $n_t=1$ this equation indeed corresponds to Eq. (8).

4.1.3 Non-equilibrium ionization (NEI) in transient plasmas.

When processes such as plasma instabilities, shock compression, rapid expansion, heating or cooling of the gas, etc., cause a change in the physical plasma parameters (like electron temperature T and electron density n_e) on a plasma time scale, t_{pl}, much shorter than the time t_{rel} in which the plasma relaxes to ionization equilibrium, the assumptions of a steady-state equilibrium break down: the plasma is in a *transient* state. The establishment of

Table 2. Parameters for transient plasmas

Source		t_{pl}^1	n_e^2	T^3	$n_e t_{pl}$	η^4	$Z^{+z} \rightleftharpoons Z^{+(z+1)}$		T^3
Hot ISM		10^{13}-10^{14}	10^{-3}-0.1	0.5-2	10^{10}-10^{13}	$2\ 10^{11}$	C V	VI	1
						$2\ 10^{12}$	O VII	VIII	1
SNR	old	10^{12}-10^{13}	0.1-10	1	10^{11}-10^{14}	$4\ 10^{11}$	O VII	VIII	2
						$4\ 10^{10}$	Fe XVIII	XIX	2
	young	10^{10}-10^{11}	0.1-10	5-10	10^9-10^{12}	$5\ 10^{12}$	Si XIII	XIV	6^5
						$3\ 10^{10}$	Fe XXIV	XXV	6^5
				10-100		10^{12}	Fe XXV	XXVI	50^6
Impulsive solar flare		1-100	10^9-10^{12}	20-60	10^9-10^{13}	10^{11}	Fe XXIV	XXV	30
						10^{12}	Fe XXV	XXVI	30
Tokamak		10^{-3}-10^{-2}	10^{14}-10^{15}	$\gtrsim 10$	10^{11}-10^{13}	$2\ 10^{11}$	Fe XXIV	XXV	15
Θ Pinch		10^{-6}-10^{-5}	10^{15}-10^{16}	$\gtrsim 10$	10^{10}-10^{11}	$3\ 10^{11}$	Fe XXV	XXVI	15
Laser pl.		10^{-9}-10^{-8}	10^{19}-10^{20}	$\gtrsim 10$	10^{10}-10^{11}				

[1] Characteristic plasma time scale or age in s.
[2] Electron density in cm^{-3}.
[3] Electron temperature in MK.
[4] Ionization parameter $\equiv n_e t_{rel}$ (cm^{-3} s^{-1}), where t_{rel} is relaxation time for ionization equilibrium.
[5] Reverse shock.
[6] Main shock.

the ionization balance then lags the temperature changes, and this can have dramatic effects on the emergent X-ray spectrum. As $t_{rel} \propto 1/n_e$ the parameter that characterizes this *non-equilibrium ionization* (NEI) is the *ionization parameter* $n_e t$ or more generally $\int n_e dt$ when n_e varies with time (Kaastra & Jansen 1993). X-ray emitting, hot plasmas are out of equilibrium typically for $n_e t \lesssim 10^{10} - 10^{13}$ cm^{-3} s. As a result, such a non-equilibrium gas initially radiates thermal X-ray bremsstrahlung characteristic of the high temperature just after the heating and virtually independent of the ionization balance, together with line plus two-photon and free-bound emission characteristic of the non-equilibrium ionization structure corresponding to the pre-heating state. The line spectrum is therefore much softer than the bremsstrahlung continuum, and as the gas ionizes out, this NEI enhancement of the soft X rays will eventually disappear, with spectral hardening occurring along the way (for examples, e.g., Shapiro & Moore 1977).

To evaluate in which circumstances transient conditions apply, we estimate the ionization equilibrium relaxation time scale $t_{rel} \simeq \min(t_{ion}, t_{rec})$ with approximate formulae (Mewe 1984) for the time scales for ionization (t_{ion}) and recombination (t_{rec})

$$n_e t_{ion} \approx 10^{10}(z+1)^4 n_z^{-4} \zeta_z^{-1} T^{-1/2} e^y \ (\text{cm}^{-3}\text{s}) \ , \tag{10}$$

$$n_e t_{rec} \approx 10^{11}(z+1)^{-2} n_z^{5/2} \xi_z^{-1} T^{1/2} \ (\text{cm}^{-3}\text{s}) \ , \tag{11}$$

where $y = 1.58 \ 10^5 (z+1)^2 n_z^{-2} T^{-1}$, ζ_z (or ξ_z) the number of valence electrons (or empty spaces) in the outer shell with principal quantum number n_z of the ionizing (or recombining) ion Z^{+z} (or $Z^{+(z+1)}$), and compare this to the relevant dynamical plasma time scale t_{pl} (for more details and examples of NEI plasmas, see the Chapter by D. Liedahl).

In Table 2 I have presented a number of representative cases. It is seen that notwithstanding the widely different categories of optically thin astrophysical plasmas, such as young supernova remnants (SNR), hot interstellar media of galaxies, solar or stellar flares, and fusion-oriented laboratory plasmas, that span a wide range of dynamical time scales ($t_{pl} \sim 10^{-9}$ to 10^{14} s), these cases cover only a restricted range in $n_e t_{pl}$ ($\sim 10^9$ to 10^{14} cm^{-3} s). Because the ionization equilibrium time scales $n_e t_{rel}$ range from $\sim 10^{10}$ to 10^{13} cm^{-3} s, the transient situation is believed to apply to many of these cases (with probably the only exception of quiet stellar coronae and the hot gas in clusters of galaxies which both have $n_e t_{pl} \approx 10^{13}$–$10^{14}$ cm^{-3}; Mewe 1984).

For a highly transient plasma like a SNR the equilibrium ionization model completely fails and we must introduce the NEI model for an adequate description. However, in the early 1980s astronomers first misinterpreted the *Einstein* X-ray spectra of SNRs by applying a CIE model and assumed special evolution effects to explain the derived artificially anomalous abundances. This is a typical example of a more complex plasma model in which the transient nature of the plasma and its spatial structure must be simultaneously taken into account for a proper interpretation of the observed X-ray spectrum; the X-ray observations of young SNR clearly confirm that non-equilibrium effects in the ionization balance are very important (e.g., Gronenschild & Mewe 1982; Hamilton & Sarazin 1983; Itoh 1984a; Masai 1984, 1994a). The spectral modeling is quite complicated. To generate a SNR model the following steps can be distinguished (e.g., Kaastra & Jansen 1993). First, the hydrodynamical model describing the blast and the reverse shock waves is calculated yielding the distribution of density, velocity and temperature as a function of position and time. Then the ion densities are evaluated by integrating the T- and n_e-dependent equations for the ionization balance over time and the X-ray spectrum is computed for the known set of ion concentrations for each position in the SNR. Finally, we include Doppler shifts due to the plasma motion and project the spectrum onto the sky and integrate it over the relevant area of the sky.

4.1.4 Non-Maxwellian electron velocity distributions.

If departures from a Maxwellian electron velocity distribution occur this may significantly influence the calculation of the ionization balance and of the excitation rates. In Sections 15.4.3 and 15.4.4 we will consider various situations in which
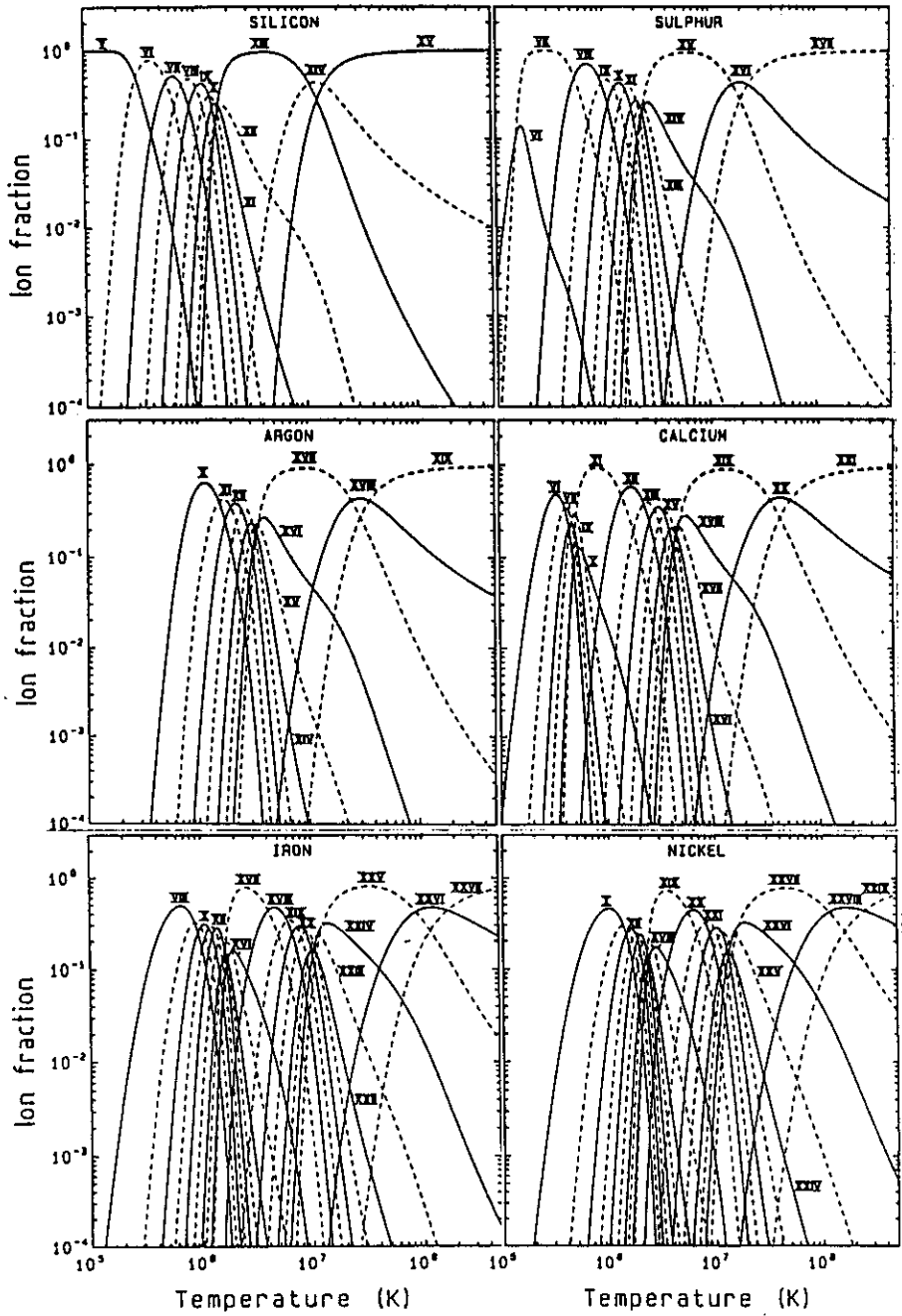
Fig. 2. Ion fractions of Si, S, Ar, Ca, Fe, and Ni as a function of electron temperature (from Mewe 1988).

such deviations can occur and how we can use these as a diagnostics. In these sections the line and continuum emission is calculated for a power law and a mono-energetic electron distribution.

II. Ionization and Recombination in a Coronal Plasma

5 Ionization Balance

Much of the temperature sensitivity of the soft X-ray spectrum is associated with the ionization structure. Under the assumptions of the coronal model, all ions can be taken to be in their ground states. The ionization state is controlled by electron impact ionization (including sometimes a contribution from excitation-autoionization) and by radiative plus dielectronic recombination. The rate of change of the population density $N_{Z,z}$ (in cm^{-3}) of ion Z^{+z} from element of atomic number Z is given by

$$\frac{1}{n_e}\frac{dN_{Z,z}}{dt} = N_{Z,z-1}S_{Z,z-1} - N_{Z,z}(S_{Z,z} + \alpha_{Z,z}) + N_{Z,z+1}\alpha_{Z,z+1} , \quad (12)$$

where $S_{Z,z}$ and $\alpha_{Z,z}$ are the total ionization ($z \to z+1$) and recombination ($z \to z-1$) rate coefficients (in $cm^3\ s^{-1}$) of ion Z^{+z}, etc. ($z = 0, 1, \ldots, Z$).[5] This equation shows that, in an evolving plasma, the characteristic time scale to approach to a steady state is $\approx [n_e(S_{Z,z} + \alpha_{Z,z})]^{-1}$ and one can expect solutions to contain terms of the form $\exp[n_e(S_{Z,z} + \alpha_{Z,z})t]$ (see also the Chapter by D. Liedahl). In Eq. (12) we neglect *multiple ionizations.*[6] The ionization and recombination rate coefficients will be dealt with in Sections 6 and 7, respectively. The ionization structure can be derived by solving for each element Z a set of $Z+1$ coupled rate equations. Eq. (12) can be written in the form of a matrix equation where the ion concentrations are represented by vectors of length $Z+1$ and the matrix is a tridiagonal $(Z+1) \times (Z+1)$ matrix composed of the ionization and recombination rate coefficients (Masai 1994a). The solution can be obtained using a matrix inversion technique.

The population of stage z depends on the four rates which connect it with the neighbouring ionization stages $z-1$ and $z+1$. If ion $z-k$ is most abundant, then in principle all the rates connecting stages between $z-k$ and z would enter. If, for example, all ionization rates would be systematically too high by a factor of two, then the predicted population of ion z would be

---

[5] Because we focus on the atomic rates we omit in Eq. (12) transport terms relating to the dynamic effects of mass motions (plasma expansion, diffusion, etc.). These must be appropriately taken into account for each particular plasma model if they have a non-negligible effect, e.g., in a laboratory plasma of finite size (see Düchs & Griem 1966; Peacock 1996).

[6] For the lower ions multiple ionization can be sometimes important (cf. Pal'chikov & Shevelko 1995).

off by 2^k. Fortunately, if k is more than say 1 or 2, the population is generally to small too matter.

For a *steady-state equilibrium* (collisional ionization equilibrium, *CIE*) $dN_{Z,z}/dt = 0$ in Eq. (12), and the population density ratio $N_{Z,z+1}/N_{Z,z}$ of two adjacent ionization stages $Z^{+(z+1)}$ and Z^{+z} can be expressed by

$$\frac{N_{Z,z+1}}{N_{Z,z}} = \frac{n_e S_{Z,z}(T)}{n_e \alpha_{Z,z+1}(T)} = \frac{S_{Z,z}(T)}{\alpha_{Z,z+1}(T)} \quad , \tag{13}$$

which is, to first order, only dependent on T and not on n_e, as long as stepwise ionization in $S_{Z,z}$ and collisional coupling to the continuum in $\alpha_{Z,z+1}$ can be neglected (Mewe 1970; Wilson 1962; Mewe & Schrijver 1978a; Mewe & Gronenschild 1981).

For each pair of subsequent ions the stationary ionization balance (Eq. 13) can be solved. With $\sum_{i=0}^{i=Z} N_{Z,z} = N_Z$ the total density of species Z, the solution for the fraction of ions in a specific ionization stage z can be expressed as

$$\eta_{Z,z} = \frac{N_{Z,z}}{N_Z} = \left[1 + \sum_{i=1}^{i=z} \prod_{k=i}^{k=z} \frac{N_{Z,k-1}}{N_{Z,k}} + \sum_{i=1}^{i=Z-z} \prod_{k=z+1}^{k=z+i} \frac{N_{Z,k}}{N_{Z,k-1}} \right]^{-1} . \tag{14}$$

Many results of such calculations have been reported in the literature (references up to 1984 are cited by Mewe 1984). As an example, in Fig. 2 I plot the ion fractions of six cosmically abundant elements from Si to Ni as functions of electron temperature, as calculated with the rate coefficients given by Mewe & Gronenschild (1981); for plots for He to Mg, see Mewe (1988). These results are very similar to those reported by Arnaud & Rothenflug (1985) which are often applied in the analysis of tenuous, astrophysical plasmas.

5.1   Accuracy of atomic physics for the ionization balance

Most spectroscopists agree that the ionization balance is one of the major uncertainties entering the comparison of models. In both ionization and recombination rates there are uncertainties typically $\sim$20–50%, but sometimes even more, say a factor $\sim$2 to 4. E.g., for the low Fe ions having $3d$ electrons the ionization rates as given by Arnaud & Rothenflug (1985) (ARo) are probably underestimated by factors 3–6, while for the Be- and Li-like and Ne- and F-like Fe ions the dielectronic recombination rates may be underestimated by factors 2–4, as was pointed out by Arnaud & Raymond (1992) (ARa). So the predicted ratio of ion concentrations of adjacent ionization stages may be off sometimes by a factor $\sim$2 or more. Fortunately, the ionization and recombination rates for the H- and He-like ions, which emit the lines that are among the strongest from hot astrophysical plasmas, are known more accurately than most of the other rates. In the case of ions which have a closed

outer electron shell (e.g., He- and Ne-like ions) it doesn't matter very much because such ions cover a broad plateau in temperature. This is because this ionization stage can easily be reached from the preceding Li- or Na-like stage (with only one outer electron with low binding energy) and persists long, since the next ionization step towards the H- or F-like stage needs a much ($\sim$4 times) higher ionization energy (it is much more difficult to take out an electron from a closed shell). The adjacent ionization stages (e.g., Li-like) depend more critically on temperature.

The effect of a systematic error can be readily estimated. Suppose that all ionization rates are underestimated by say a factor of 4. Since the rates typically vary as $\exp(-\chi/kT)$, and since the concentrations of ions with ionization energy χ typically peak at $\chi/kT \sim 3$, the ion peaks will be shifted to $\chi/kT \sim 4.4$, so that all ions will be shifted to lower temperatures by about 0.17 in $\log T$ (i.e. 50% in T).

Mewe (1990) has compared the results from various ionization balance calculations (RS, ARo, MG) and concludes that the overall shapes of the ion fraction $\eta_z(T)$ curves are quite similar and that the shifts of the ion peaks are generally limited within about $\Delta \log T \approx 0.1$-$0.2$, but that the ion peak values may differ by about 10–30% and sometimes up to a factor of two, especially for the ions adjacent to the He-like and Ne-like "plateaus".

The differences mainly result from different dielectronic recombination rates (for inaccuracies see Sections 7.2 and 7.2.2). For many diagnostic purposes the ARo ion balance is used, and for Fe the updated ARa calculations.

Recently Masai (1997) has discussed the effect of the ionization balance on the X-ray spectral analysis by comparing the ionization balance for iron based on ARo, ARa, and Masai (1984), respectively.

5.2   Update of the ionization balance by improved calculations for the rate coefficients

Arnaud & Raymond (1992) have made an attempt to update the ionization balance for the special case of Fe by introducing improved dielectronic recombination rates, but we are still lacking the revision of the Arnaud & Rothenflug (1985) ionization balance for the other elements. Moreover, a more general revision is desirable for the rates of radiative and dielectronic recombination.

5.2.1 Ionization rates. The most recent work has been done by Kaastra & Mewe (1998) who have fitted the ionization cross sections of all shells of ions from H to Zn (atomic number $Z = 1$-30). Apart from direct ionization, they include excitation-autoionization, resonance excitation, double autoionization, and direct multiple ionization. Further, an extended compilation of ionization rate coefficients has been made by Kato et al. (1991).

5.2.2 Recombination rates. Verner et al. (1993) and Verner & Yakovlev (1995) have calculated the partial photoionization cross sections of atoms and ions from He to Zn for all subshells $n\ell$ of ground-state species with the Hartree-Dirac-Slater method and have fitted their results by simple analytic functions. By use of the Milne relation (Eq. 34) one can obtain radiative recombination rates, and recently Verner & Ferland (1996) have followed such a procedure. They have calculated the rates for H-like, He-like, Li-like, and Na-like ions of all elements from H through Zn. These are the ionic species for which radiative recombination is not dominated by dielectronic recombination (at least at low temperature $\lesssim 10^4$ K and low density) because these ions do not have low-lying autoionization levels and therefore are not subject to low-temperature dielectronic recombination.

Recently, Huaguo & Zhizhan (1996) have fitted analytic formulae to dielectronic recombination rate coefficients for the H-like isoelectronic sequence, calculated with an intermediate-coupling multi-configuration Hartree-Fock method; Huaguo et al. (1994a,b,c,d) have done this for the Li-, Ne-, He-, and F-like sequences, respectively. Some further references are Karim & Bhalla [1988 (H), 1989 (He)] and Romanik (1988) (He, Li, Be, Ne) (cf. also Itikawa et al. 1995 for more references).
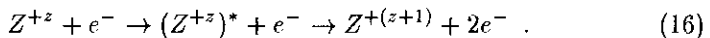
6   Rate Coefficients for Ionization

6.1   Collisional ionization

Under the conditions of the coronal model valid for low-density plasmas (see Sect. 4) the ionization equilibrium is determined by the balance between electron impact ionization and radiative and dielectronic recombination. Here I consider the ionization processes which, apart from *direct ionization* from the ground state (with rate coefficient $S_{Z,z}^{\mathrm{d}}$),

$$Z^{+z} + e^- \rightarrow Z^{+(z+1)} + 2e^- \tag{15}$$
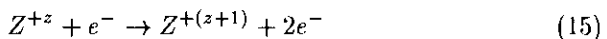
may also may contain a contribution from *excitation-autoionization*, i.e., electron impact excitation from the ground state to an autoionizing level (above the first ionization energy) followed by autoionization (rate coefficient $S_{Z,z}^{\mathrm{a}}$):

$$Z^{+z} + e^- \rightarrow (Z^{+z})^* + e^- \rightarrow Z^{+(z+1)} + 2e^- \ . \tag{16}$$

The total rate coefficient (in cm^{+3} s^{-1}) is

$$S_{Z,z} = S_{Z,z}^{\mathrm{d}} + S_{Z,z}^{\mathrm{a}} \ , \tag{17}$$

hence the number of ionizations (cm^{-3} s^{-1}) of ion Z^{+z} is: $n_e N_{Z,z} S_{Z,z}$, where n_e and $N_{Z,z}$ are the electron and ion densities (in cm^{-3}). The inelastic process of ionization (or excitation) is most effective when the relative velocity of the impacting particle is of the order of the orbital velocity of the bound

electron in the ion to be ionized (or excited). Thus if electrons and ions have comparable kinetic energies the electrons are much more effective, unless we consider population redistribution between nearby levels where e.g., proton collisions can be efficient. In the following I neglect ionization by ion impact (cf. also Sect. 8.1).

For the impact of an impinging electron with velocity v relative to the ion Z^{+z} to be ionized (or excited) the number of ionizations (excitations) per second reads:

$$N_{Z,z} \, v \, Q(v) \; , \tag{18}$$

where $Q(v)$ is the collision cross section (cm^2) for the particular process at the given relative velocity v (which is practically the velocity of the light electron itself). We obtain the rate coefficient S by averaging over the velocity distribution $f(v)$ of the electrons in the plasma:

$$S = \langle vQ(v) \rangle = \int_{v_0}^{\infty} vQ(v)f(v)\,\mathrm{d}v = \int_{E_0}^{\infty} \sqrt{2E/m_e}\,Q(E)f(E)\,\mathrm{d}E \; , \tag{19}$$

where $E = \frac{1}{2}m_e v^2$ is the electron energy and v_0 (or E_0) is the threshold velocity (or energy) of the collision process. Under the assumptions of the coronal model the electrons have a normalized[7] Maxwellian velocity (or energy) distribution with a temperature T:

$$f_{\mathrm{M}}(v)\mathrm{d}v = 4\pi \left(\frac{m_e}{2\pi kT} \right)^{3/2} v^2 \exp \left(-\frac{m_e v^2}{2kT} \right) \mathrm{d}v, \text{ or}$$

$$f_{\mathrm{M}}(E)\mathrm{d}E = \frac{2}{\sqrt{\pi}} \left(\frac{E}{kT} \right)^{1/2} \exp \left(-\frac{E}{kT} \right) \mathrm{d}\left(\frac{E}{kT} \right) \; . \tag{20}$$

Inserting Eq. (20) into Eq. (19) yields

$$S = \sqrt{\frac{8kT}{\pi m_e}} y^2 \int_{E_0}^{\infty} Q(U)\mathrm{e}^{-yU} U \,\mathrm{d}U \; , \tag{21}$$

where $U = E/E_0$ is the initial energy E of the impinging electron in terms of the threshold energy E_0, and $y = E_0/kT$ the reduced threshold energy. It turns out that the cross sections for excitation or ionization obey a scaling law by which the cross section can be written in a form

$$Q(U) = \alpha (E_{\mathrm{H}}/E_0)^2 Q_{\mathrm{red}}(U) \, \pi a_0^2 \; , \tag{22}$$

where the reduced cross section $Q_{\mathrm{red}}(U)$ is a scaled dimensionless cross section that for all ions in a given isoelectronic sequence has approximately the same form and is not sensitively dependent of the atomic parameters; a_0 is the first

---

[7] $\int_0^{\infty} f_{\mathrm{M}}(E)\mathrm{d}E = 1.$

H atom Bohr radius and E_H the ionization energy of a hydrogen atom,[8] and α is a numerical factor of the order unity.

Writing $E_0 = E_H z_e^2/n^2$ (z_e is the effective charge, n the principal quantum number of the state from which ionization takes place), Eq. (22) implies that the ionization cross section scales as $Q \propto (n/z_e)^4$. We may explain this as follows. At first sight we would expect $Q \sim \pi a_n^2 \sim (n^4/z_e^2)\pi a_0^2$ because the radius for the orbit (n) is $a_n = (n^2/z_e)a_0$. However, the electron-electron interaction has to compete with the electron-nucleus interaction (which goes as $\sim z_e/r$ at distance r). On a crude classical picture one may argue the e-e interaction to dominate only over a *fraction* $1/z_e^2$ of the total effective target area πa_n^2. Taking this into account we obtain indeed the *scaling $Q \sim (n^4/z_e^2)(1/z_e^2) = (n/z_e)^4$*.

6.1.1 Direct ionization. Numerous authors have attempted to represent the functional dependence of the direct electron-impact ionization cross section by a semi-empirical formula (e.g., Elwert 1952; Drawin 1961; Lotz 1968; Arnaud & Rothenflug 1985), which correctly represents both the behaviour at threshold $(U = 1)$, $Q \propto (U - 1)$ as well as the quantum-mechanical Born-Bethe dependence at high energies, $Q \propto U^{-1} \ln U$ [cf. also discussion of more complicated formulae by Arnaud & Rothenflug (1985), and Kaastra & Mewe (1998)].

In astrophysics the rates derived from the semi-empirical formula of Lotz (1968) for the cross section for direct impact ionization from the ground state have been widely used. The latter reads

$$Q(U) = \pi a_0^2 \sum_{k=m}^{N} C_k \xi_k W(U_k) \left(\frac{E_H}{\chi_k}\right)^2 \frac{\ln(U_k)}{U_k} \ , \tag{23}$$

where the summation is over (sub)shells m of the initial ion Z^{+z} with ionization energy χ_m, $U_m = E/\chi_m$, and where ξ_m is the effective number of equivalent electrons in the shell with principal quantum number m. In most cases it is sufficient to set N equal to 1 (outermost shell) or 2 (next inner subshell). The function $W(U) = 1 - b_m \exp[-c_m(U-1)]$ represents the deviation from linear behaviour near threshold (only significant for ions of low charge and for low temperature). From fits to experimental data or extrapolations Lotz (1968) found that one can take for ions ionized more than four times $W(U_m)=1$, and for the constant $C_m=2.76$. Then the "Lotz" rate coefficient for direct ionization (d) [for one shell only and omitting subscript m] follows from Eqs. (21) and (22) (with $\alpha = 2.76\xi_m$, $E_0 = \chi$, and $Q_{red}(U) = U^{-1} \ln U$):

$$S_{Z,z}^d = 3.244 \ 10^{-4} \xi \chi_{[eV]}^{-1} T_{[K]}^{-1/2} E_1(\chi/kT) \ (cm^3 s^{-1}) \ , \tag{24}$$

---

[8] $a_0 = 5.2918 \ 10^{-9}$ cm, $\pi a_0^2 = 8.797 \ 10^{-17}$ cm^2, and $E_H = 13.6057$ eV $= 1$ *Rydberg* (Ry) $= \frac{1}{2}$ *atomic unit* (a.u.).

where $E_1(y) = \int_1^\infty U^{-1}\exp(-yU)\,\mathrm{d}U \simeq \mathrm{e}^{-y}/(y+1) \approx \mathrm{e}^{-y}/y \ (y \gg 1)$ is the first exponential integral [cf. also Eq. (71)], since ion concentrations typically peak at $y = \chi/kT \sim 2\text{–}5$. Hence direct ionization rates scale with temperature as $S^d \propto T^{1/2}\chi^{-1}\exp(-\chi/kT)$.

Since threshold energies for ionization (and for $\Delta n \neq 0$ excitation) scale as $\chi \propto z_e^2$, where z_e is the effective charge number of the nucleus acting on the electrons in the shell (in particular for hydrogenic ions $Z^{+z} : z_e = z + 1$, for non-hydrogenic ions z_e is defined from $\chi_m = E_H z_e^2/m^2$), the cross section scales as $Q \propto z_e^{-4}$ (Eqs 22 and 23) and the rate coefficient, expressed as a function of *reduced* temperature $\Theta = T/z_e^2$, as $S^d \propto z_e^{-3}$ (Eq. 24). Calculations based on the Exchange Classical Impact Parameter (ECIP) method (Burgess et al. 1977; Summers 1974) predict rates typically about half those given by the Lotz formula, whereas the ionization rates now coming into widest use, those from Distorted Wave calculations (e.g., Younger 1981), appear to lie in between [see discussion by Raymond (1988)]. Many ionization cross sections have been measured for the lower ions with 10–20% accuracy (e.g., Gregory et al. 1987), while for the higher ions many atomic *rate* coefficients for ionization, recombination, and excitation have been obtained from plasma measurements (e.g., Wang et al. 1986, 1987, 1988; for reviews see Kunze 1972; Griem 1988). For cases in which experimental or theoretical data are not available, Burgess & Chidichimo (1983) suggest to use the Lotz formula (23) with $C_{(m)} \simeq 2.3$ and with $\xi_{(m)}$ and $\chi_{(m)}$ properly assigned. Arnaud & Rothenflug (1985) present an extensive compilation of ionization rates for 15 cosmically abundant elements (H, He, C, N, O, Ne, Na, Mg, Al, Si, S, Ar, Ca, Fe, and Ni) based on fits to available experimental cross sections and on Younger's theoretical results. Arnaud & Raymond (1992) have updated the rate coefficients for the special case of Fe. The most complete work has been done by Kaastra & Mewe (1998) who have fitted the ionization cross sections of all shells of ions from H to Zn (atomic number $Z = 1\text{–}30$).

6.1.2 Excitation-Auto-ionization. An additional ionization process via collisional excitation of an inner-shell electron is most important for ions which have a large number of electrons in the first inner subshell compared with the number in the outermost shell. An example is the sodium iso-electronic sequence ($1s^2 2s^2 2p^6 3s$, e.g., Fe XVI), where eight L-shell electrons can contribute to auto-ionization (AI) (e.g., $2p\text{-}3p$ and $2p\text{-}3d$ transitions), while there is only a single valence $3s$ electron that contributes readily to direct ionization (DI). Here an inner electron can be excited to a bound level above the first ionization threshold and subsequently can either autoionize (probability A^a), or can decay radiatively (probability A^r) to a bound state below the ionization threshold (e.g., Bely & van Regemorter 1970; Mewe 1988). This is illustrated in Fig. 3 for the Li-like case. In the total ionization cross section the AI contribution is recognized as a steep bump above the DI cross section. The net contribution to the ionization cross section can be
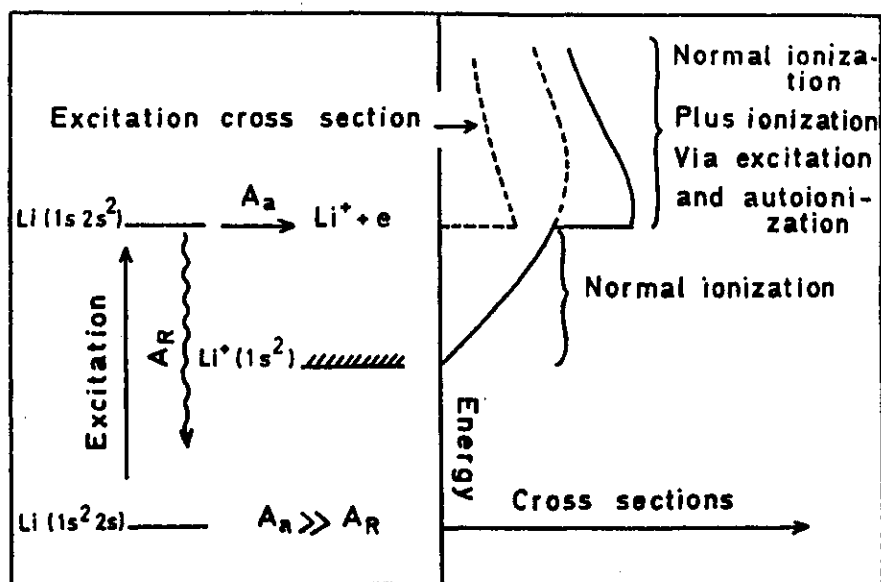
Fig. 3. Ionization via excitation and auto-ionization (after Bely & van Regemorter 1970).

written as a sum $\sum_s Q_{s,\mathrm{exc}} BR_s$ over all target bound states (s) lying above the first ionization limit and where the branching ratio $BR_s = A_s^{\mathrm{a}}/[A_s^{\mathrm{a}} + A_s^{\mathrm{r}}]$. Generally $A^{\mathrm{r}} \propto Z^4$ along an iso-electronic sequence, whereas A^{a} is approximately constant, so that B_i strongly varies along the sequence, while it can change very suddenly along successive ionization stages of one element. Typically $Q \propto E_0^{-2} U^{-1} \propto Z^{-4}$ (Eq. 65), so that the rate coefficient scales as (see Eq. 68) $S^{\mathrm{a}} \propto T^{-1/2} E_0^{-1} \exp(-E_0/kT)$ for $E_0/kT \gg 1$, where E_0 is the excitation energy of the autoionizing level. Arnaud & Rothenflug (1985) present a compilation based on semi-empirical fits to the results of calculations by Sampson (1982).

Resonant ionization. Other indirect processes which lead to ionization are multi-step resonant processes leading to the appearance of narrow resonances in the total ionization cross section. The first step in resonant ionization (RI) is the capture of a free electron (the same as in DR, cf. Sect. 7.2) and the creation of a doubly excited autoionizing state in the target ion which can decay by the emission of two electrons; the net result is a single ionization. Various combinations are possible such as "resonant-excitation-double-autoionization" (REDA) which, e.g., for the ionization of Fe XVI contributes up to 30% to the total ionization cross section [cf. Pal'chikov & Shevelko (1995), and Moores (1988)].
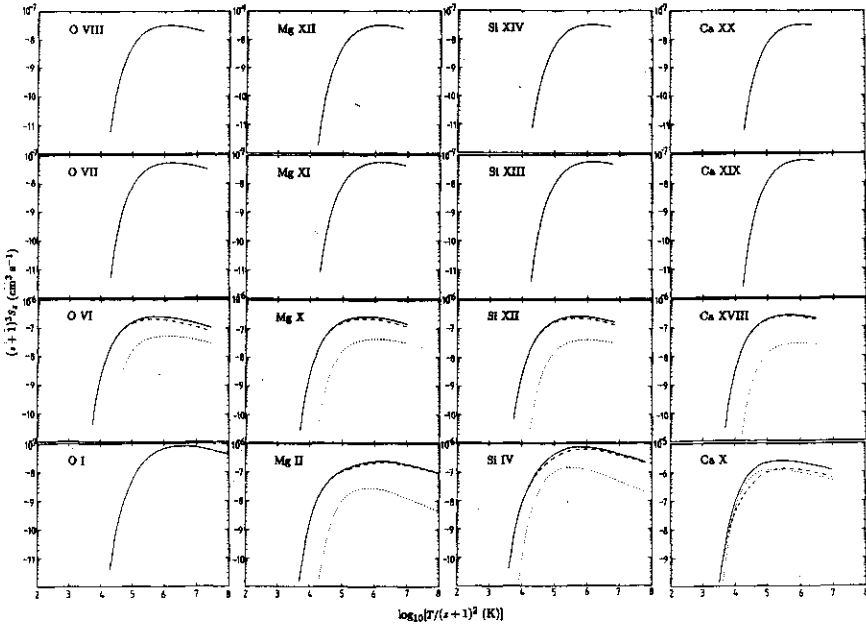
Fig. 4. Reduced rate coefficients $(z+1)^3 S_z$ (in cm^3 s^{-1}) for direct ionization (d) (dashed line) plus autoionization (a) (dotted) (solid line indicates total rate) of ion Z^{+z} as a function of reduced electron temperature $T/(z+1)^2$ from Arnaud & Rothenflug (1985) (e.g., $z{=}7$ for ionization of O VIII, etc.) (from Mewe 1990).

In Figs. 4 and 5 I have presented, for a number of representative cases covering both low- and high-Z ions, the results of Arnaud & Rothenflug (which are often used in the present spectral codes). I show the scaled rate coefficient $(z+1)^3 S_z$ for ionization of ion Z^{+z} as a function of the reduced temperature $\Theta = T/(z+1)^2$. In cases where the contribution from autoionization becomes also important, I have indicated this in the figure. I estimate that in many cases the rates are good to 10–20% and that the overall uncertainty will be at the level of up to ~40% (cf. also Raymond 1988).

6.1.3 High-density effects on the ionization rates.
Any transition to levels below the TL (see Sect. 4.1.2) is equivalent to recombination, since the hole that is left is immediately populated by a collisional transition from the continuum; similarly, any excitation from low levels to the thermal levels above the TL is equivalent to ionization, since further excitation and ionization dominates downward radiative decay. If the TL is low enough [say $n_t \lesssim 5$, corresponding to $n_e \gtrsim 10^{12}(z+1)^{7.5}$] effects of density (e.g., stepwise ionization) on the ionization and recombination rate coefficients should be
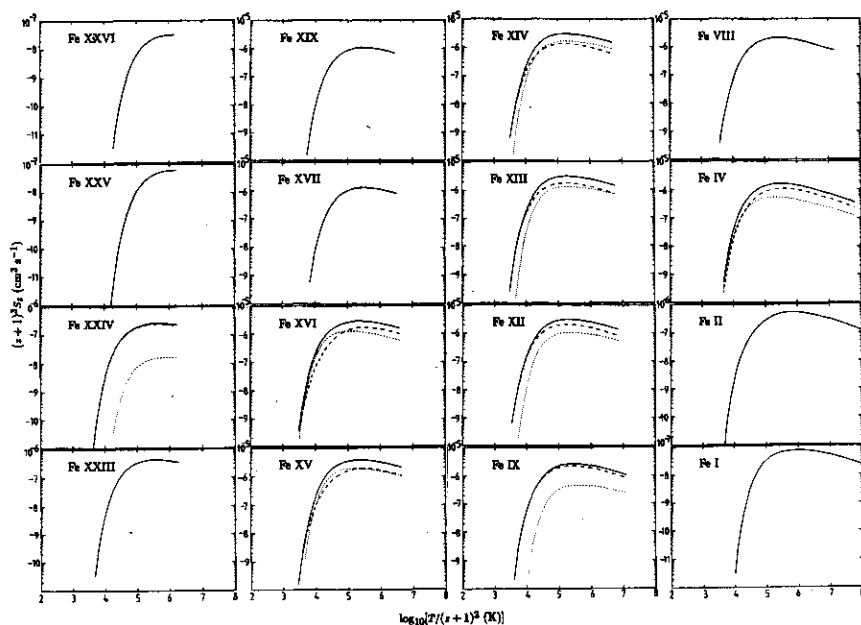
Fig. 5. Reduced ionization rate coefficients for a number of ionization stages of iron. For explanation see caption to Fig. 4.

taken into account. In certain cases where metastable levels are important (e.g., low-Z Li-, Be-, and B-like ions) stepwise excitation-ionization can occur already at much lower densities (e.g., Vernazza & Raymond 1979).

Bates et al. (1962a,b) were the first to make calculations fully taking into account the combined effects of collisions and radiative decay for the case of an optically thin *or* thick *hydrogenic* plasma. They expressed the net rates of ionization and radiative recombination in terms of binary coefficients which they called "*collisional-radiative*" ionization or recombination coefficients. For the complicated case in which also trapping of resonance radiation becomes important, I have made some rough estimates for these rate coefficients with semi-empirical approximation formulae (based on the results of Bates et al.) for a highly simplified hydrogenic two-level + continuum scheme (Mewe 1970, also 1988). The transition between low- and high-density cases occurs at different densities, roughly at the plasma dimension $D \sim 3 \ 10^{27}(z+1)^{10.5}n_e^{-2}$ cm, which represents the effect of resonance radiation trapping in the case of Doppler broadening.

In the high–density limit the effective rate coefficient ($cm^3 \ s^{-1}$) for ionization of hydrogenic ions $X^{+(Z-1)}$ approaches (cf. Mewe 1970, 1988) (T in K):

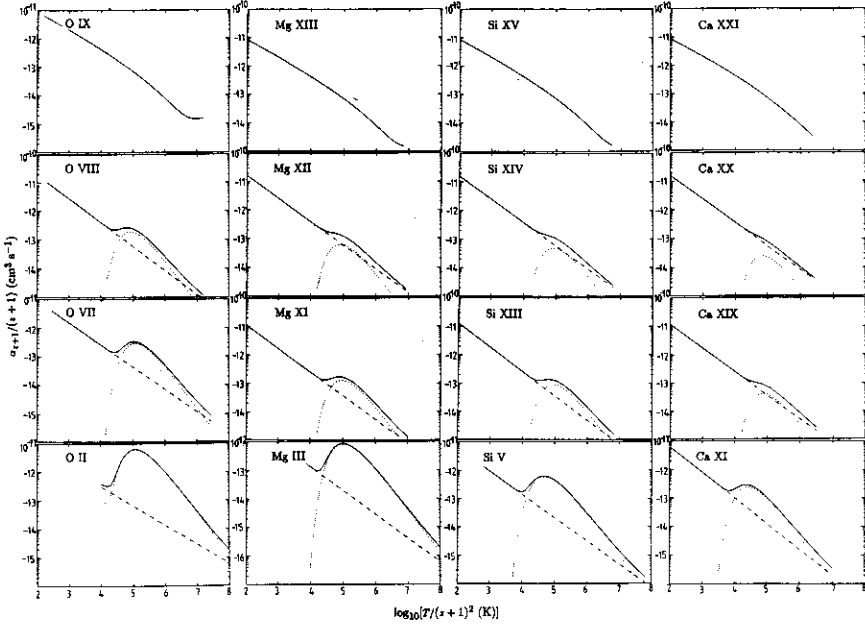$$S_{Z-1}(n_e \to \infty) = 1.3 \ 10^{-5}Z^{-2}T^{-1/2}\exp(-1.184 \ 10^5 Z^2/T) \ , \qquad (25)$$

Fig. 6. Reduced rate coefficients $\alpha_{z+1}/(z+1)$ (in cm^3 s^{-1}) for radiative recombination (RR; dashed line) plus dielectronic recombination (DR; dotted line) of ion $Z^{+(z+1)}$ as a function of reduced electron temperature $T/(z+1)^2$ from Arnaud & Rothenflug (1985) E.g., $z=7$ for recombination of O IX, etc. The solid line indicates the total rate. (from Mewe 1990).

which equals the excitation rate to the first excited level for this simplified model.

7   Rate Coefficients for Recombination

In coronal equilibrium, each ionization is balanced by a recombination process, either radiative or dielectronic. For hot plasmas we can neglect processes of charge transfer, which can be very important for the ionization structure of cooler plasmas, such as photoionized nebulae. The most important charge transfer process is generally the capture of an electron from neutral hydrogen by a charged ion, resulting in recombination of the ion. For temperatures below ~ 0.01 MK this becomes important [see, e.g., Arnaud & Rothenflug (1985), and the review by Butler & Dalgarno (1980)]. Further, I neglect 3–body recombination which is only important at very high densities ($n_e \gtrsim 10^{15} Z^2$ cm^{-3}, cf. Sect. 7.1.1).
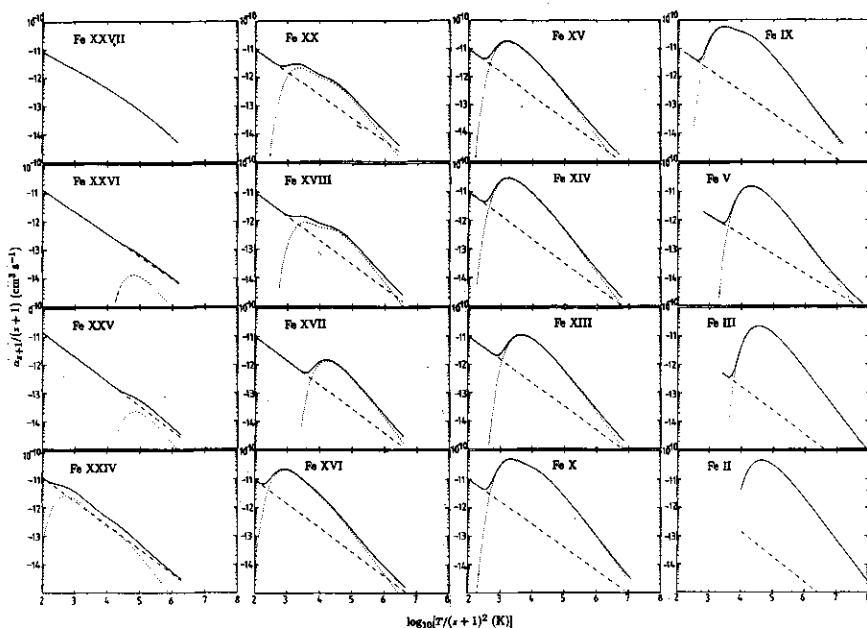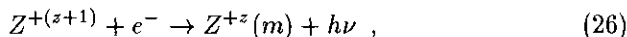
Fig. 7. Reduced recombination rate coefficients for a number of ionization stages of iron. For explanation see caption to Fig. 6.

For low-density plasmas we have (a) the process of *radiative recombination*,

$$Z^{+(z+1)} + e^- \rightarrow Z^{+z}(m) + h\nu \ , \tag{26}$$

where m denotes the m-th state of the recombined ion and (b) the process of *dielectronic recombination* which occurs in the following steps. First an energetic free electron is captured and its kinetic energy is used for the simultaneous excitation of a bound electron into a doubly excited state of ion Z^{+z}:

$$Z^{+(z+1)} + e^- \rightarrow (Z^{+z})^{**} \ . \tag{27}$$
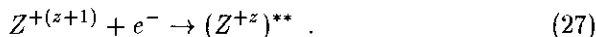
If auto-ionization follows (the reverse of the capture process), the system returns to its original state and no recombination takes place. Alternatively a fraction of the ions in the autoionizing state decays by spontaneous radiative transition of the inner excited electron to a state below the first ionization limit (stabilization process):

$$(Z^{+z})^{**} \rightarrow (Z^{+z})^* + h\nu \ , \tag{28}$$
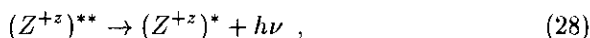
where the stabilizing transition in the recombined ion Z^{+z} results in the emission of a dielectronic satellite line of the parent transition in the recombining

ion $Z^{+(z+1)}$. Eventually, the singly excited state cascades down to the ground state with the subsequent emission of photons:

$$(Z^{+z})^* \rightarrow Z^{+z} + h\nu' + h\nu'' + ... \qquad (29)$$

Though dielectronic recombination (DR) was already recognized by Massey & Bates (1942) as a recombination process wherein radiationless capture of a free electron can occur, its importance was not emphasized until it was shown by Burgess (1964, 1965) that it provides an important additional recombination mechanism in a hot dilute plasma like the solar corona. Taking into account this process he pointed out that as a consequence, a considerably higher temperature is needed to maintain a certain state of ionization, thus solving the outstanding problem of the discrepancy between the ionization temperature and the two to three times higher Doppler line width temperature. Another aspect is, as was first shown by Gabriel (1972), that this process is responsible for the formation of spectral lines appearing as (mostly) long-wavelength satellites to the resonance lines of highly ionized atoms in hot plasmas [see review by Dubau & Volonté (1980) and Sect. 15]. In fact, such lines constitute the only observable effect by which dielectronic recombination manifests itself.

If we write for the total radiative and dielectronic recombination rate coefficients $\alpha^r_{Z,z+1}$ and $\alpha^d_{Z,z+1}$, respectively, then the total recombination rate coefficient (in $\text{cm}^3 \text{ s}^{-1}$) is given by

$$\alpha_{Z,z+1} = \alpha^r_{Z,z+1} + \alpha^d_{Z,z+1} \ , \qquad (30)$$

so that the number of recombinations ($\text{cm}^{-3} \text{ s}^{-1}$) of ion $Z^{+(z+1)}$ is given by $n_e N_{Z,z+1} \alpha_{Z,z+1}$, where n_e and $N_{Z,z+1}$ are the electron and ion densities (in cm^{-3}), respectively. Though we will concentrate on a tenuous plasma, at the end I will briefly describe the influence of stepwise processes on the radiative recombination rate in a hydrogenic plasma of high density.

7.1   Radiative recombination; the Milne equation

Since radiative recombination is the capture of a plasma electron into a bound state of an ion with emission of a photon, this process is inverse to photoionization so that there is a connection between the rates of recombination and photoionization, the so-called Milne relation (cf. Milne 1924; Elwert 1952; Bates & Dalgarno 1962). This relation can be derived by applying the principle of detailed balance (see Sect. 4) in thermal or thermodynamic equilibrium (cf. Rybicki & Lightman 1979), hence assuming a thermal Maxwell electron velocity distribution (Eq. 20) and a Planck radiation field. Since the rate coefficients refer to atomic properties, the relation is generally valid. The power per unit area (perpendicular to the propagation direction), frequency, and solid angle of the blackbody radiation field is given by:

$$B_\nu = \frac{2h\nu^3}{c^2} \frac{1}{e^{h\nu/kT} - 1} \quad . \tag{31}$$

Let $Q^r_{z+1,m}$ be the cross section for radiative recombination of ion $Z^{+(z+1)}$ in the ground state with statistical weight w_{z+1} and density N_{z+1} (cm^{-3}) with an electron of velocity v (or kinetic energy $E = \frac{1}{2}m_e v^2$) towards an ion $Z^{+z}(m)$ in state m with statistical weight $w_{z,m}$. Then the number of recombinations per second and per cm^3 with thermal electrons per velocity interval dv is

$$N_{z+1} n_e Q^r_{z+1,m} f_M(v) v \ dv \quad , \tag{32}$$

where $f_M(v)$ is given by (Eq. 20). On the other hand, the number of photoionizations from state m (in ion Z^{+z} with density $N_{z,m}$) per second and per cm^3 in an isotropic blackbody radiation field B_ν per frequency interval $d\nu$ is

$$\frac{4\pi}{h\nu} N_{z,m} \kappa_{z,m}(\nu) \left(1 - e^{-h\nu/kT}\right) B_\nu \ d\nu \quad , \tag{33}$$

where $\kappa_{z,m}(\nu)$ is the absorption cross section for photo-ionization from state m in ion Z^{+z} and the factor $\left(1 - e^{-h\nu/kT}\right)$ is the correction on the absorption for stimulated emission (which follows immediately from the well-known relations between the Einstein radiation coefficients). Then equating expressions (32) and (33), using Eq. (20), Eq. (31), the Saha-Boltzmann equation [i.e., Eq. (6) with $N_z \to N_{z,m}$, $\chi_z \to \chi_{z,m}$, and $w_z \to w_{z,m}$], using energy conservation for non-relativistic electrons $[\mathrm{d}(h\nu) = \mathrm{d}(\frac{1}{2}m_e v^2)$ or $h\mathrm{d}\nu = m_e v \mathrm{d}v]$ and $h\nu = E + \chi_{z,m}$ is the energy of the emitted photon ($\chi_{z,m} = h\nu_m$ is the ionization energy from state m, ν_m is the frequency of the absorption edge), we finally obtain the *Milne relation*:

$$\frac{Q^r_{z+1,m}}{\kappa_{z,m}(\nu)} = \frac{(h\nu)^2}{2E m_e c^2} \frac{w_{z,m}}{w_{z+1}} = 1.3313 \ 10^{-5} \frac{(h\nu)^2}{E E_H} \frac{w_{z,m}}{w_{z+1}} \quad , \tag{34}$$

where E_H is the ionization energy of hydrogen. This is an important relation that is used to calculate recombination rates from photoionization data.

For a hydrogenic ion of nuclear charge Z, in a state with principal quantum number m the absorption cross section (in cm^2) is given by the Kramers-Gaunt formula (Elwert 1952; Kramers 1923; Gaunt 1930)

$$\kappa_m(\nu) = 7.9 \ 10^{-18} \ m Z^{-2} f_1 (\nu_m/\nu)^3 \ (\nu \geq \nu_m) \quad , \tag{35}$$

where f_1 is the Gaunt correction factor of order unity ($f_1 = 0.8$ for $m = 1$, 0.9–1 for $m > 1$); $\kappa_m(\nu) = 0$ for $\nu < \nu_m$. Combining Eqs (34) and (35) and omitting subscripts we obtain for the recombination cross section (in cm^2)

$$Q^r(U) = 2.10 \ 10^{-22} \ f_1 m [U(U+1)]^{-1} \quad , \tag{36}$$

where $U = E/\chi_m$. The recombination rate coefficient α^r (in $\mathrm{cm}^3 \ \mathrm{s}^{-1}$) can be obtained by integrating vQ^r over a Maxwellian electron distribution (see Eq. 19), but taking the electron threshold energy $E_0 = 0$ and $y = \chi_m/kT$:

$$\alpha^r = \langle vQ^r \rangle = \int_0^\infty v f_M(v) Q^r(v) \, \mathrm{d}v =$$

$$6.21 \ 10^5 \ T^{1/2} y^2 \int_0^\infty Q^r(U) e^{-yU} U \, \mathrm{d}U \ , \tag{37}$$

or inserting Eq. (36)

$$\alpha^r(m) = 2.06 \ 10^{-11} \ f_1 m^{-1} Z^2 T^{-1/2} G_1(\chi_m/kT) \ , \tag{38}$$

with T in K and $G_1(y) = y e^y E_1(y) \simeq y \ln[(y+1)/y] \approx 1 \ (y \gg 1)$ (see Eq. 72). To obtain the total rate we have to sum over all states m.

Seaton (1959) derived a formula for the total radiative recombination rate towards hydrogenic ions which is based on an expansion of the Kramers-Gaunt factor:

$$\alpha^r = 5.197 \ 10^{-14} Z \lambda^{1/2} [0.4288 + 0.5 \ln(\lambda) + 0.469 \lambda^{-1/3}] \ , \tag{39}$$

where $\lambda = 157890 Z^2/T$ (T in K). This expression which is accurate to 3% for $T \leq 10^6 Z^2$, is used in the calculations by Arnaud & Rothenflug (1985).

For recombination towards non-hydrogenic ions in excited states ($m > m_0$) one can also use the hydrogenic approximation since with increasing m excited states readily approach hydrogenic ones, but for the recombination towards the ground state (m_0) we can evaluate the recombination coefficient from the cross section of photoionization from the ground state (e.g., Reilman & Manson 1979; also Pradhan 1987) using the Milne relation (Eq. 34). A number of authors, e.g., Aldrovandi & Péquignot (1973) and Arnaud & Rothenflug (1985) applied this and made simple power law fits in temperature to the resulting recombination rates. For references, see Verner & Ferland (1996) who have made more sophisticated fits to the photoionization cross sections and recombination rates. As an example, I present in Figs. 6 and 7 some representative results of Arnaud & Rothenflug (1985). The estimated overall uncertainties are probably at the level of 30–40% (see discussion by Raymond 1988).

For the general case of non-hydrogenic ions we can use the Milne relation when photoionization rates are available (see Sect. 5.2.2), but for making first-order estimates we may use the approach of Elwert (1952) who replaced in this case Z by the effective nuclear charge z_e, defined by $\chi_{m_0} = E_H z_e^2/m_0^2$, where χ_{m_0} is the energy of ionization of the recombined ion Z^{+z} in the ground state with principal quantum number m_0 (e.g., for the hydrogenic case $z_e = Z$ and $m_0 = 1$), and introduced a correction factor G to account for the recombination to excited states. Then (omitting subscript Z) we obtain for the total radiative recombination rate coefficient (cm^3 s^{-1}) :

$$\alpha_{z+1}^r = 2.06 \ 10^{-11} (G/m_0) G_1(\chi_{m_0}/kT) z_e^2 T^{-1/2} \approx 3 \ 10^{-11} \ z_e^2 T^{-1/2} \ , \tag{40}$$

where $G \simeq 1 + 0.37 m_0 + 0.25 m_0^{1.36} (\chi_{m_0}/kT)^{0.43}$ and T is in K. This expression shows that radiative recombination rates in dependence of reduced temperature $\Theta = T/z_e^2$ scale $\propto z_e$. For a global estimate we can use the right-hand approximation within about 15% for $\chi_{m_0}/kT \gg 1$.

7.1.1 High-density effects on the radiative recombination rates.
Analogously to the calculation of the collisional–radiative ionization rate co-efficient (see Sect. 6.1.3) we consider the effect of high density on recombination. In the high-density limit the rate coefficient ($cm^3 s^{-1}$) for recombination towards hydrogenic ions $Z^{+(Z-1)}$ approaches (n_e in cm^{-3}, T in K) (Mewe 1970, 1988):

$$\alpha_Z(n_e \to \infty) = 5.37 \ 10^{-21} \ Z^{-2}T^{-2}n_e \exp(3.946 \ 10^4 Z^2/T) \ , \qquad (41)$$

which is $\propto n_e$ and equal to the 3–body recombination rate. The latter is directly related to the inverse process of ionization (Eq. 25) by the principle of detailed balancing (Sect. 4) so that the ratio of Eq. (25) and Eq. (41) yields indeed the Saha ionization balance equation (Eq. 6).
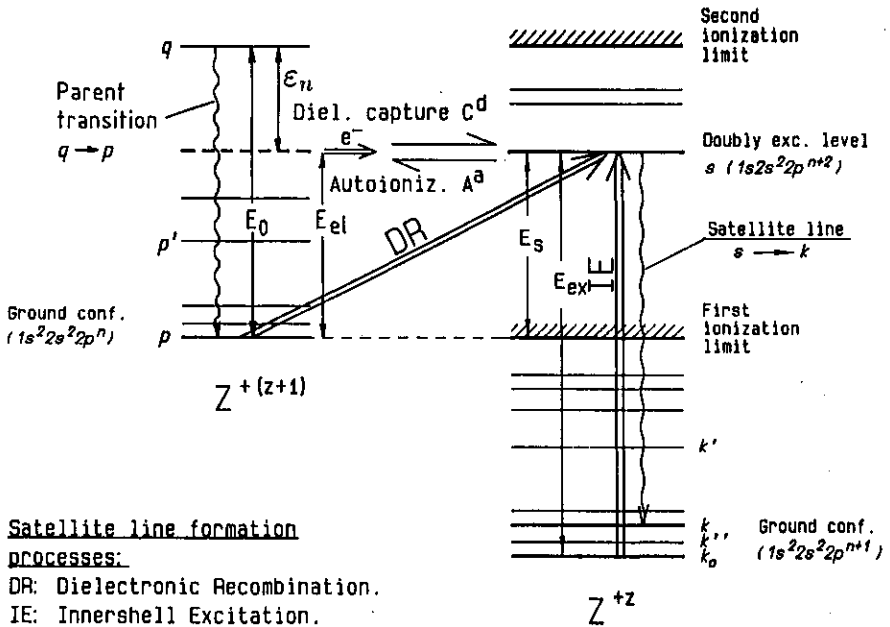
Fig. 8. Energy level diagram showing the dielectronic capture of an electron into a doubly excited level $s = q, n\ell$ and the subsequent formation of a dielectronic recombination (DR) satellite line $s \to k$ in ion Z^{+z}. Here the doubly excited level s is formed by the DR of ion $Z^{+(z+1)}$ in one of its ground configuration levels p (= ground state 1 for a low-density plasma). An alternative population process is electron impact inner-shell excitation (IE) (energy $E_{ex} \simeq E_0$) of ion Z^{+z} from one of its ground configuration levels k'' (= presumably the ground state k_0). De-excitation of state s occurs either radiatively towards levels $k' < s$ (e.g., $k = p, n\ell$) to form the DR satellite line $s \to k$) or by auto-ionization towards levels $p' < s$.

7.2   Dielectronic recombination

The recombination of many coronal ions, however, is dominated by dielectronic recombination (for reviews, e.g., Hahn 1985; Hahn & LaGattuta 1988; Bell & Seaton 1985).

Dielectronic recombination (DR) can be considered as a two-step process illustrated in Fig. 8.[9] It is initiated by the resonant radiationless capture of an energetic plasma electron by an ion $Z^{+(z+1)}$ into a high Rydberg state $n\ell$ of ion Z^{+z}, accompanied by the excitation $p \to q$ of one of the bound electrons in the core of the recombining ion $Z^{+(z+1)}$, thus forming a doubly excited state in ion Z^{+z}:

$$Z^{+(z+1)}(p) + e^- \to Z^{+z}(q, n\ell) \ . \tag{42}$$
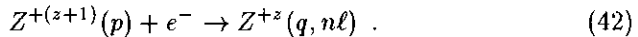
The initial state p of the recombining ion $Z^{+(z+1)}$ is usually the ground state in the coronal approximation. The high Rydberg electron $(n\ell)$ is just a "spectator" as far as the radiation of the core electron is concerned. Thus, an electron is incident on ion $Z^{+(z+1)}$ with an energy $E_{el} = E_s = E_0 - \varepsilon_n$ just ε_n less than the threshold energy E_0 needed to excite the core electron. As it approaches the ion, it gains kinetic energy in the Coulomb field of the ion, so that close in it has sufficient energy to excite the bound inner core electron, but if it does so, it has not enough energy to escape, and is bound in Rydberg level $(n\ell)$ with binding energy $\varepsilon_n = E_H z^2/n^2$. Since there is an infinite number of Rydberg states, the DR capture cross section versus electron energy consists of a corresponding series of narrow resonances located just below the threshold for core-electron excitation (cf. also Sect. 8.1).

Once the ion is in the doubly excited state $s = q, n\ell$ (which is above the first ionization limit), having one electron removed from an inner shell, it has *two options*. It may return to a state of lower energy by ejecting one of its own electrons without the emission of radiation. This internal conversion process in which the energy of the excited core electron is again transferred to the Rydberg electron (the reverse of the capture process) is called the *Auger effect*. Then the electron leaves and *autoionization* occurs. Alternatively, the vacancy in the inner shell is filled by an electron from a less tightly bound state (this process may be successively repeated until all the excess energy of the ion has been radiated). The excited core electron radiates the excess energy away as fluorescence radiation and is captured so that *dielectronic recombination* occurs. The doubly excited state $s = q, n\ell$ undergoes a stabilizing radiative transition (satellite line $s \to k$) directly (or eventually via several cascades) towards a final state $k = p, n\ell$ that lies below the first ionization limit of the recombined ion:

$$Z^{+z}(q, n\ell) \to Z^{+z}(p, n\ell) + h\nu \ . \tag{43}$$

---

[9] The ion $Z^{+(z+1)}$ in this diagram may represent one of the Fe XVIII–Fe XXIII ions for which the parent resonance line $2p \to 1s$ occurs in Fe XXV.

The *satellite* line $(h\nu)$ $s \to k$ in ion Z^{+z} is slightly shifted to the long-wavelength side of the corresponding parent $q \to p$ transition in the recombining ion $Z^{+(z+1)}$ due to the electrostatic shielding by the spectator electron.

Finally, the singly excited state $k = p, n\ell$ eventually cascades down to the ground state $k_0 = p, n_0\ell_0$ [i.e. the spectator electron makes the transition $n\ell \to n_0\ell_0$ and $Z^{+z}(p, n\ell) \to Z^{+z}(p, n_0\ell_0) + h\nu'$].

The dielectronic capture rate C_s^{d} (in cm^3 s^{-1}) to level s with statistical weight $w_s = 2(2\ell + 1)$ is directly related to the inverse process of autoionization from level s (rate A_s^{a} in s^{-1}) towards the ground state (statistical weight w_1) of the recombining ion $Z^{+(z+1)}$ by applying the principle of *detailed balancing* in thermodynamical equilibrium (cf. Sect. 4):

$$N_{z+1}^* n_{\mathrm{e}} C_s^{\mathrm{d}} = N_{z,s}^* A^{\mathrm{a}} \ , \tag{44}$$

where $N_{z,s}^*$ and N_{z+1}^* are the *fictitious* densities of the satellite level (s in the recombined ion Z^{+z}) and of the recombining ion ($Z^{+(z+1)}$) given by the Saha-Boltzmann equation (cf. Eq. 6) with w_{z+1}/w_z replaced by w_1/w_s). Then we immediately obtain for the dielectronic capture rate (cf. also Gabriel 1972; Dubau & Volonté 1980):

$$C_s^{\mathrm{d}} = 2.071\ 10^{-16} T_{[\mathrm{K}]}^{-3/2}(w_s/w_1) A^{\mathrm{a}}_{[\mathrm{s}^{-1}]} \exp(-E_s/kT) \ (\mathrm{cm}^3\ \mathrm{s}^{-1}) \ , \tag{45}$$

where E_s is the energy difference between the autoionizing state s and the ground state of the recombining ion which is just the kinetic energy $E_0 - \varepsilon_n$ of the plasma electron being captured. This relation is valid as long as the plasma electrons have a Maxwellian energy distribution, since C_s^{d} and A_s^{a} are atomic rate coefficients relating two exactly inverse processes. For the dielectronic rate coefficient we can write:

$$\alpha^{\mathrm{d}}(s) = C_s^{\mathrm{d}}\ BR_s \ , \tag{46}$$

where

$$BR_s = \frac{A_s^{\mathrm{r}}}{A_s^{\mathrm{a}} + \sum A_s^{\mathrm{r}}} \ , \tag{47}$$

the branching ratio for the dielectronic recombination channel where A_s^{r} is the radiative decay rate for the satellite line $s \to k$ with the summation over all possible radiative transitions from the satellite level s. By summing over all possible resonant autoionizing Rydberg states $s = n\ell$ we obtain the total DR rate coefficient (cm^3 s^{-1}) (e.g., Bely-Dubau et al. 1979):

$$\alpha^{\mathrm{d}} = \sum_s \alpha^{\mathrm{d}}(s) = 2.071\ 10^{-16} T^{-3/2} \sum_s B_s \mathrm{e}^{-E_s/kT} \ , \tag{48}$$

where

$$B_s = \frac{w_s A_s^{\mathrm{a}} A_s^{\mathrm{r}}}{w_1(A_s^{\mathrm{a}} + \sum A_s^{\mathrm{r}})} \ . \tag{49}$$

The behaviour of the DR rate depends sensitively on the branching ratio BR, i.e. on the relative magnitudes of A^a and A^r. The A^a can be found by extrapolating the $p \to q$ excitation cross section below threshold. They vary as n^{-3} (e.g., Hahn & LaGattuta 1988). For small n, A^a is likely to be much larger than A^r for the values of ℓ which contribute strongly, and α_{DR} is then $\propto A^r$. As along an isoelectronic sequence the radiative transition probability scales as $A^r \propto Z^4$ (for $\Delta n \neq 0$ transitions), it turns out that for low-Z ions (say $Z \lesssim 10$), A^a still exceeds A^r for large n values up to several hundred (and ℓ values up to ~ 6), so that many resonant Rydberg states will contribute. However, as Z increases (say $Z \gtrsim 20$), A^a already becomes smaller than A^r for smaller n, and DR from lower states becomes increasingly important. For instance, recombination of Fe XXV ($Z = 26$) occurs primarily through the $n = 2$ shell (Bely-Dubau et al. 1979). For a given (n, ℓ), $A^r(n, \ell)$ is nearly constant with n and ℓ (because the Rydberg electron is effectively only a spectator as far as the core-excited electron is concerned), whereas $A^a(n, \ell) \propto n^{-3}$. For low n and l, $A^a \gg A^r$, then $BR \propto A^r n^3 \propto n^3$, and $\alpha_{DR}(n, \ell) \propto g_s A^a BR \propto (2\ell + 1)A^r$. Furthermore, $A^a(n, \ell)$ decreases rapidly with ℓ [e.g., $\propto \exp(-0.25\ell^2)$], effectively cutting off the contribution from large ℓ (say above $\ell = \ell_c$ between 5 and 10), since for $A^a \ll A^r$, $\alpha_{DR} \propto A^a$. Thus, though (especially for low-Z ions) there is a large number of resonances which *could* contribute to DR (*if* their autoionization rates were larger) $\propto \sum_{\ell=0}^{n-1} 2(2\ell+1) = 2n^2$, only ℓ's for $\ell \lesssim \ell_c$ (i.e., $A^a \gtrsim A^r$) will contribute $\propto 2(\ell_c + 1)^2$ (e.g., for $n=20$ and $\ell_c=10$ only 200 states out of the possible 800). This is due to the strong decrease of A^a with ℓ.

Burgess (1964, 1965) was the first to compute DR rates and fit the results to a general semi-empirical formula, similar to the expression (48), later corrected by Burgess & Tworkowski (1976). The expected accuracy was $\sim 30\%$ and the formula is probably valid only near the temperature T_m at which the ion concentration peaks. For $T \gg T_m$ DR rarely matters, but for very low temperatures ($T \ll T_m$), it can be quite important in photoionized plasmas or in rapidly cooling gas. For low temperatures Nussbaumer & Storey (1983) have computed DR rates for abundant elements up to Si. The Burgess approximation is best for $\Delta n = 0$ inner-electron transitions and modified versions of the formula have been proposed for $\Delta n \neq 0$ transitions (Merts et al. 1976; Hahn 1985). Another modification, as was first pointed out by Jacobs et al. (1977), is the inclusion of additional autoionizing decay channels of the doubly excited state into *excited* states of the recombining ion (auto-ionization not always occurs only via the true inverse radiationless capture, i.e., into the channel associated with the ground state of the recombining ion). For certain ions this can drastically reduce the DR rate. Though the Jacobs rates are good for low-Z ions, the Jacobs correction may seriously underestimate the rates for high-Z ions [e.g., a factor ~ 2–3 for recombination of Fe XVII (Smith et al. 1985)]. It appears that the disagreement among various computations allows an overall accuracy of only $\sim 40\%$ [see discussion by Raymond (1988)].

Unfortunately, for dielectronic recombination rates there is less experimental guidance than for ionization rates, because the crossed-beam experimental results suffer from the influence of electric fields experienced by ion beams crossing a magnetic field (e.g., Hahn 1985). This causes field ionization that limits the value of n to ~ 30, but more importantly, Stark mixing of different l levels of a given n state, which may cause a dramatic enhancement of the experimental cross section for low-Z ions of up to an order of magnitude compared to the computed zero-field case (see also Sect. 7.2.2).

Arnaud & Rothenflug (1985) have evaluated many theoretical data and updated them in a number of cases. Figs. 6 and 7 present their results for the radiative recombination (RR) and dielectronic recombination (DR) rate coefficients in a reduced form, i.e. $\alpha_{z+1}/(z+1)$, as a function of the reduced temperature $\Theta = T/(z+1)^2$. This scaling is appropriate for RR (see Eq. 40), but seems also reasonably valid for DR (Summers 1974; Hahn et al. 1980). It is seen that dielectronic recombination becomes increasingly important for lower Z and at higher temperatures, whereas for the higher ionization stages of high-Z ions radiative recombination becomes dominant.

7.2.1 High-density effects on the dielectronic recombination rates. Dielectronic recombination rates can be affected by the density: at increasing density the DR rate will be reduced by the ionization of the highly excited $n\ell$ states. The magnitude of this suppression has a fairly weak n_e dependence and roughly scales as $\sim (n_e/(z+1)^7)^{0.25}$ (e.g., Burgess & Summers 1969; Summers 1974). It will be most important for the lower-Z ions which emit UV emission lines rather than for the X-ray emitting ions (Raymond 1988). The effects set in roughly for $n_e \gtrsim (10^3-10^4)(z+1)^7$ cm^{-3}.

7.2.2 Inaccuracies: effects of electric fields. Several crossed-beam experiments for singly ionized atoms have shown that dielectronic recombination (DR) is very sensitive to electric fields. The results show that the measured DR rates are a factor of $\sim$5–10 larger than the predicted ones for lower ions (e.g., Müller et al. 1987). This strong discrepancy was explained in terms of the effect of an electric field E_{el} of $\sim$ 10–100 V/cm that cuts off the high $n\ell$ Rydberg states by field ionization but causes Stark mixing of different ℓ levels for lower n, resulting in a net enhancement of the DR rate by nearly an order of magnitude for lower ions. In the experiment, a magnetic field $B \sim$200 Gauss was used to focus the electron beam. The ions which cross the electron beam with velocities $v \sim 10^7$ cm/s then experience in their rest frame a Lorentz field $E_{el} = 10^{-8}vB \approx 20$ V/cm, sufficient to produce full Stark mixing. As A^a decreases with ℓ the result of mixing high- and low-ℓ levels is that A^a is increased for high ℓ and decreased for low ℓ, thus flattening the $A^a(\ell)$ versus ℓ curve, so that more states effectively participate in the recombination process, and the DR cross section is increased.

In the actual plasma environment the mean thermal drift $v_\perp \sim \sqrt{2kT_i/m_i}$ of ions (i) across a magnetic field B can indeed generate such Lorentz electric fields. For $E_{el} \gtrsim 20$ V/cm this reduces to $B_{[G]}\sqrt{T_{i[MK]}/M_i} \gtrsim 90$, which, e.g., for $M_i \sim 20$ and $T_i \sim 1$ MK implies $B \gtrsim 400$ G. Magnetic fields on the order of this value can exist in solar or stellar coronal loop structures and much higher values ($\sim$1000 G) in the lower chromosphere. As the effect is only important for the lowly ionized atoms, it can play a role in cool ($\lesssim 2$ MK) coronal or photoionized plasmas.

Mewe (1990) made an attempt to visualize this effect using a simple schematic model as given by Müller et al. (1987). The typical enhancement factor for the DR recombination of ion $Z^{+(z+1)}$ due to full Stark mixing was approximated by $f = 1 + 10 \; (z + 1)^{-1.15}$. The results show that the effects are most noticeable for the lower ions (where many n states take part in the DR process) formed at low ($\lesssim 2$ MK) temperatures (cf. his Fig. 4 in which a comparison is made for ion fractions of oxygen and iron calculated with and without correction for ℓ-level Stark mixing).

III. Formation of X-ray Spectra in a Coronal Plasma

The overall appearance of the X-ray spectra will be dominated by the ionization structure which varies dramatically with temperature throughout the range 0.1–100 MK.

In extremely hot ($T > 100$ MK) plasmas all abundant elements are nearly fully ionized and the X-ray emission is dominated by the free-free continuum from hydrogen and helium. With decreasing temperature, the heavier trace elements are only partly ionized, beginning with iron, and spectral emission lines excited by electron collisions show up and will begin to dominate the X-ray spectrum. This is especially true for the Fe L-shell lines around 10 Å, the Fe K-shell lines at ~ 2 Å and the Fe $2s$–$2p$ lines around 100 Å. In a wide temperature range (0.01–10 MK) the X-ray spectra of optically thin sources are rich in emission lines from many ions. The spectral lines are broadened mainly by Doppler broadening.

The wavelength band 1–140 Å contains a multitude of prominent lines from nearly all ionization stages of cosmically abundant elements, including the K-shell transitions of carbon through iron, and the L-shell transitions from silicon through iron. If suitably resolved, these lines are powerful diagnostics of plasma parameters because the line strengths are generally very sensitive to the electron temperature, the elemental abundances, and in some cases to the electron density. In certain circumstances (e.g., transient plasmas) the line intensities are dependent on deviations from the ionization equilibrium or on deviations from a Maxwellian electron energy distribution (e.g., Mewe 1990).

The emission line spectra and continua from optically thin plasmas are fairly well known from calculations (for reviews, e.g., Raymond 1988; Mewe

1990, 1991; for examples of measured and simulated spectra see also the Chapters by Paerels and by Kaastra). Comparison of measured line fluxes with known theoretical line emissivities yields the differential emission measure distribution as a function of temperature of the source, which is an essential first step in building a model for a stellar corona and assessing the important terms in the coronal energy balance. Therefore, high-resolution X-ray spectroscopy has its most obvious application in diagnosing optically thin sources such as the coronae of late-type stars.

I consider the processes that produce the line and continuum radiation, in particular the electron impact excitation of spectral lines and the formation of so-called satellite lines. The possibilities for the diagnostics of temperature, density, differential emission measure, abundances, and velocities have been described in more detail elsewhere (Mewe 1990, 1991).

8   Line Radiation

The spectral lines that dominate the soft X-ray spectrum and the cooling of astrophysical plasmas at temperatures up to ~ 10 MK are mainly excited by electron collisional excitation from the ground state. Though this is often a good approximation to calculate the stronger (resonance) lines in a low-density plasma, we have to follow a more complicated scheme of processes connecting many more levels (e.g., also fine structure levels) when we consider the effects of electron density on the line intensities (see also the Chapter by Liedahl).

The volume emissivity P_{ji} (phot cm^{-3} s^{-1}) of a particular spectral line transition $j \to i$ in ion Z^{+z} from element of atomic number Z is written as (omitting subscript Z, z):

$$P_{ji} = N_j A_{ji} \ , \tag{50}$$

where N_j is the population density (cm^{-3}) of the ions in the upper line level j and A_{ji} is the probability (s^{-1}) of a spontaneous radiative transition from the upper line level j towards the lower level i. In the general case the level population density is solved from a set of rate equations which read for level j [neglecting processes of photo-excitation and photo-ionization and also transport terms which can be important in a laboratory plasma of finite size (e.g., Düchs & Griem 1966; Peacock 1996)]:

$$\frac{dN_j}{dt} = \sum_{h<j} N_h n_e S_{hj} + \sum_{k>j} N_k (A_{kj} + n_e S'_{kj}) + N_{z+1} n_e \alpha_j^r + N_{z-1} n_e \beta_j^{II}$$

$$- N_j \left[\sum_{h<j} (A_{jh} + n_e S'_{jh}) + \sum_{k>j} n_e S_{jk} + n_e S_j^i \right] \ , \tag{51}$$

where S_{hj} is the rate coefficient for electron impact excitation $h \to j$ (h denotes the lower level) and S'_{kj} the rate coefficient for collisional de-excitation

$k \rightarrow j$ (k the upper level). Furthermore, α_j^r and β_j^{II} are the rate coefficients for recombination and collisional inner-shell ionization (the latter is important in the formation of the He-like forbidden line in a transient plasma, see Mewe & Schrijver 1978b, and Sect. 15.3), which may give a contribution to the population of level j, while S_j^i denotes the rate of collisional ionization from level j. If we assume a *steady state*, i.e. $dN_j/dt = 0$, Eqs (51) reduce for each element to a set of linear algebraic equations describing the statistical equilibrium. Because we neglected the transport terms we have the condition that $\sum_{j=1}^{N} N_j = N_{Z,z}$, the total ion density in charge state z of element Z. The equation of charge conservation can be added to the system, which couples the elements, but in practice, we are interested primarily in the trace elements, which have practically no effect on the charge balance. For each element, the system of equations can be solved for all level populations N_j by using a technique of matrix inversion [the ion densities N_{z+1} and N_{z-1} can be expressed into $N_z \simeq N_g$ via the ionization balance (Eq. 14)].

Even for a transient plasma we can often make the assumption of a steady state because it turns out that in most cases the excited levels come very quickly, i.e. effectively instantaneously, into equilibrium with a particular value of the ion density in the ground state (N_g) corresponding to the current plasma state. Such a state is called a *quasi-equilibrium* or quasi-steady-state (QSS) (cf. McWhirter & Hearn 1963, and the Chapter by Liedahl). I note that a metastable state takes more time to approach a QSS. An additional condition for the quasi-equilibrium is that the excited-level population densities are negligible with regard to the ground state density, so that the densities of the free electrons and the ions remain essentially constant during the time in which the quasi-steady state is established.

So we deal with the steady-state equations and, for convenience, we make the following assumptions (number in parentheses is the number of the corresponding term in the r.h.s. of Eq. 51): we neglect recombination (3), inner-shell ionization (4), ionization (7), collisional de-excitation processes (5) and excitations to higher levels (6); we assume low plasma density, i.e., excited level populations are so low that we can neglect cascades from levels above level j (2), and all excitations from excited levels (i.e., we consider in the first term only excitation from the ground level g and neglect possible effects from metastable levels); $N_g \simeq N_{Z,z}$, i.e. practically all ions are in the ground state. Then Eq. (51) reduces to

$$0 = N_g n_e S_{gj} - N_j \sum_{h < j} A_{jh} \ , \tag{52}$$

which in many situations is a suitable approximation for a coronal plasma. However, in the case where we study density effects on spectral lines, we should consider the more complete set of Equations (51) including sometimes transitions between fine-structure levels (cf. Sect. 13). Equations (50) and (52) yield for the line emissivity (phot cm^{-3} s^{-1})

$$P_{ji} = N_j A_{ji} = N_g n_e S_{gj} B R_{ji} = n_e N_H A_Z B R_{ji} G_{ji}(T) \ , \qquad (53)$$

where $B R_{ji} = A_{ji}/\sum_{h<j} A_{jh}$ is the radiative branching ratio with respect to all lower levels, N_g the ground state population (cm^{-3}) of ion Z^{+z}, and $A_Z = N_Z/N_H$ the abundance of element Z relative to hydrogen (H). Finally, $G_{ji}(T) = \eta_{Z,z}(T)S_{gj}(T)$, where $\eta_{Z,z} = N_{Z,z}/N_Z \simeq N_g/N_Z$ is the fraction of ions from element Z in ionization stage z and $S_{gj}(T)$ the rate coefficient (cm^3 s^{-1}) for electron impact excitation $g \to j$. The function $G_{ji}(T)$ represents the temperature dependence due to the combination of ionization and excitation, and the temperature T_m at which it peaks is called the temperature of *maximum formation* of the given line. For a fully ionized (in H and He) plasma with cosmic abundances (Anders & Grevesse 1989) the ratio N_H/n_e is fixed primarily by the abundances of H and He: $N_H \simeq 0.77 n_e \simeq n_e$, hence $P_{ji} \propto n_e^2$.

8.1   Excitation processes

The formation of line and continuum radiation mainly occurs by the *electron impact* of atoms or ions. The excitation becomes effective when the impinging electron has a speed comparable to or somewhat larger than the orbital velocity of the bound electron in the atom or ion that is to be excited, i.e., this occurs when the energy of the impinging electron $E \gtrsim \Delta E$, the threshold energy for excitation of the ion. For the excitation of an ion the excitation cross section is finite (and generally largest) at threshold owing to the Coulomb attraction that accelerates the impinging electron.

For an ion (e.g., a *proton*) to be effective in exciting an atom or ion, its speed should also be comparable to the orbital speed of the bound electron which implies that its energy should be higher than for an electron by the ratio of proton/electron mass $R_{pe} = m_p/m_e \simeq 1800$. The excitation cross section for proton excitation begins to rise slowly at threshold and attains its maximum roughly at energies of the impinging proton of $\sim R_{pe}\Delta E \gg \Delta E$. In a plasma with equal electron and ion temperatures $T_e = T_i = T$, those ions that are formed in collisional ionization equilibrium (CIE) (Sect. 5) have ionization energies $\chi \sim \Delta E \sim kT$. Hence, in this situation, electrons are by far more effective in the excitation (because $kT_e \sim \Delta E$) than protons (or heavier ions) which rather would need the condition $kT_i \sim R_{pe}\Delta E \gg kT_e$.

However, there are cases where proton excitation is quite important. For instance, in a NEI plasma (cf. Sect. 4.1.3) the situation can occur in which the plasma temperature T suddenly rises and the ionization balance is still frozen in so that kT becomes $\gg \Delta E$, and the protons are more efficient in exciting the ions rather than the electrons for which the excitation cross section drops at least as fast as $\log E/E$. This is, for example, the case in very fast shock waves for which conditions are created where proton excitation is important: behind the shock low-ionization species are immersed in very hot shocked gas so $kT_i \gg \Delta E$.

The condition $kT \gg \Delta E$ is also fulfilled in CIE for the excitation of transitions between closely spaced energy levels in fine structures which affects the density sensitivity of line intensities. Then proton impact can be important, e.g., by initiating $2s$–$2p$ transitions in H-like ions (Lyman α doublet line) (Zygelman & Dalgarno 1987) or $2s\,^3S$–$2p\,^3P$ transitions in He-like ions (Blaha 1971) (cf. Fig. 13 and Sect. 13).

For further literature, I refer to Raymond & Brickhouse (1996) and to Pal'chikov & Shevelko (1995). The latter authors distinguish in the excitation of ions by electrons,

$$Z^{+z} + e^- \rightarrow (Z^{+z})^* + e^- \ , \tag{54}$$

the following processes:

(i) excitation of outer-shell electrons (cf. Sect. 8.1.1)

$$Z^{+z}(\zeta n\ell^q) + e^- \rightarrow (Z^{+z})^*(\zeta n\ell^{q-1}n'\ell') + e^- \ , \tag{55}$$

(ii) excitation of inner-shell electrons (cf. Sect. 15.3)

$$Z^{+z}(\zeta n\ell^q \xi) + e^- \rightarrow (Z^{+z})^*(\zeta n\ell^{q-1}\xi n'\ell') + e^- \ , \tag{56}$$

and

(iii) resonant excitation (see below)

$$Z^{+z}(\xi_0) + e^- \rightarrow (Z^{+(z-1)})^{**}(\xi n\ell) \rightarrow (Z^{+z})^*(\xi_1) + e^- \ , \tag{57}$$

where ζ and ξ denote a part of the electron configuration and q denotes the number of equivalent electrons of the $n\ell$ shell.

Resonant excitation

Process (57) is a two-step process that is illustrated in Fig. 9. Because of the long-range attractive Coulomb force, a multi-charged ion Z^{+z} can capture a free electron of energy E and create a doubly excited ion $(Z^{+(z-1)})^{**}$:

$$Z^{+z}(\xi_0) + e^- \rightarrow (Z^{+(z-1)})^{**}(\xi n\ell) \ , \tag{58}$$

where the free electron is captured into a high Rydberg state $n\ell$ and an inner core electron of $Z^{+(z-1)}$ is simultaneously excited to state ξ. The excited ion $(Z^{+(z-1)})^{**}$ is unstable and can decay by two competitive channels:

auto-ionization (AI)

$$(Z^{+(z-1)})^{**}(\xi n\ell) \rightarrow (Z^{+z})^*(\xi_1) + e^- \ , \tag{59}$$

or radiative decay (dielectronic recombination, cf. Sect. 7)

$$(Z^{+(z-1)})^{**}(\xi n\ell) \rightarrow (Z^{+(z-1)})^*(\xi_1 n\ell) + h\nu \ . \tag{60}$$

via the emission of a satellite line ($h\nu$) and subsequent cascading ($h\nu'$, $h\nu''$, ...) to the ground state ξ_0.
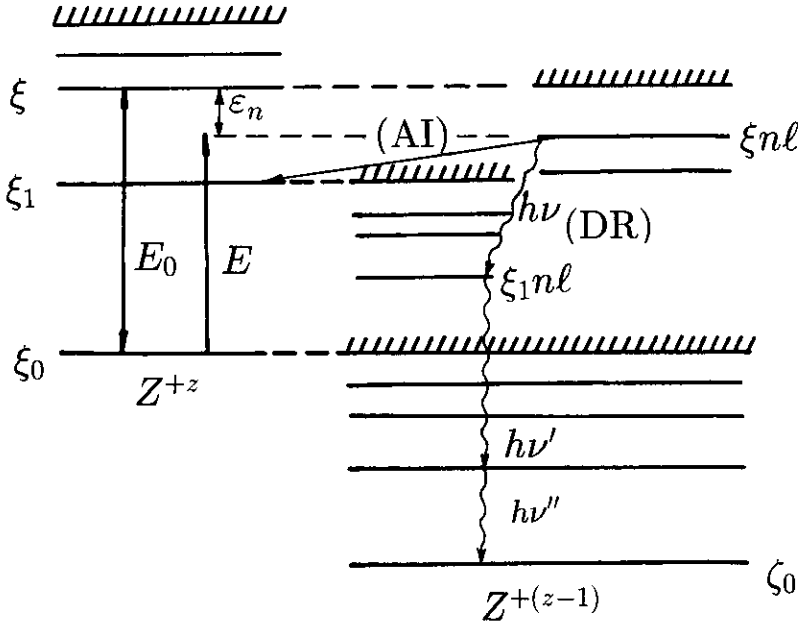
Fig. 9. Energy level scheme and processes for electron resonance capture. AI and DR denote auto-ionization and dielectronic recombination, respectively (from Pal'chikov & Shevelko 1995, with some modifications).

The auto-ionization leads to excitation $\xi_0 \to \xi_1 (\neq \xi_0)$ of the ion Z^{+z} via the intermediate state $\zeta = \xi n\ell$. This excitation process in addition to the usual one is called *resonant excitation* (if $\xi_1 = \xi_0$ it is called resonant elastic scattering).

The resonant capture of an electron is only possible if its energy

$$E = E_0 - \varepsilon_n \simeq E_0 - E_H(z-1)^2/n^2 \ , \tag{61}$$

where E_0 is the threshold energy to excite the core electron in ion Z^{+z} and ε_n is the binding energy of the captured electron in a high Rydberg state $n\ell$.

This leads to the appearance of a series of narrow resonance structures (for different values of n) on top of the "normal" excitation cross section just below the threshold for the core-electron excitation and just above the threshold energy of the normal excitation (cf. Fig. 10). The width of such a resonance is given by the *Heisenberg relation*:

$$\delta E_\zeta = \frac{h}{2\pi}[A_a + A_r] \ , \tag{62}$$

where the sum of the autoionization (A_a) and radiative decay (A_r) probabilities determines the total decay probability of the doubly-excited state ζ.
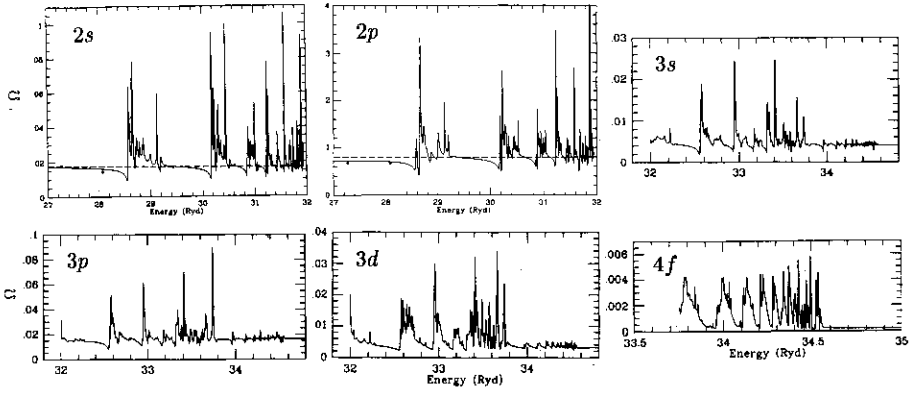
Fig. 10. Collision strengths for excitation of the transitions from the ground state $1s\ ^2S$ in the H-like ion C VI to the $n = 2$ states $2s\ ^2S$ and $2p\ ^2P$, the $n = 3$ states $3s\ ^2S$, $3p\ ^2P$, and $3d\ ^2D$, and to $4f\ ^2F$ (from Aggarwal & Kingston 1991).

Typically, for $[A_a + A_r] \lesssim 10^{14}\ \mathrm{s}^{-1}$, $\delta E_\zeta \lesssim 0.0048$ Rydberg. The contribution of these resonances (smoothed over an electron Maxwellian distribution) should be taken into account for plasmas at relatively low temperatures, but can often be neglected for hot plasmas. Moreover, as the charge of the ion increases, the radiative transition probability ($A_r \propto Z^4$) becomes larger than the autoionization probability ($A_a \sim$ const. in an isoelectronic seq.) so that the branching ratio $A_a/(A_a + A_r) \propto Z^{-4}$ and the resonances will disappear and dielectronic recombination prevails (see discussion by Moores 1988).

8.1.1 Electron impact excitation rate coefficients. The cross section $Q_{ij}(U)$ for electron impact excitation from level i to level j can be written in terms of the *collision strength* $\Omega(U)$:

$$Q_{ij}(U) = \frac{\pi a_0^2}{w_i} \left(\frac{E_H}{E_{ij}} \right) \frac{\Omega(U)}{U} = \frac{\pi a_0^2}{w_i} \left(\frac{E_H}{E} \right) \Omega(E) \ , \qquad (63)$$

where $U = E/E_{ij}$, the impact energy E of the electron expressed in terms of the line excitation energy E_{ij}, and w_i is the statistical weight of the initial lower (often the ground) level. This expression is similar to Eq. (22) with $\alpha = E_{ij}/(w_i E_H)$ and $Q_{red}(U) = \Omega(U)/U$. Note that E_{ij}/E_H is the excitation energy expressed in so-called *Ry(dbergs)* (cf. Sect. 6.1). For optically allowed (electric dipole) transitions we can introduce the concept of the excitation *Gaunt factor* $g(U)$, first introduced by Seaton (1962) and by van Regemorter (1962), which is related to the collision strength by

$$\frac{\Omega(U)}{w_i} = \frac{8\pi}{\sqrt{3}} \frac{E_{\mathrm{H}}}{E_{ij}} \; f \; g(U) = 197.3 \; f \; g(U) \; E_{ij[\mathrm{eV}]}^{-1}$$

$$= 0.01592 \left[\lambda_{[\mathrm{\mathring{A}}]}/a\right] f \; g(U) \; , \qquad (64)$$

where $f_{(ij)}$ is the absorption oscillator strength and λ the wavelength of the line, and $a = E_{ij}/h\nu$, the ratio of line excitation and photon energy ($a > 1$ for a line transition not ending on the ground level). Then the excitation cross section reads as

$$Q_{ij}(U) = \frac{8\pi}{\sqrt{3}} \left(\frac{E_{\mathrm{H}}}{E_{ij}}\right)^2 f \; \frac{g(U)}{U} \; \pi a_0^2 = 14.51 \left(\frac{E_{\mathrm{H}}}{E_{ij}}\right)^2 f \; \frac{g(U)}{U} \; \pi a_0^2 \; . \qquad (65)$$

Note that if g for a given transition is approximately constant in an iso-electronic sequence, the collision strength Ω scales as f/E_{ij}, or $\propto Z^{-2}$, and $Q_{ij} \propto Z^{-4}$ because $E_{ij} \propto Z^2$ [cf. Eqs (64) and (65)].

Integration of vQ_{ij} over a Maxwellian electron velocity distribution (Eq. 20) leads to the *excitation rate* S_{ij} [same as Eq. (21)]:

$$S_{ij} = \sqrt{\frac{8kT}{\pi m_e}} y^2 \int_1^\infty Q_{ij} e^{-yU} U \mathrm{d}U \; , \qquad (66)$$

where $y = E_{ij}/kT$. By defining the Maxwellian-averaged collision strength $\bar{\Omega}(y)$ as

$$\bar{\Omega}(y) = y e^y \int_1^\infty \Omega(U) e^{-yU} \mathrm{d}U \; , \qquad (67)$$

we substitute Eq. (63) into Eq. (66), use Eq. (67) and obtain numerically for S_{ij} in units of cm^3 s^{-1}:

$$S_{ij} = 8.63 \; 10^{-6} \frac{\bar{\Omega}(y)}{w_i} T^{-1/2} e^{-y} \; = \; 1.703 \; 10^{-3} \; f \; \bar{g}(y) E_{ij[\mathrm{eV}]}^{-1} \; T^{-1/2} e^{-y} \; , \qquad (68)$$

where $y = E_{ij}/kT = 1.1604 \; 10^4 \; E_{ij}/T = 1.4388 \; 10^8 \; a/[\lambda T]$, with E_{ij} the line excitation energy in eV, T in K, and λ in Å. Finally, $\bar{g}(y)$ is the excitation Gaunt factor averaged over the Maxwell distribution.

When no data are available one can make a *first-order estimate* of the excitation rate for optically allowed dipole (and sometimes also forbidden) transitions by using the Gaunt factor approximation. With an accuracy of a factor of two or so we may use near threshold ($U \gtrsim 1$) typical values of $g \sim 0.2$ (or 1) for $\Delta n \neq 0$ (or $= 0$) transitions, and at $U \gg 1$ the asymptotic Born-Bethe approximation $g \approx (\sqrt{3}/2\pi) \ln U$. Usually spectroscopists have used as a crude approximation a *constant* Gaunt factor, but one can obtain a generally much better accuracy by introducing an *energy dependence* with a suitable approximation formula.

Fitting formulae for excitation data. Some time ago Mewe (1972) introduced a parametrized interpolation formula for Ω (or g) that represents the correct
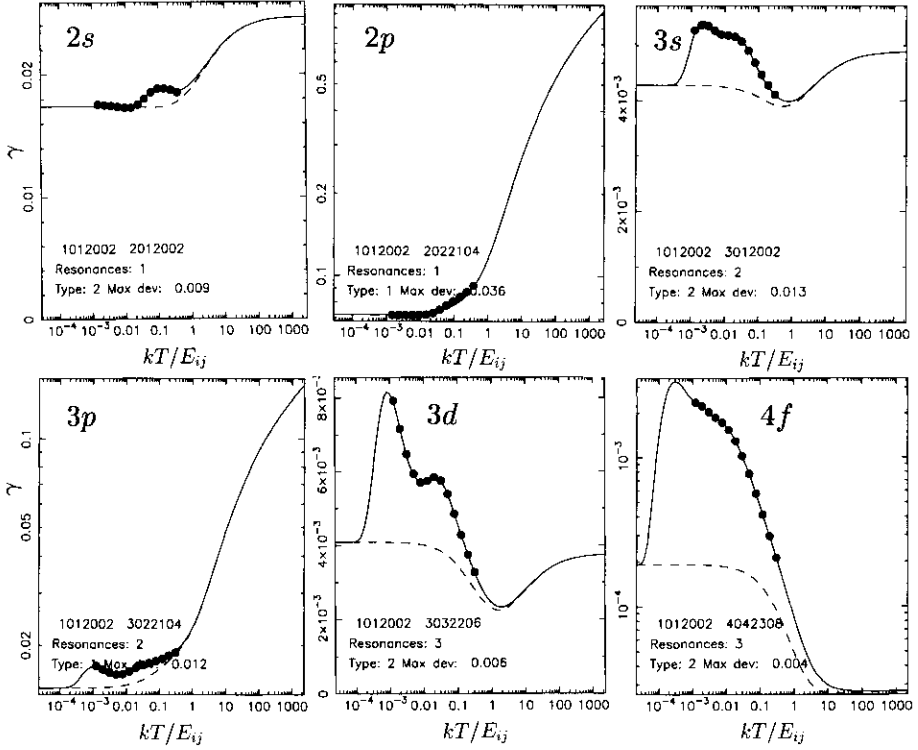
Fig. 11. Fitted effective collision strengths $\gamma = \bar{\Omega}(y)$ (cf. Eq. 67) as a function of $y^{-1} = kT/E_{ex}$ for the transitions from the ground state $1s\,^2$S in the H-like ion C VI to the $n = 2$ states $2s\,^2$S and $2p\,^2$P, the $n = 3$ states $3s\,^2$S, $3p\,^2$P, and $3d\,^2$D, and to $4f\,^2$F (data from Aggarwal & Kingston 1991). The effect of the resonances is taken into account [see the corresponding Fig. 10 for the non-integrated collision strength $\Omega(U)$]. The solid line indicates the collision strength including resonances, while the dashed line gives that without resonances. Various types of fitting formulae (cf. Table 3) are used.

behaviour both near threshold and asymptotically at high energies (cf. also Mewe & Schrijver 1978a):

$$\Omega(U) = A + \frac{B}{U} + \frac{C}{U^2} + \frac{2D}{U^3} + F \ln U \ . \tag{69}$$

This expression can be integrated over a Maxwellian electron energy distribution. The coefficients can be adjusted to fit both calculated collision strengths as well as measured excitation rates. Insertion of Eq. (69) into Eq. (67) gives the collision strength averaged over the electron Maxwell distribution:

$$\bar{\Omega}(y) = A + (By - Cy^2 + Dy^3 + F)\, E^y E_1(y) + (C + D)\, y - Dy^2 \ , \tag{70}$$
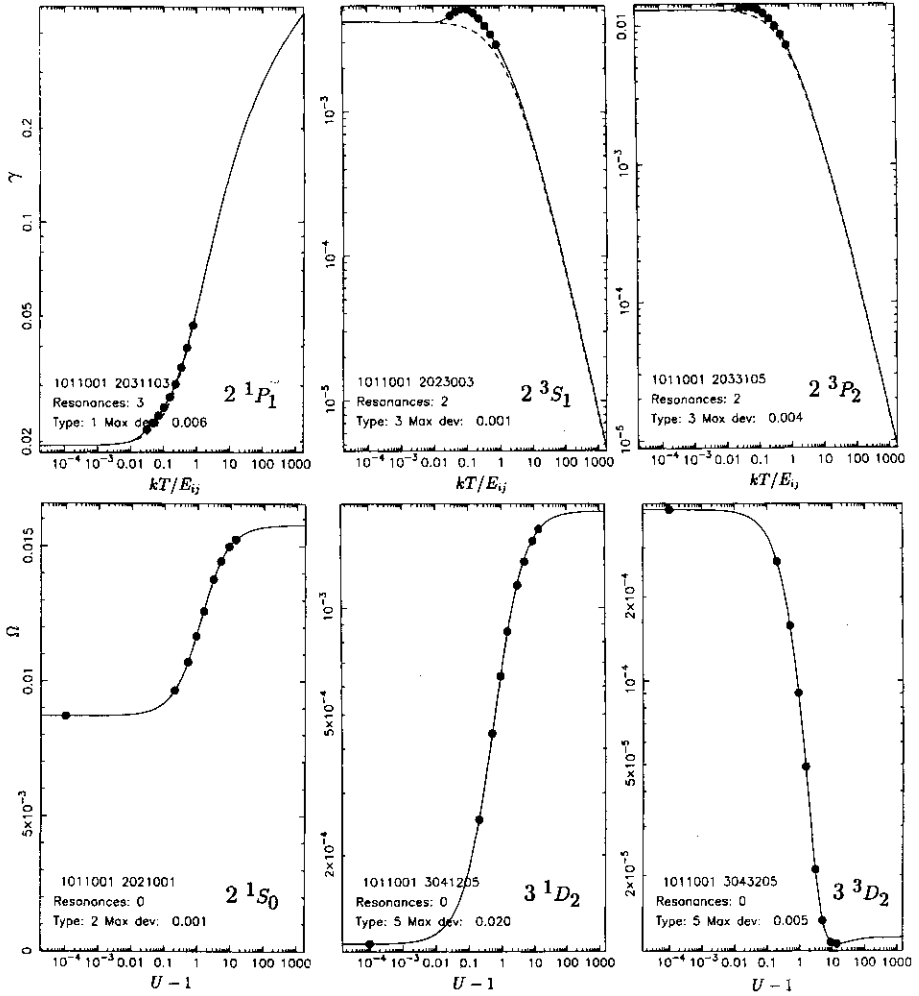
Fig. 12. Fitted effective collision strengths $\gamma = \bar{\Omega}(y)$ as a function of kT/E_{ij} for the transitions from the ground state $1s^2 \, {}^1S_0$ in the He-like ion O VII to the $n = 2$ states $1s2p \, {}^1P_1$, $1s2s \, {}^3S_1$, and $1s2p \, {}^3P_2$, and collision strengths $\Omega(U)$ as a function of $U - 1$ for transitions to the $n = 2$ state $1s2s \, {}^1S_0$ and the $n = 3$ states $1s3d \, {}^1D_2$ and $1s3d \, {}^3D_2$ (data from Sampson et al. 1983, and Zhang & Sampson 1987). In the top three plots the solid line indicates the collision strength including resonances, while the dashed line gives that without resonances.

Table 3. Parameters for fitting formula (75)

Type[a]	c_0	c_1	c_2	c_3	c_4	c_5	c_6	c_7	s
1	+	+	+	+	0	0	0	+	0
2	+	+	+	+	0	0	0	0	0
3	0	0	+	+	+	0	0	0	+
4	+	+	+	+	0	0	0	+	+
5	+	+	+	+	0	0	0	0	+
6	0	0	+	+	+	+	0	0	+
7	0	0	0	+	+	+	+	0	+

a

1: allowed electric dipole transitions
2: forbidden transitions
3: spin-forbidden transitions
4: type 1 + scaling
5: type 2 + scaling
6: forbidden transitions
7: forbidden transitions

where

$$E_1(y) \equiv \int_1^\infty z^{-1} e^{-yz} dz \ , \tag{71}$$

is the exponential integral (cf. Abramowitz & Stegun 1970, Eqs. 5.1.53 and 5.1.54; for $y < 1$, the absolute accuracy is better than 2×10^{-7}; for $y > 1$, the relative accuracy is better than 5×10^{-5}). Mewe & Schrijver (1978a) have introduced a useful approximation (accurate within 0.2% for $y \geq 0.001$):

$$e^y E_1(y) \simeq \ln\left(\frac{y+1}{y}\right) - \frac{0.36 + 0.03(y+0.01)^\alpha}{(y+1)^2} \approx \frac{1}{y+1} \ (y \gg 1) \ , \tag{72}$$

where $\alpha = 0.5$ $(y \geq 1.5)$ or $\alpha = -0.5$ $(y < 1.5)$.

From the approximations for (71) we obtain for the collision strength (and the rate S_{ij} from Eq. 68) near threshold or at asymptotically high energies:

$$\bar{\Omega}(y \gg 1) \simeq \Omega(U = 1) = A + B + C + 2D, \quad S_{ij} \propto T^{-1/2} e^{-y}, \tag{73}$$

and

$$\bar{\Omega}(y \ll 1) \simeq F/y, \quad S_{ij} \propto T^{1/2}. \tag{74}$$

In fitting collision strengths, Eq. (69) can be used in many cases also for forbidden transitions with the logarithmic term put to zero, but sometimes

it is necessary to introduce higher-order terms $\propto 1/U^n$ ($n \geq 4$) and a *scale factor s* by substituting $U \rightarrow U + s$. Kaastra & Mewe have recently developed a fitting routine which incorporates a more complicated fitting formula for Ω (or S, Q, g):

$$\Omega(U) = \sum_{i=0}^{i=6} \frac{c_i}{(U+s)^i} + c_7 \ln U \ . \tag{75}$$

In Table 3 I indicate when the coefficients c_i and the scale parameter s are non-zero (indicated by a $+$) or zero for various types of transitions.

Note that the fitting procedure can also take into account the contribution from possible *resonances* near the threshold of excitation which can be important for the calculation of excitation rates for cool plasmas.

Figs. 11 and 12 give examples of fitting results for the H-like ion C VI and the He-like ion O VII, respectively. Clearly the effect of resonances shows up in various cases. Different types of fitting formulae are used (cf. Eq. 75 and Table 3). In the case of the first three transitions in O VII (fit to γ in Fig. 12) we have applied a combined fitting to the data of Sampson et al. (1983) (without resonances) and those of Zhang & Sampson (1987) (including resonances). The effect of resonances is clearly seen, e.g., in the 3s, 3d, and 4f excitation in C VI and the 2^3S excitation in O VII.

More complex expressions for the line formation in an optically thin plasma (cf. Eq. 51), including possible cascade effects on the excitation rate and also contributions from recombination ($\propto \eta_{z+1}$), inner-shell ionization ($\propto \eta_{z-1}$) and unresolved dielectronic recombination satellite lines ($\propto \eta_z$) have been given elsewhere (Mewe & Gronenschild 1981; Mewe et al. 1985a).

8.1.2 De-excitation rates. The rate coefficient S'_{ji} of de-excitation $j \rightarrow i$ is related to S_{ij}, the rate coefficient of the inverse excitation process $i \rightarrow j$ by

$$S'_{ji} = \frac{w_i}{w_j} e^{E_{ij}/kT} S_{ij} \ , \tag{76}$$

where w_i and w_j are the statistical weights of the lower level i and the upper level j, respectively. This relation immediately follows by applying the principle of detailed balance (Sect. 4) and the Boltzmann equation for the ratio of the fictitious population densities of levels i and j.

8.1.3 Accuracy of excitation rates. Though in a number of cases the Gaunt factor approximation method gives reasonably accurate results, more accurate values are needed, especially for the weaker lines and optically forbidden transitions. Raymond (1988) gives a brief discussion of the accuracy of several computational methods such as Coulomb-Born (CB) and Distorted Wave (DW) approximations, and the more accurate Close Coupling (CC) method, which properly takes into account the dominant resonances near the

threshold of the excitation mentioned in connection with DR. [For a theoretical review see Seaton (1975), for a review on crossed-beam experiments see Dolder & Peart (1986), and for a review on plasma measurements of atomic rates see Griem (1988)].[10] CB tends to overestimate the collision strength near threshold by $\sim$20–50%, while DW gives better results, especially for high-Z ions. Few accurate CC results are available for He-like ions (Kingston & Tayal 1983). For many of the strongest X-ray lines, e.g., from H- and He-like ions and Li- to Ne-like ions, the collision strengths are known with better than 20% accuracy. Near threshold, the strong narrow resonances may spoil the accuracy, but for applications of rate coefficients in plasma diagnostics, these are smoothed out to a large extent in averaging the cross section over the electron energy distribution, and may contribute to the excitation rate only in the case of relatively cool plasmas.

8.2 Radiative transitions

A spectral line corresponds to the electromagnetic radiation of an ion which makes a transition from the excited state (j) to the lower one (i) with a given transition probability A_{ji}. I give here a brief description of several spectroscopic concepts and notations and refer for further details to various textbooks such as Herzberg (1944) and Condon & Shortley (1970).

8.2.1 Notations for energy levels and electron configurations. The
energy state of an atom or ion is specified by a set of quantum numbers, the most familiar set being described by the Russell-Saunders *LS coupling*, i.e.

$$n_1\ell_1^{q_1} n_2\ell_2^{q_2} \cdots n_m\ell_m^{q_m} \pi \left[{}^{2S+1}L_J\right] \equiv \gamma\pi \left[{}^{2S+1}L_J\right] \quad ,$$

where γ denotes the electron configuration, $\pi = (-1)^{\sum q_i\ell_i}$ is its "parity", and the symbol between square brackets denotes the energy level (see later). An electron (i) in the configuration γ is described by the *principal quantum number* n_i (characteristic for a *certain shell*), ℓ_i the quantum number of its orbital momentum. Furthermore, s_i denotes the quantum number of the electron spin $(= \pm\frac{1}{2})$ and j_i the resultant total angular momentum of l_i and s_i; $j = \ell \pm \frac{1}{2}(\ell \geq 1)$, $j = \frac{1}{2}(\ell = 0)$. All angular momenta are expressed in units of $h/2\pi$ (where h is the Planck constant). For $\ell = 0, 1, 2, 3, 4, 5, \cdots$ we speak of $s, p, d, f, g, h, \cdots$ electrons according to the <u>s</u>harp, <u>p</u>rincipal, <u>d</u>iffuse, and <u>f</u>undamental series in alkali spectra, and then alphabetically.

The building up of the electron configurations (and the associated periodic system of elements) is determined by *Pauli's exclusion principle* which states that in one atom no two identical electrons can occur, i.e., no two electrons can have the same set of quantum numbers [e.g., n, ℓ, j, and m_j (= component of j in a direction of preference)]. This principle prevents the filling of shells

---

[10] Compilations of excitation data have been reported by Aggarwal et al. (1986), Gallagher & Pradhan (1985), and Lang (1994), while Itikawa et al. (1984) and Itikawa (1991) have published comprehensive bibliographies.

with an arbitrary number of electrons. It follows that only a limited number of electrons can have the same n and ℓ (so-called *equivalent* electrons). With $\ell = -n + 1, \cdots, 0, \cdots, n - 1$, and $s = \pm\frac{1}{2}$ the building up occurs for the first three closed shells ($n = 1, 2, 3$) as: $1s^2 2s^2 2p^6 3s^2 3p^6 3d^{10}$ (cf. Herzberg 1944).[11] A *closed shell* gives no net contribution to the angular momentum: $\sum_i \boldsymbol{\ell}_i = \sum_i \mathbf{s}_i = \sum_i \mathbf{j}_i = 0, \sum_i \ell_i = \text{even}, \sum_i s_i = \text{an integer number}$. For example, we have $1s^2 2s^2 2p^6 3s^2 3p^2\ {}^3P_0$ for the configuration of the ground state of Fe XIII (for term notation see below).

An atomic energy *level* (or summed over all J called: *term*) is denoted by ${}^r(L\text{-symbol})_J$, where L and S are the total orbital and spin momenta and J is the total angular momentum (cf. Sect. 8.2.2). The notation for the levels (terms) is $S, P, D, F, G, H, \cdots$ for $L = 0, 1, 2, 3, 4, 5, \cdots$. For a given value of $L \geq S$ there are $r = 2S + 1$ levels that are distinguishable only by a different magnetic interaction of $\mathbf{L}$ and $\mathbf{S}$ and that have sometimes the same energy ("degenerate" levels). One speaks of a term with "*multiplicity*" $r = 2S + 1$. Also in the case $L < S$ where the actual multiplicity $= 2L + 1$ one still calls formally r the multiplicity (e.g., ${}^3P_{2,1,0}$ is a triplet term but also ${}^3S_1$ is called a triplet term). The notation for the multiplicity is for $S = 0, \frac{1}{2}, 1, 1\frac{1}{2}, 2, 2\frac{1}{2}, \cdots$: singlet, doublet, triplet, quartet, quintet, sextet, etc. terms. If the algebraic sum $\sum_i \ell_i$ is even or odd the term is called *even* or *odd* denoted by the index o ("odd"), e.g., even doublet term ${}^2D$ or odd triplet term ${}^3P^o$.

Since the vector $\mathbf{J}$ has $2J + 1$ orientations with respect to a certain direction of preference, e.g., given by a magnetic field, one calls $g_J = 2J + 1$ the *statistical weight* of the level with quantum number J. In the case of a magnetic field the component M_J (or m_j for a single electron) of $\mathbf{J}$ in the field direction, the so-called magnetic quantum number (Zeeman effect) can take the values: $M_J = J, J - 1, \cdots, 0, \cdots, -J + 1, -J$. For example, for $L = 2, S = 1, J = 2$ we have a ${}^3D_2$ level with statistical weight $g_2 = 5$.

8.2.2 Coupling schemes.

LS-coupling occurs when the individual electron orbital angular momenta $\boldsymbol{\ell}_i$ couple to a total orbital angular momentum $\mathbf{L} = \sum_i \boldsymbol{\ell}_i$, the electron spins s_i to a total spin angular momentum $\mathbf{S} = \sum_i \mathbf{s}_i$, while $\mathbf{L}$ and $\mathbf{S}$ combine with a smaller coupling to a resultant $\mathbf{J}$ (Herzberg 1944). Symbolically:

$$(\ell_1, \ell_2, ...)(s_1, s_2, ...) = (L, S) = J.$$

LS-coupling holds when the electrostatic interaction V_{el} between the electrons (which causes the distances between the multiplets) is much larger than the relativistic spin(S)-orbit(L) interaction V_{rel} (producing the multiplet splitting), i.e. $V_{\text{el}} \gg V_{\text{rel}}$; the multiplet splitting is small compared to the energy separation between levels from the same electron configuration but different L. LS-coupling holds for a large number of elements, at least at low nuclear

---

[11] The building-up order is according to increasing $n + \ell$ and at equal $n + \ell$ according to increasing n, i.e.: $1s2s2p3s3p4s3d4p5s4d5p6s4f5d6p \cdots$ ($4f$ is an inner orbit which is filled up much later for the rare earth elements in the periodic system).

Table 4. Parameters for radiative decay of $n = 2$ levels in He- and H-like ions

Seq.	i	Transition[1]	Type	α_i^2	β_i^2	$A_i(6)^3$	$A_i(12)^3$	$A_i(26)^3$
He	1	$2\,^1S_0 \to 1\,^1S_0$	$2E1$	$1.3\ 10^7$	6	$3.3\ 10^5$	$3.2\ 10^7$	$4.1\ 10^9$
	2	$2\,^1P_1 \to 1\,^1S_0(w)$	$E1$	$9\ 10^{12}$	4	$8.9\ 10^{11}$	$2.0\ 10^{13}$	$4.6\ 10^{14}$
	3	$2\,^3S_1 \to 1\,^1S_0(z)$	$M1$	$1.3\ 10^4$	10	50	$7.3\ 10^4$	$2.1\ 10^8$
	4	$2\,^3P_2 \to 1\,^1S_0(x)$	$M2$	$3\ 10^6$	8	$2.7\ 10^4$	$1.1\ 10^7$	$6.6\ 10^9$
	5	$2\,^3P_1 \to 1\,^1S_0(y)$	$E1$	$6\ 10^9$	9	$2.9\ 10^7$	$3.4\ 10^{10}$	$4.3\ 10^{13}$
	6	$2\,^1P_1 \to 2\,^1S_0$	$E1$	$4\ 10^7$	3	$1.8\ 10^7$	$4.9\ 10^7$	$5.0\ 10^8$
	7	$2\,^1P_1 \to 2\,^3S_1$	$E1$	$4\ 10^5$	7	$7.7\ 10^3$	$1.2\ 10^6$	$3.5\ 10^8$
	8	$2\,^3P_2 \to 2\,^3S_1$	$E1$	$1.2\ 10^8$	3	$5.9\ 10^7$	$1.5\ 10^8$	$1.5\ 10^9$
	9	$2\,^3P_1 \to 2\,^3S_1$	$E1$	$1.5\ 10^8$	1	$5.8\ 10^7$	$1.4\ 10^8$	$4.8\ 10^8$
	10	$2\,^3P_0 \to 2\,^3S_1$	$E1$	$1.5\ 10^8$	1	$5.8\ 10^7$	$1.3\ 10^8$	$3.8\ 10^8$
	11	$2\,^1S_0 \to 2\,^3S_1$	$M1$	0.13	7	0.0020	0.35	100
	12	$2\,^1S_0 \to 2\,^3P_1$	$E1$	350	3.5	<1	650	350
		$2\,^3S_1 \to 1\,^1S_0$	$2E1$	weak				
		$2\,^3P_2 \to 2\,^3S_1$	$M2$	weak				
		$2\,^3P_0 \to 1\,^1S_0$	$E1M1$	weak				
		$2\,^3P_0 \to 1\,^1S_0$	$E1^4$	weak				
H	13	$2\,^2P_{3/2} \to 1\,^2S_{1/2}(L\alpha_1)$	$E1$	$6.27\ 10^{12}$	4	$8.1\ 10^{11}$	$1.3\ 10^{13}$	$2.9\ 10^{14}$
	14	$2\,^2P_{1/2} \to 1\,^2S_{1/2}(L\alpha_2)$	$E1$	$6.27\ 10^{12}$	4	$8.1\ 10^{11}$	$1.3\ 10^{13}$	$2.9\ 10^{14}$
	15	$2\,^2S_{1/2} \to 1\,^2S_{1/2}$	$2E1$	$8.1\ 10^6$	6	$3.8\ 10^5$	$2.4\ 10^7$	$2.5\ 10^9$
	16	$2\,^2S_{1/2} \to 1\,^2S_{1/2}$	$M1$	$2.6\ 10^4$	10	$1.5\ 10^2$	$1.6\ 10^5$	$3.7\ 10^8$
		$2\,^2P_{3/2} \to 1\,^2P_{1/2}$	$E2$	weak				

[1] The resonance line (w), intercombination line (y) (blended by the line x), and the forbidden line (z) form the He-like triplet; $L\alpha 1, 2$ is the H-like resonance doublet line.
[2] Formula: $A_i \approx \alpha_i (Z/10)^{\beta_i}$ s^{-1} (He: $Z \gtrsim 10$, and for case $i = 12$ only for $Z = 20$; H: accurate for all Z).
[3] Accurate value of A_i (s^{-1}) for $Z = 6$, 12, and 26.
[4] Induced by hyperfine structure (HFS) mixing.

charge ($Z \lesssim 30$), but with increasing Z, $V_{\rm rel}$ increases more rapidly than $V_{\rm el}$ and the opposite situation occurs ($V_{\rm rel} \gg V_{\rm el}$): *jj-coupling*. In this case the individual ℓ_i and s_i combine to give a j_i, the total angular momentum of an individual electron. The j_i's combine with a smaller coupling to the total $\mathbf{J}$ of the atom or ion. Symbolically:

$$(\ell_1, s_1)(\ell_2, s_2)(\ell_3, s_3)... = (j_1, j_2, j_3 ...) = J.$$

This holds for larger Z especially in complicated level configurations with many levels close to each other. For highly excited levels (with large principal
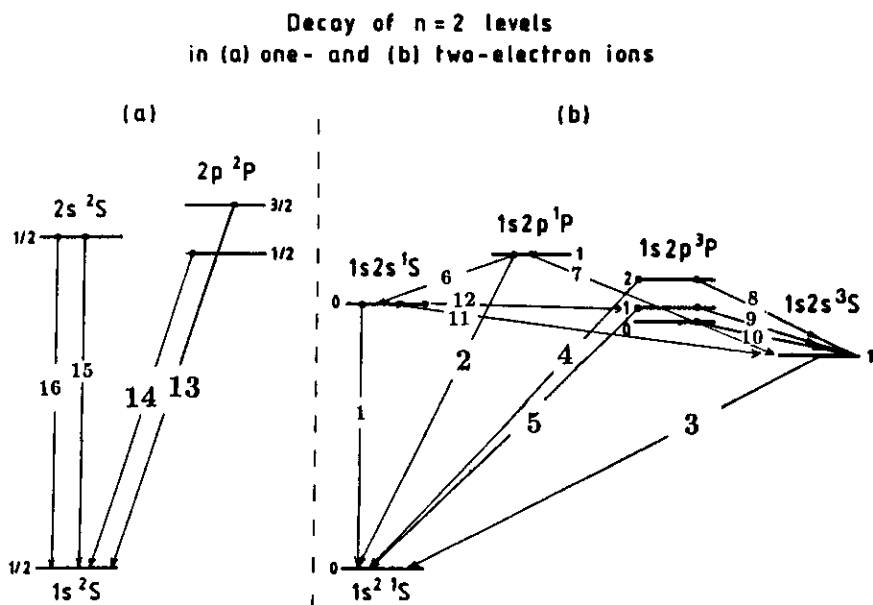
Fig. 13. Various radiative decay modes of the $n = 2$ levels in H-like ions (a) and in He-like ions (b). Lines 13 & 14 are the components of the H-like Lyman α resonance line; the well-known He-like triplet is formed by the resonance line (2), intercombination line (5) (blended by line 4), and forbidden line (3).

quantum number n) the electrostatic interaction decreases, hence jj-coupling occurs already at lower Z than for the lower levels (cf. Herzberg 1944).

An example of the transition from LS- to jj-coupling is provided by the $2\,^1P_1$ and $2\,^3P_{2,1,0}$ terms in He-like ions (cf. Fig. 13). For low Z ($Z \lesssim 30$) the three substates of $2\,^3P$ stay close (form an LS multiplet and are well below the $2\,^1P$ state, but for large Z the $2\,^3P_2$ state moves up close to the $2\,^1P_1$ state forming with this level by $(\frac{3}{2},\frac{1}{2})$ jj-coupling a J of 2 or 1, while the two $2\,^3P_{1,0}$ states still stay close and form by $(\frac{1}{2},\frac{1}{2})$ a J of 1 or 0. The two $^3P_1$ and $^3P_0$ levels cross each other several times as Z increases: between $Z = 7$–44, level 1 is above 0, outside this range on both sides the situation is reversed. Also the $2\,^1S_0$ level crosses the two ^3P levels several times (cf. Lin et al. 1977).

8.2.3 Types of transitions. Quantum selection rules characterize the type of transition that an atom or ion makes under the interaction with electromagnetic radiation. We distinguish the following radiative transitions (cf. Pal'chikov & Shevelko 1995): electric ($E\kappa$) and magnetic ($M\kappa$) 2κ-pole tran-

sitions. For example, we have $E1$ or $E2$ = electric dipole or quadrupole radiation, respectively, $M1$ or $M2$ = magnetic dipole or quadrupole radiation, etc., or more involved combinations such as two-photon electric dipole ($2E1$) or two-photon electro-magnetic ($E1M1$) radiation (e.g., Pal'chikov & Shevelko 1995, and references therein). Further, for isotopes with nuclear spin $I \neq 0$ and at high Z ($\gtrsim 30-40$) $E1$ radiation induced by hyperfine structure mixing (HFS) by the magnetic moment of the nucleus can occur (e.g., Dunford et al. 1990; Munger & Gould 1986). As an illustrative example I have shown in Fig. 13 and Table 4 all kinds of possible different radiative decay modes i of the $n = 2$ states in He-like and H-like ions.

8.2.4 Selection rules. We can distinguish between "exact" and "approximate" selection rules. The exact ones follow from the properties of the angular parts of the operators for electric and magnetic transitions and are independent of the coupling scheme. They are formulated for the "exact" quantum numbers, the total momentum J and its projection M_J, and the parity π (cf. Pal'chikov & Shevelko 1995):

$$\Delta J = 0, \pm 1, \pm 2, \cdots, \pm \kappa, \quad J + J' \geq \kappa \ , \tag{77}$$

$$\Delta M_J = 0, \pm 1, \pm 2, \cdots, \pm \kappa, \ , \tag{78}$$

$$\Delta \pi = (-1)^\kappa \ (\text{for } E\kappa), \text{ and } -(-1)^\kappa \ (\text{for } M\kappa) \ . \tag{79}$$

There is no restriction for the principal quantum number n. Finally, the rule of Laporte for a one-electron jump (more-electron jumps are less important) gives:

$$\Delta(\sum_i \ell_i) = \pm 1, \pm 3, \cdots \ , \tag{80}$$

that is even terms combine only with odd, and odd only with even. The approximate selection rules are dependent on the type of coupling scheme. We consider here LS-coupling for which one has, for electric E_κ transitions:

$$\Delta L = 0, \pm 1, \pm 2, \cdots, \pm \kappa \ \ (L + L' \geq \kappa), \Delta S = 0 \ , \tag{81}$$

and for magnetic M_κ transitions:

$$\Delta L = 0, \pm 1, \pm 2, \cdots, \pm(\kappa - 1) \ \ (L + L' \geq \kappa - 1) \ ,$$
$$\Delta S = 0, \pm 1, \pm 2, \cdots, \pm(\kappa - 1) \ \ (S + S' \geq \kappa - 1) \ . \tag{82}$$

For "allowed" electric dipole ($E1$) radiation which usually dominates the line emission one has thus: $\Delta L = 0, \pm 1$, $\Delta S = 0, \Delta J = 0, \pm 1, J = 0 \not\leftrightarrow J = 0$, $M_J = 0 \not\leftrightarrow M_J = 0$ (for $\Delta J = 0$), $\Delta \ell = \pm 1$, and $\pi' = -\pi$. Hence S-S transitions are ruled out.

For magnetic monopole ($M1$) radiation one has the same restrictions for L, S, and J as for E_1 and further: $\Delta \ell = 0$, and $\pi' = \pi$.

Finally, for electric quadrupole ($E2$) transitions: $\Delta L = 0, \pm 1, \pm 2$, $\Delta S = 0$, $\Delta J = 0, \pm 1, \pm 2$, $J = 0 \nleftrightarrow J = 0$, $J = \frac{1}{2} \nleftrightarrow J = \frac{1}{2}$, $J = 0 \nleftrightarrow J = 1$, $\Delta \ell = 0, \pm 2$, and $\pi' = \pi$. Here transitions between S terms and between S and P terms are ruled out.

For the most important electric dipole transitions $j \to i$ the transition probability A_{ji} is expressed as (e.g., Wiese et al. 1996):

$$A_{ji} = 6.6703 \; 10^{15} (w_i/w_j) f_{ij} \lambda^{-2} \qquad (83)$$

where A_{ji} is in units of s^{-1}, w_i and w_j are the statistical weights of the lower and upper level, respectively, f_{ij} is the absorption oscillator strength and λ the wavelength in Å. The general systematic trends in the behaviour of A for the allowed transitions is as follows. For transitions where a change in the principal quantum number n occurs the oscillator strength is nearly comstant and $\lambda \propto Z^{-2}$ so that A approximately scales $\propto Z^4$. For $\Delta n = 0$ transitions approximately $f \propto 1/Z$ and $\lambda \propto 1/Z$, hence approximately $A \propto Z$.

If for a transition one of the above-mentioned selection rules is violated it is called "forbidden". A violation of the selection rules is connected with magnetic interactions (mostly spin-orbital ones) and the forbidden lines can arise from any of the higher multipoles or by a multi-photon mode.

Allowed electric dipole transitions are in most cases the dominant ones and other types of transitions are usually orders of magnitude weaker. As a rule of thumb Herzberg (1944) gives intensity ratios typically $E1 : M1 : E2 \sim 1 : 10^{-5} : 10^{-8}$, and Summers (1988) gives: $\sim 5 \; 10^7 \; Z^4 : 3 \; 10^3 Z^6 : 3 \; Z^6$. However, the actual situation is more complicated. For hot plasmas non-electric-dipole transitions can play an important role (e.g., in the density diagnostics, see Sect. 13) because the probabilities of forbidden transitions rapidly increase with increasing Z with powers between ~ 6–10. To give an idea of the relative importance and behaviour of various types of radiation, I have given in Table 4 some typical values for the transition probabilities for all kinds of possible radiative decay modes i of the $n = 2$ states in He-like and H-like ions (cf. also Fig. 13 in which weak transitions are not indicated but mentioned in Table 4 except for the very weak electric quadrupole $E2$ transition $2^2P_{3/2} \to 2^2P_{1/2}$ in H-like ions). The A values are mainly based on data given by Lin et al. (1977) and Wiese et al. (1996). Table 4 gives also the parameters for an approximation of the transition probability A_i of transition i which is generally coarse for the He-like case and accurate for the H-like case, and the accurate values of A_i for $Z = 6, 12$, and 26.

9   Continuum Radiation

In astrophysics there are essentially three physical processes that produce a continuum spectrum in X rays: bremsstrahlung ("braking radiation"), synchrotron radiation, and Compton scattering. These processes are discussed in detail in the Chapters by Longair and Liedahl; here I briefly consider the first

process (plus free-bound and two-photon emission) because this is important for an optically thin plasma.

Bremsstrahlung is radiation due to the acceleration of a charged particle in the Coulomb field of another charge and is sometimes also referred to as *free-free emission* (ff) because it originates from a transition of the impacting particle between two "free" or unbound states of the target ion. If the two charges are identical, there is no net acceleration of the electric dipole moment during this binary encounter, so electron-electron and ion-ion free-free radiation power will vanish in the electric-dipole limit and can usually be neglected. Electron-ion collisions that produce a much larger electron acceleration are mainly responsible for the bremsstrahlung in a hot cosmic plasma.

An exact treatment of this process requires a quantum mechanical calculation but it turns out that a classical treatment gives already the correct functional dependence for most of the physical parameters (cf. the Chapter by Longair). The quantum correction on the classical result is then introduced as the socalled *Gaunt factor*, which in a large interesting parameter range is of order unity. In the coronal model we consider only *thermal* bremsstrahlung for a Maxwellian electron velocity distribution, characterized by some temperature T. Integrating over the Maxwell distribution one obtains for the thermal free-free continuum emissivity (power per unit volume per unit frequency range) (cf. Rybicki & Lightman 1979):

$$P_{\text{ff}}(\nu, T) = C_{\text{ff}} Z_i^2 \, n_e n_i \, \bar{g}_{\text{ff},i}(\nu, T) \, T^{-1/2} e^{-h\nu/kT} \quad , \tag{84}$$

where $\bar{g}_{\text{ff},i}$ is the velocity-averaged Gaunt factor for the given target ion (i), Z_i and n_i are the effective charge and density of the target ion, n_e the electron density, and the factor C_{ff} worked out numerically in c.g.s. units (also T in K, densities in cm^{-3}):

$$C_{\text{ff}} = \frac{2^5 \pi e^6}{3 m_e c^3} \left(\frac{2\pi}{3 k m_e} \right)^{1/2} = 6.842 \times 10^{-38} \text{ erg cm}^{-3} \text{ s}^{-1} \text{Hz}^{-1} \quad , \tag{85}$$

where e and m_e are the electron charge and mass, and k the Boltzmann constant. Because the Gaunt factor only slowly varies the ff radiation has a rather flat spectrum with a sharp exponential cut-off near $h\nu \approx kT$ which provides a straightforward measurement of the temperature from the spectral shape near the cut-off when the bremsstrahlung is the dominant process creating the continuum. The frequency-integrated ff emission (in erg cm^{-3} s^{-1}) is given by:

$$P_{\text{ff}}^{\text{tot}}(T) = 1.426 \times 10^{-27} Z_i^2 \, n_e n_i \, \bar{g}_{\text{ff}}(T) \, T^{1/2} \quad , \tag{86}$$

where $\bar{g}_{\text{ff}}(T)$ is the frequency-average of $\bar{g}_{\text{ff},i}$, which is in the range 1.1–1.5 and can be approximated within about 20% by 1.2 (cf. Rybicki & Lightman 1979).

To calculate the total amount of ff radiation one must sum over all ions (i) present in the plasma. For a plasma with cosmic abundances the main contributions come from hydrogen and helium but other species cannot always be neglected. Gronenschild & Mewe (1978) and Mewe et al. (1986) have introduced a total averaged Gaunt factor G_{ff} by replacing Eq. (84) by

$$P_{ff}(\nu, T) = C_{ff} Z_i^2 \, n_e^2 \, G_{ff} \, T^{-1/2} e^{-h\nu/kT} \quad , \tag{87}$$

where,

$$G_{ff}(\nu, T) = \sum_i \left(\frac{n_i}{n_e}\right) \bar{g}_{ff,i}(\nu, T) Z_i^2 \quad , \tag{88}$$

and the effective charge of ion (i) is defined by

$$Z_i = \left(\frac{n_{i-1,0}^2 E_{i-1}}{E_H}\right)^{1/2} \quad , \tag{89}$$

where E_{i-1} is the ionization energy from the ground state with principal quantum number $n_{0,i-1}$ in the *recombined* ion (i-1) and E_H the ionization energy of hydrogen.

The Gaunt factors have been calculated as a function of ν, T, and Z_i by Karzas & Latter (1961) who presented their results only graphically but since then, Carson (1988) has presented extensive tables reproducing the results of Karzas & Latter. Gronenschild & Mewe (1978) and Mewe et al. (1986) have derived approximation formulae for the free-free Gaunt factors given by Karzas & Latter (1961), based upon the high-energy Born approximation and a correction factor (accuracy better than 15%). Kaastra (1992) has later improved these calculations by interpolating Carson's table. Moreover he has introduced a relativistic correction factor based on the relativistic calculations in the Born limit by Kylafis & Lamb (1982).

In addition to free-free radiation, continuum emission in optically thin plasmas is also produced by the interaction of a free electron with an ion by a *free-bound* (fb) transition or a *two-photon* process (2γ). Free-bound emission occurs when a free electron with kinetic energy E_{el} is captured into a bound state (m) with ionization energy E_m of the ion (radiative recombination). The energy of the emitted photon is $h\nu = E_{el} + E_m$. This process is often important and dominates the continuum radiation in a CIE plasma with temperature $T \ll 1$ MK, whereas for $T \gg 10$ MK free-free radiation is dominant. At $T \sim 1$ (or 10) MK free-bound radiation is dominant for photon energy $h\nu \gtrsim 0.1$ (or 3) keV. In a photo-ionized plasma free-bound emission is even more dominant because recombination is here much more important (see the Chapter by Liedahl). For relatively hot plasmas (e.g., $T \gtrsim$ a few MK) dielectronic recombination may also give a contribution to the continuum radiation but this process was not considered.

Two-photon emission can be important for H- and He-like ions and it occurs when the metastable $2s$ level ($2\,^2S_{1/2}$ for H, $2\,^1S_0$ for He) is excited. From the selection rules (cf. Sect. 8.2.4) it follows that the $2s$ electron cannot decay by a single-photon transition. At high electron density the metastable $2s$ level will be depopulated by collisions with electrons or protons (induced transition $2s \rightarrow 2p$) but if the density is sufficiently low ($n_e \lesssim n_c$) the metastable level can decay by the simultaneous emission of two photons ($2E1$, cf. Table 4) which have together a total energy equal to the excitation energy E_0 of the metastable S level. The spectrum is symmetric around $E = \frac{1}{2}E_0$ and extends from $E = 0$ to $E = E_0$ [see Spitzer & Greenstein (1951) for H-like ions and Dalgarno & Drake (1969) for He-like ions]. Mewe et al. (1986) derive for the critical density $n_c \approx 7\ 10^3 Z^{9.5}$ (H) or $2\ 10^5(Z-1)^{9.5}$, e.g., a few times 10^{11} cm^{-3} for carbon. Thus for many astrophysical applications collisional depopulation will be unimportant.

For a comparison of the various contributions of ff, fb, and 2γ processes to the total continuum emission I refer to the figures given by Mewe et al. (1986). The fb and 2γ processes were incorporated by Gronenschild & Mewe (1978) and Mewe et al. (1986) in their calculations as a total continuum Gaunt factor G_c given by

$$G_c = G_{\text{ff}} + G_{\text{fb}} + G_{2\gamma}. \qquad (90)$$

For the fb calculations the above-mentioned authors have used a constant approximation for the fb Gaunt factor given by Karzas & Latter (1961), and used a hydrogenic approximation for recombinations to excited levels (cf. Sect. 7.1). Later Kaastra (1992) has taken into account the correct energy dependence of the Gaunt factor and improved the calculations for the recombinations to the ground state by using the photo-ionization cross sections given by Verner et al. (1993) in applying the Milne relation (Eq. 34). Kaastra (1992) has also improved Mewe's approximation for the 2-photon Gaunt factor by applying a more accurate interpolation of the results of Spitzer & Greenstein (1951) and Dalgarno & Drake (1969). All these improvements were implemented in our code SPEX (cf. Sect. 3.2).

Finally, I give here a few alternative expressions for the total continuum emissivity $P_c(\lambda, T)$ written as the energy emissivity at wavelength λ per unit wavelength interval in units of erg cm^{-3} s^{-1}Å^{-1}:

$$P_c(\lambda, T) = 2.461\ 10^{-22}\ n_e N_H\, G_c\, \lambda^{-2} T^{-1/2} \exp[-143.88/(\lambda T)]\ , \qquad (91)$$

or, alternatively, as the photon number emissivity $P_c(E, T)$ at photon energy E per unit energy interval in units of phot cm^{-3} s^{-1} keV^{-1}:

$$P_c(E, T) = 3.637\ 10^{-15}\ n_e N_H\, G_c\, E^{-1} T^{-1/2} \exp[-E/kT]\ , \qquad (92)$$

where in Eq. (91) T is in MK, λ in Å, and in Eq. (92) E and kT are in keV and where the ratio n_e/N_H is taken equal to 1.2 for a plasma with cosmic

abundances (Anders & Grevesse 1989). For an easy estimate we can make use of the following Gaunt factor approximation (λ in Å, T in MK) (Mewe et al. 1985a):

$$G_c \simeq 27.83(T + 0.65)^{-1.33} + 0.15\lambda^{0.34}T^{0.422} \; , \tag{93}$$

which gives a reasonable approximation (within $\sim$10–20%) at $T \geq 3$ MK and a crude estimate ($\sim$30–50%) for 0.2 MK $\leq T < 3$ MK for a plasma with cosmic abundances from Allen (1973). However, for wavelengths below the O VIII edge at 16.8 Å, better results can be obtained by properly taking into account the contributions from fb and 2γ emission.

IV. Diagnostics of Plasma Parameters

High-resolution spectroscopy permits the diagnostics of a variety of plasma parameters such as coronal temperature, ionization balance, emission measure, abundances, densities, and velocities (Mewe 1991; for many references, see Keenan 1992, 1995).

10   Electron Temperature

The soft X-ray spectrum depends sensitively on the ionization structure throughout the temperature range 0.1–100 MK. The mere detection of a particular spectral line in the spectrum implies the existence of plasma near the temperature of maximum formation (see Sect. 8) for that line, hence provides an accurate "thermometer" for the source emission region.

The electron temperature T can be diagnosed from the intensity ratio of two collisionally excited lines from different ions of the same element using Eq. (53). Though this line ratio is independent of the elemental abundance, it does depend on the ionization equilibrium. In situations in which deviations from ionization equilibrium occur, one can avoid this constraint by using the ratio of two lines from the same ionization stage, but with a different temperature dependence, e.g., two collisionally excited lines with different excitation energies such as the Lyman α and β lines. Alternatively, one can measure the ratio of lines at nearly the same wavelength for which the excitation functions have a different dependence on T, e.g., in the helium-like $2 \rightarrow 1$ triplet. This consists of a resonance (r) $2^1P \rightarrow 1^1S$ line, a forbidden (f) $2^3S \rightarrow 1^1S$ line and an intercombination (i) $2^3P \rightarrow 1^1S$ line (summed over two close components). The intensity ratio $r/(i + f)$ varies with electron temperature.

Another possibility is to use the intensity ratio of the collisionally excited resonance line and a nearby dielectronic recombination satellite line

(see Sect. 15). The helium-like triplets with their satellites provide a very valuable diagnostics for electron temperature, emission measure, abundances, and ionization balance.

11   Elemental Abundances

In both coronal equilibrium and non-equilibrium situations, ions of different elements which have similar ionization potentials usually coexist in close proximity. Thus the ratios of the prominent emission lines from ions of different elements yield in a relatively model-independent way elemental abundances. By using a suitable set of lines from different ionization stages of one given element, e.g., iron, we can determine the temperature distribution by fitting the line intensities. Then by selecting suitable lines from different elements, relative elemental abundances can be determined. For a given line the emissivity $P_\ell \propto n_e N_H A_Z$ (Sect. 8) and the continuum emissivity $P_c \propto n_e N_H G_c$ (Sect. 9). Here the effective Gaunt factor G_c is a complicated function of the element abundances (cf. Gronenschild & Mewe 1978; Mewe et al. 1986), but for relatively hot ($\gtrsim 5$ MK) plasmas it is mainly determined by contributions from H and He. Then the line-to-continuum ratio P_ℓ/P_c is approximately proportional to the element abundance so that from the intensity ratio of a line to the neighbouring unblended continuum, in principle, the absolute abundance with respect to H can be derived.

12   Ionization Balance in NEI

In a transient plasma the line spectrum is sensitive to the deviations from the ionization equilibrium, whereas the bremsstrahlung continuum immediately follows the changing plasma conditions (temperature), so that the line/continuum ratio can provide an indication of the deviation from the ionization equilibrium (e.g., Shapiro & Moore 1977). To study such effects in solar or stellar flares, high-resolution spectroscopy must be applied (e.g., Mewe et al. 1985b). Also resonance/inner-shell excitation satelline ratios can be used for this purpose (cf. Sect. 15.4.2).

13   Electron Density

From spectral fits to the line and/or continuum emission one can determine the emission measure $\int n_e^2 dV$ (cf. Sect. 14), but this alone is not sufficient to model the optically thin source. One needs to know the electron density, n_e from density-sensitive lines to determine the size of the emitting volume V which is a critical parameter in any theoretical modeling of plasma heating and formation.

Electron densities can be measured using density sensitive spectral lines originating from metastable levels or using inner-shell excitation satellites to resonance lines (for reviews, e.g., Feldman 1981; Mason & Monsignori Fossi 1994; Mewe et al. 1991; Masai 1994b). In the first case the helium-like $2 \rightarrow 1$ triplet system lines (cf. Sect. 10) are particularly important (Gabriel & Jordan 1972; Pradhan 1985; Mewe et al. 1985a). The helium-like intensity ratio f/i varies with electron density above a certain critical density n_{ec} due to the collisional coupling between the *metastable* 2^3S upper level of the forbidden line f and the 2^3P upper level of the intercombination line. It does not strongly depend on the model (CIE or XPN) because its density dependence is determined only by the collisional coupling between the two upper line levels (see below), but the singlet/triplet ratio $r/(i+f)$ (which can be used for temperature diagnostics) does and can also serve as an indication of the validity of the coronal model (see Mewe 1990). The f/i line intensity ratio of helium-like ions from carbon through magnesium in the wavelength region 9–42 Å can be used to diagnose coronal plasmas in the density range $n_e = 10^8$–10^{13} cm^{-3} and corresponding temperature range $T \sim 1$–6 MK.

However, for density diagnostics in active late-type stars one must observe lines formed at temperatures around $T \sim 10$ MK. For this purpose Mewe et al. (1985a, 1991) have considered many density-sensitive lines in the Fe L-shell complex, i.e. 2ℓ–$\geq 3\ell'$ transitions from ions Fe XVII–XXIV (and some corresponding nickel lines from Ni XXI–XXIV) covering the wavelength region 7–13 Å, lines between 90–140 Å from 2ℓ–$2\ell'$ transitions in Fe XVIII–XXIII, and lines between 170–275 Å from 3ℓ–$3\ell'$ transitions in Fe IX–XIV ions. The density dependence arises because the upper line level can be excited from various sub-levels within the ground state which become collisionally coupled at increasing densities (the same holds for the satellite lines). The Fe and Ni lines can be used as tools for diagnosing plasmas in the density range 10^{10}–10^{15} cm^{-3} and temperature range ~ 0.5–15 MK. A selection of density-sensitive lines is given by Mewe et al. (1991).

The forbidden/intercombination line ratio in He-like ions

For the special case of the helium-like forbidden f ($m \rightarrow g$) and intercombination i ($k \rightarrow g$) lines I illustrate the steady-state solution of Eq. (51) for the upper-level populations of these lines, using a simplified 3-level term scheme with levels 1^1S (denoted by g, the ground level), 2^3S (m, the "forbidden" level), and 2^3P (k, the "intercombination" level). Taking into account only the most important atomic processes and neglecting for the moment all recombination processes, the population densities are given by solving the following two coupled equations:

$$N_m(A_{mg} + n_e S_{mk}) = n_e N_g S_{gm} + N_k A_{km},$$
$$N_k(A_{kg} + A_{km}) = n_e N_g S_{gk} + n_e N_m S_{mk} . \qquad (94)$$

Assuming first a very low population for level k, i.e. $N_k \ll N_g$, hence neglecting in the r.h.s. of the first equation of Eq. (94) the last term, then we

obtain for the ratio R of the forbidden and intercombination line intensities $P_f = N_m A_{mg}$ and $P_i = N_k A_{kg}$:

$$R \equiv \frac{P_f}{P_i} = \frac{S_{gm}(T)}{S_{gk}(T)} \frac{1 + (A_{km}/A_{kg})}{1 + (n_e/n_{ec})} \quad , \tag{95}$$

where

$$n_{ec} = \frac{A_{mg}}{S_{mk}} \frac{S'_{gk}}{S_{gk} + S_{gm}} \quad , \tag{96}$$

is the *critical density* n_{ec} above which collisional excitation 2^3S to 2^3P begins to dominate the radiative decay from the metastable 2^3S level to the ground state. If $n_e S_{mk} \ll A_{mg}$ then R does not depend on n_e, but when $n_e \gtrsim n_{ec}$ then R becomes sensitive to variations in n_e. As $A_{mg} \sim Z^{10}$ (cf. Table 4) and $S_{mk} \sim Z^{-3}$, n_{ec} scales as Z^{13}, i.e. $n_{ec} \approx 0.3(T/T_m)^{0.3} Z^{13}$ cm^{-3}, where T_m is the temperature of maximum line formation (cf. Mewe & Schrijver 1978a; Mewe et al. 1991). The ratio $S_{gm}(T)/S_{gk}(T)$ in Eq. (95) introduces a temperature dependence of R which is, however, rather weak because the difference $E_k - E_m$ in excitation energies is small. Though Eq. (95) gives the essential behaviour of R, the solution is actually more complicated because the effect of the last term in the first equation of Eq. (94) cannot be neglected completely. The full solution of Eq. (94) reads (cf. Mewe & Gronenschild 1981):

$$R = \frac{[S_{gm} + (1 - BR_i)S_{gk}]BR_f}{S_{gk}BR_i + [S_{gm} + (1 - BR_i)S_{gm}](1 - BR_f)} \quad , \tag{97}$$

where the collision rates S_{gm} and S_{gk} include the effects of cascades, and S_{gk} also contains a contribution from proton excitation (cf. Mewe & Schrijver 1978a,c and also Sect. 8.1), and where

$$BR_f = \frac{A_{mg}}{A_{mg} + n_e S_{mk} BR_i}, \text{ and } BR_i = \frac{A_{kg}}{A_{kg} + A_{km}} \tag{98}$$

are the branching ratios of the forbidden and intercombination line, respectively. Eq. (97) would reduce to Eq. (95) only if $BR_f \simeq 1$ and $BR_i \simeq 1$ which is obviously not the case, but the density behaviour of R is similar.

We have neglected here recombination processes which are usually less important in collision-dominated (CIE) plasmas but are just dominant in X-ray photo-ionized (XPN) plasmas. If we make the substitutions $S_{gm} \rightarrow (N_i/N_g)\alpha_{cm}$ and $S_{gk} \rightarrow (N_i/N_g)\alpha_{ck}$ (where N_i is the density of the next higher H-like ion and α_{cm} and α_{ck} are the recombination rate coefficients to the levels m and k) we obtain the general case. Since it turns out that the ratios S_{gm}/S_{gk} and α_{cm}/α_{ck} are quite similar (e.g., Mewe & Schrijver 1978a) the critical density has the same behaviour in dependence of Z and is approximately the same (within about 20–40%) for the CIE and XPN case (see also the Chapter by Liedahl).

The magnitude of A_{mg} (i.e. the type of transition) determines the density range over which R is n_e–sensitive. Keenan (1992) distinguishes the following three types of transitions:

- Intercombination transitions in low-Z species (e.g., $2s2p\ ^3P_1 \rightarrow 2s^2\ ^1S$ in O V) or forbidden transitions in high-Z species (e.g., $2s^22p^2\ ^3P_1 \rightarrow 2s^22p^2\ ^3P_0$ in Ca XV) have $A_{mg} \simeq 10^2 - 10^4\ s^{-1} \Rightarrow n_e$ range $\simeq 10^8 - 10^{13}\ cm^{-3}$ (applicable, for example, to the solar transition region/corona and late-type stellar atmospheres).
- Forbidden transitions in low-Z species (e.g., $3s3p\ ^3P_2 \rightarrow 3s^2\ ^1S$ in Si III) have $A_{mg} \simeq 10^{-3} - 1\ s^{-1} \Rightarrow n_e$ range $\simeq 10^2 - 10^7\ cm^{-3}$ (applicable to gaseous nebulae such as H II regions and planetary nebulae).
- Forbidden transitions within the ground term of low-Z species (e.g., $2s^22p\ ^2P_{3/2} \rightarrow 2s^22p\ ^2P_{1/2}$ in C II) have $A_{mg} \simeq 10^{-6} - 10^{-3}\ s^{-1} \Rightarrow n_e$ range $\leq 100\ cm^{-3}$ (applicable to the interstellar medium and supernova remnants).

14   Differential Emission Measure

From Eq. (53) we find for the line power P integrated over the whole emitting source volume V (cm^3)

$$P \propto EM f(T)\ , \tag{99}$$

where $f(T)$ is the emission function that contains contributions from electron impact excitation, ion balance, and abundances, and

$$EM = \int n_e N_H\,dV \tag{100}$$

is the total *emission measure* of the source (in units cm^{-3}). In this case the ratio of two lines from the same element but with different temperature dependence gives T and EM, while the ratio of two lines with the same temperature dependence but from different elements gives the abundance ratio. The line/continuum ratio gives the absolute abundance.

However, in general the situation is more complicated. It is to be expected that the source is not well represented by one single temperature, but that instead plasma at *many different temperatures* will contribute to the X-ray spectrum. Then we write

$$P \propto \int f(T)D(T)\,d\log T\ , \tag{101}$$

where we introduce the *differential emission measure* (DEM) distribution function $D(T)$ defined by

$$D(T) = n_e(T)N_H(T)\frac{dV}{d\log T}\ . \tag{102}$$

This is the weighting function that measures how strongly any particular temperature contributes to the observed spectrum.

To derive physical parameters from the spectra various techniques can be applied such as multi-temperature fitting or fitting with continuous models to derive $D(T)$ (for references e.g., Kaastra, Mewe, Liedahl et al. 1996; Mewe et al. 1995b, 1996; see also the Chapter by Kaastra). These methods use a pre-calculated set of model spectra $f(\lambda_i, T_j)$. Here $f(\lambda_i, T_j)$ denotes the plasma line plus continuum emission function (phot cm^3 s^{-1}) per unit $n_e N_H$, per wavelength bin λ_i, and for an electron temperature grid T_j. These model spectra are folded through the instrument response, include interstellar absorption and take into account the appropriate abundances. The total spectrum integrated over the temperature distribution is written as

$$F(\lambda_i) = \int f(\lambda_i, T) n_e(T) N_H(T) \, dV(T) \simeq$$
$$\sum_{j=1}^{M} f(\lambda_i, T_j) D(T_j) \Delta \log(T_j) \ . \tag{103}$$

The DEM distribution is derived by matching the observed line and continuum (wavelength) spectrum $\tilde{F}(\lambda_i)$ as well as possible to the synthesized model spectrum $F(\lambda_i)$ for a grid of temperatures ranging from T_1 up to T_M and with a step size of typically $\Delta \log(T_j) = 0.1$ (sufficiently small since most lines are formed within $\delta \log T \simeq 0.3$). It is important to include also the continuum spectrum in the analysis since the line–to–continuum ratio contains important information on the abundances (in particular the [Fe/H] abundance ratio) and line scattering effects. I note that the determination of $D(T)$ by the inversion of Eq. (103) is not trivial since in practice the measured spectrum contains noise and a unique solution is never possible (see the Chapter by Kaastra for a discussion). In the analysis with SPEX (cf. Sect. 3.2) five DEM methods can be applied:

- (i) multi–temperature Gauss fitting,
- (ii) regularization method,
- (iii) polynomial method,
- (iv) clean algorithm,
- (v) genetic algorithm.

The first, fourth, and fifth method are especially suited to resolve discrete narrow temperature structures, whereas the second and third method are more suited for smooth temperature distributions (cf. Kaastra et al. 1996; Mewe et al. 1996). A nice example of a comparison between all DEM methods, as applied to the analysis of combined *ASCA* and *EUVE* data of the active solar-type star EK Draconis, is given in the paper by Güdel et al. (1997; their Fig. 4).

15   Diagnostics of Satellite Lines

Satellite lines are systems of lines appearing close to or blended with the resonance lines of highly ionized atoms formed in hot astrophysical and laboratory plasmas. For H- and He-like ions these types of lines have been well known for almost 60 years. Edlén & Tyrén (1939) discovered such lines in the spectra from a vacuum spark and interpreted them as resonance transitions in the presence of an additional bound perturbing ("spectator") electron $n\ell$, for example, the $1s^2n\ell$–$1s2pn\ell$ Li-like satellites to the He-like resonance line $1s^2$–$1s2p$. These lines correspond to the stabilizing transitions in the process of *dielectronic recombination*, which was first recognized by Massey & Bates (1942) as a *two-step* recombination process. The *first* step, radiationless (or "dielectronic") capture of a free electron by a recombining ion, gives rise to a doubly excited autoionizing quasi-bound state. The *second* step (stabilization) is the emission of radiation (*satellite* line) to give a stable, singly excited state in the recombined ion.

The stronger satellites arise from states with $n = 2$ for the perturbing spectator electron and appear on the long-wavelength side of the parent resonance line. The group of $n = 3$ satellites appears closer with some members on the short-wavelength side and/or blended with the resonance line, while those arising from $n \geq 4$ are practically indistinguishable from it.

The *dielectronic recombination* (DR) process has been studied in detail since Burgess (1964, 1965) was able to show that it can provide an important additional recombination mechanism in hot dilute plasmas like those observed in the solar corona, affecting noticeably the ionization equilibrium, and thus the interpretation of the ionization temperature of the corona. Most applications of DR were therefore first concentrated on this particular aspect.

Since the early seventies with the advent of many observations of high-resolution X-ray spectra from hot astrophysical and laboratory plasmas, its importance as a line formation mechanism has been emphasized. In particular, Gabriel (1972) and co-workers have demonstrated that satellite lines provide very powerful tools to diagnose such hot plasmas since these lines are sensitive to variations of *electron temperature* and *density*, and *deviations* from a *Maxwellian electron distribution*. Moreover, in transient ionizing plasmas and for heavier ions, these lines can also be produced by direct electron impact excitation of a ground-state *inner-shell* electron, which also allows the *(transient) ionization state* of the plasma to be determined. These authors made the first attempt to interpret the satellite intensities and have developed a detailed theory of the He-like ion satellites (for a review see Dubau & Volonté 1980). For references to the numerous observations of satellite lines in high-resolution spectra of hot astrophysical plasmas (essentially the solar corona) and laboratory sources, see Mewe (1988). Note that Mewe & Kaastra have recently written several internal SRON notes on data compilations for K-shell X-ray spectra of ions with $Z = 6$–28 which are available on request.
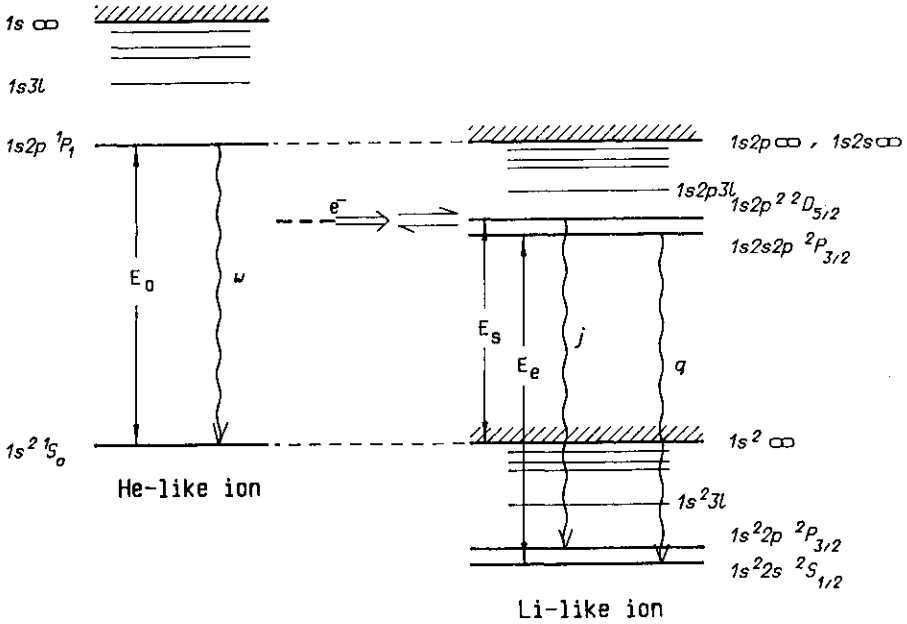
Fig. 14. Energy level diagram showing the parent resonance line w in the He–like ion together with the strong DR satellite j and the IE satellite q in the Li–like ion (from Mewe 1988).

15.1   Dielectronic recombination (DR) satellite intensity

The contribution from DR is derived as follows. In the usual way the emission rate I_{sk}^{DR} (photons cm^{-3} s^{-1}) by dielectronic excitation of the satellite line $s \to k$ is given by

$$I_{sk}^{\mathrm{DR}} = N_{z,s} A_{sk}^r \ , \tag{104}$$

where the population density $N_{z,s}$ (cm^{-3}) of state s is determined by the balance between dielectronic capture (rate coefficient C_s^{d}) and autoionization plus radiative decay, i.e.,

$$N_{z+1,1}\, n_{\mathrm{e}}\, C_s^{\mathrm{d}} = N_{z,s}\, A_s(\mathrm{tot}) \ , \tag{105}$$

where n_{e} is the electron density, and $A_s(\mathrm{tot}) = A_s^{\mathrm{a}} + \sum A_s^{\mathrm{r}}$, the total decay rate of satellite level s by autoionization and by radiative decay. Thus:

$$I_{sk}^{\mathrm{DR}} = N_{z+1,1} n_{\mathrm{e}} C_s^{\mathrm{d}} B R_s \ , \tag{106}$$

with C_s^{d} given by Eq. (45) and the branching ratio BR_s given by Eq. (47), so that we obtain for the DR line intensity (photons cm^{-3} s^{-1}):

$$I_{sk}^{\mathrm{DR}} = 2.071 \times 10^{-16}\ N_{z+1} n_{\mathrm{e}} T_{[\mathrm{K}]}^{-3/2}\ B_s\ \exp(-E_s/kT) \ , \tag{107}$$

where the satellite intensity factor B_s is given by Eq. (49).

15.1.1 Density effects. Up to now we have considered the special case of a low-density plasma in which all ions $Z^{+(z+1)}$ and Z^{+z} are in their ground states. At increasing electron density (say $n_e \gtrsim 10^{13}$ cm^{-3}) the excited levels $p > 1$ in the ground-state configuration of ion $Z^{+(z+1)}$ (cf. Fig. 8) will start to become populated significantly, so as to give sometimes also contributions to the DR satellites. The total contribution of all levels p to the emission rate $s \to k$ is then given by a summation over all p (e.g., Lemen et al. 1986). The *density dependence* of the satellite emission then arises through the density-dependent populations in the fine-structure levels of the ground configuration of ion $Z^{+(z+1)}$.

15.2   Inner-shell excitation (IE)

Sometimes there is a contribution to the satellite intensity from electron *impact excitation* of an inner-shell electron in the recombined ion Z^{+z} from the *ground* state (because we assume the conditions for the low-density case) from which the satellite upper line level s has an excitation energy E_e. This process can become efficient in atomic systems containing many electrons in the inner shell or for satellite lines arising from non-autoionizing states. It is not effective in He-like ions since there it requires simultaneous excitation of two electrons which is much less probable than single-electron excitation. In *transient* plasmas (cf. Sect. 4.1.3) this process can be very important (cf. Mewe & Schrijver 1980).

For the photon emission rate by *inner-shell excitation* (photons cm^{-3} s^{-1}) of the satellite line $s \to k$ we write

$$I_{sk}^{IE} = N_z n_e B R_s S_e \ , \tag{108}$$

where N_z is the density of ion Z^{+z} in the ground state, $B R_s$ is the branching ratio given by Eq. (47) and S_e is the electron impact excitation rate coefficient given by the formulae of Sect. 8.1.1.

This process is most effective under circumstances where simultaneously a *high temperature* [needed to overcome the excitation energy, e.g., E_e in Eq. (111)] and a *low ion stage* [e.g. Li-like in Eq. (111)] occur. Because the (Li-like) ionization potential is much lower than the excitation energy of the satellite (cf. Fig. 14) this is possible only in a *transient* plasma in which the ionization lags behind (see Sect. 4.1.3).

15.2.1 Density effects. At higher electron densities, also other (excited) levels in the ground configuration of ion Z^{+z} can obtain a significant population, thus introducing a *density dependence* in the IE part of the satellite line, similarly as in the DR case (cf. Lemen et al. 1986).

15.3 Inner-shell ionization (II)

Mewe & Gronenschild (1981) and Mewe et al. (1980) have considered electron impact ionization from the inner $1s^2$ shell of ion $Z^{(z-1)}$ which contributes to the production in an optically thin plasma to the formation of a certain line in the next higher ion Z^{+z} (e.g., the satellites to He-like resonance lines from lower Li-, Be-, etc. like ions).

For the same reason as given for IE the II process is especially important in a transient plasma.

It turns out that for inner-shell ionization of Li-like ions the ionization formula of Lotz (1968) (corrected by the *fluorescence yield* C_{II}) agrees within 5% with the calculations of Sampson & Zhang (1988). For the photon emission rate we write analogously to Eq. (108)

$$I_{sk}^{II} = N_{z-1} n_e C_{II} S_i \ , \tag{109}$$

where the rate coefficient for inner-shell ionization S_i is given by Eq. (24) with $\xi = 2$, the total number of electrons in the $1s^2$ shell and χ the ionization energy of the $1s^2$ shell in ion $Z^{+(z-1)}$ and where C_{II} is the fluorescence yield (= probability of emission of a photon per ionization).

Mewe & Schrijver (1975, 1978a,b) have argued that inner-shell ionization of a Li-like ion is an additional mechanism in populating the metastable state of a He-like ion by the process

$$Z^{+(z-1)}(1s^2 2s \ ^2S) + e^- \rightarrow Z^{+z}(1s2s \ ^3S) + 2e^- \ , \tag{110}$$
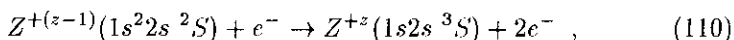
which can give a significant contribution to the formation of the forbidden He-like (z) $2^3S \rightarrow 1^1S$ line in a transient plasma (Mewe & Schrijver 1975, 1978b, 1980). In this case $C_{II} = 0.75$ for a low-density plasma.

15.4 Diagnostics

The diagnostic techniques based on the measurement of satellite to resonance line intensity ratios in high-resolution X-ray spectra from hot plasmas provide powerful tools for the determination of electron *temperature*, electron *density* (see above), *departures from steady-state ionization* balance (in transient plasmas), or *departures from Maxwellian energy* distributions (in non-thermal plasmas). As an example, I briefly consider the illustrative case of the He-like Fe XXV resonance line (w) at 1.85 Å with the satellites in the Li-like ion (e.g., the prominent DR satellite j and the IE satellite q, see Fig. 14) (for notations and details, e.g., Gabriel 1972, and Mewe 1988).

From the formulae given above and in Sect. 8, the relative intensities of the resonance (w), DR satellite (j), and IE satellite (q) lines can be approximately written as:
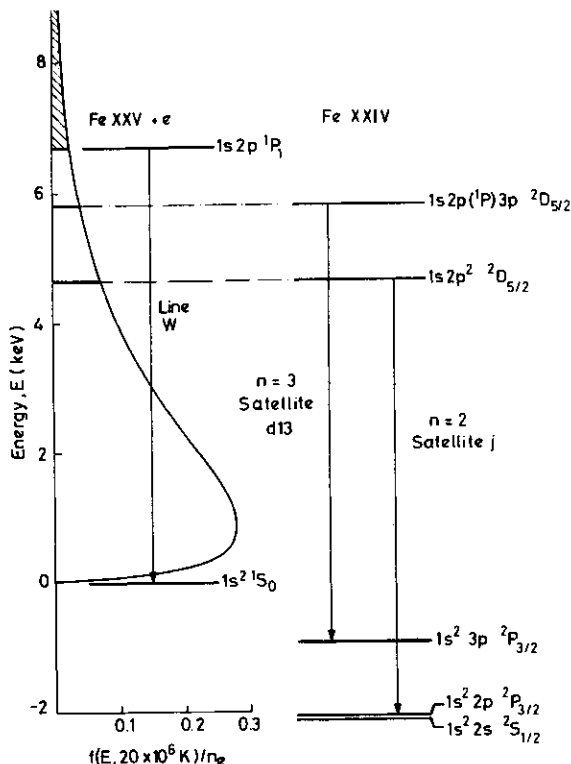
Fig. 15. Energy level diagrams for Fe XXIV and Fe XXV $+ e^-$ with line transitions w, j and $d13$ indicated. The normalized free-electron Maxwellian energy distribution, $f(E)/n_e$, is shown for a typical flare temperature of 20×10^6 K (after Gabriel & Phillips 1979).

$$I_w \propto n_e\, N_{\text{He}}\, T^{-1/2}\, e^{-E_0/kT},$$
$$I_j \propto n_e\, N_{\text{He}}\, T^{-3/2}\, e^{-E_s/kT},$$
$$I_q \propto n_e\, N_{\text{Li}}\, T^{-1/2}\, e^{-E_e/kT}, \tag{111}$$

where N_{He} and N_{Li} are the densities of He- and Li-like ions determined by the ionization balance, and the excitation energies are E_0, E_s, and E_e (note that $E_0 \simeq 1.4 E_s \simeq E_e$).

15.4.1 Temperature diagnostics. The DR satellite/resonance line ratio

$$j/w \propto T^{-1}\, e^{0.3E_w/kT} \tag{112}$$

determines the electron *temperature*, independently of the electron density and the ionization balance.

15.4.2 Ionization balance diagnostics. On the other hand, the IE satellite/resonance line ratio

$$q/w \propto N_{\mathrm{Li}}/N_{\mathrm{He}} \qquad (113)$$

determines the *ion abundance ratio* Li/He, independently of temperature.

It has been common after Gabriel (1972) to describe the derived abundance ratio by the so-called "ionization" temperature, T_z, i.e. the value of the electron temperature for which in ionization equilibrium, the actual ratio $N_{\mathrm{Li}}/N_{\mathrm{He}}$ is equal to that determined from the measured line ratio ($T = T_z$). With T and T_z derived from such line ratios, departures from ionization equilibrium in a transient plasma can be deduced, $T > T_z$ indicating an ionizing plasma, and $T < T_z$ a recombining plasma.

15.4.3 Non-Maxwellian electron velocity distributions. Departures from a Maxwellian velocity distribution can occur when energy is deposited into (or lost from) the high-energy tail of the distribution at a rate much faster than the Coulomb electron-electron collision rate $t_{\mathrm{ee}}^{-1} \sim 100 n_e T^{-3/2}$ s^{-1}, resulting in a high-energy excess (or deficit, respectively). Even when the Coulomb collision rate is too slow, plasma instabilities may cause a relaxation towards a Maxwellian distribution in a much shorter time as is probably the case in the shocks in supernova remnants (SNRs). Non-Maxwellian distributions are most likely to occur in low-density plasmas and at high velocities where collisional relaxation is slow, or in plasmas confined by strong magnetic fields that inhibit the dissipation process. As the electrons in the high-energy tail are just the ones which excite and ionize ions, the excitation and ionization rates are most strongly affected, whereas recombination rates which rely mostly on the electrons in the bulk of the distribution are not significantly affected. However, Itoh (1984b) showed that in the early stages of ionization in the shocks of SNRs the electron population can consist of primary shock-heated electrons plus cooler secondary electrons ejected during the ionization process that cause an enhanced recombination rate and slowing down of the ionization process. This in turn can lead to an underestimate of the age of the SNR (cf. Kaastra 1998).

A deficit of high-energy electrons could arise if the fast electrons lose their energy by exciting or ionizing ions more rapidly than Coulomb collisions shuffle electrons from the bulk of the energy distribution (energy $\sim kT$) to the tail (e.g., Dreicer 1960). The reverse, i.e., the production of a high-energy excess in the tail, may occur in plasmas with a steep temperature gradient where fast electrons can penetrate into cooler regions of the plasma, e.g., in the solar wind (Owocki & Scudder 1983) or in solar flares (Seely et al. 1987).

Various diagnostics can be applied to obtain constraints on the shape of the electron energy distribution: (1) measurements of spectral lines from a number of ion charge stages with a range in ionization thresholds; (2) measurement of the polarization of lines or continuum which is quite sensitive

to the presence of electron beams in plasmas; (3) measurements of spectral lines that are excited by different parts of the electron distribution.

For the second method I refer to Pal'chikov & Shevelko (1995) who discuss the theory of polarization of X-ray lines and give many references to crossed-beam experiments and solar spectral measurements. Here I consider the technique of measuring the ratio of two spectral lines that are excited by different portions of the electron energy distribution.

It is generally admitted that energetic non-thermal electrons are responsible for the hard X-ray bursts occurring in the impulsive phase of flares, which may enhance the high-energy tail (e.g. > 10 keV) of the Maxwellian distribution of the emitting background plasma, and as a consequence this may result in an enhancement of the resonance line intensity relative to the DR satellite intensities. This is connected with the resonant character of the DR process as is illustrated in Fig. 15 showing the energy level diagrams for the He-like Fe XXV resonance line w and its DR Li-like satellites j and $d13$. A DR satellite is produced only by free electrons having an energy exactly equal to [within the small autoionization width δE_ζ, see Eq. (62)] the excitation energy E_s of the satellite line level, whereas the resonance line (w) can be excited by all electrons having any energy above the threshold value E_0 [$\simeq 1.4E_s$ (or $\simeq 1.16E_s$) for $n = 2$ (or 3) satellites]. Therefore the appearance of an enhanced high-energy tail in the distribution will result in an increase of the resonance line but will have no effect on the satellite lines. As a consequence, the satellite/resonance ratio decreases giving larger values of the apparent electron temperature. On the other hand, the ratio of two $n = 2$ and $n = 3$ satellites remains unaffected, but gives a measure of the actual temperature referring to the Maxwellian part of the electron energy distribution. Gabriel & Phillips (1979) have developed such a detection method using the Fe XXV resonance line and two strong $n = 2$ (j) and $n = 3$ ($d13$) satellites (Fig. 15). Seely et al. (1987) have applied this method to high-resolution spectra measured with the SOLFLEX spectrometer onboard the *P78-1* spacecraft from several solar limb flares. They have found that non-thermal electron energy distributions occur during the first few minutes of the impulsive phase, near the time when hard X-ray bursts are observed at the onset of the flare. For the discrete electron energies (4.7 and 5.8 keV) at which the j and $d13$ satellites are formed, the electron energy distributions were observed to have a bump or to be flat at this time.

15.4.4 Line and continuum emission for non-thermal distributions.

Line emission

As an illustration I compare the intensities of dielectronic recombination (DR) and inner-shell excitation (IE) lines for various normalized[12] electron energy distributions $f(E)$: a Maxwell (M), a power law (PL), and a mono-energetic (ME) distribution. The Maxwell distribution is given by Eq. (20) and the power law distribution is given by:

$$f_{PL}(E) = (\delta - 1)E_1^{\delta-1}E^{-\delta} \ (E \geq E_1), \text{or } f_{PL}(E) = 0 \ (E < E_1) \ , \quad (114)$$

where we assume $\delta > 1$. The mono-energetic distribution is:

$$f_{ME}(E) = (\Delta E)^{-1} \quad (115)$$

in a small energy interval ΔE around electron energy $E = E_m$.

For an arbitrary electron energy distribution the intensity of a DR satellite line with excitation energy E_s is given by

$$I^{DR} = \left(\frac{2E_s}{m_e}\right)^{1/2} \frac{h^3}{16\pi m_e} \frac{f(E_s)}{E_s} \ \beta \ , \quad (116)$$

where $\beta = N_{z+1}n_e B_s$ [cf. Eq. (107)]. Inserting the numerical constants, expressing now energies and temperature T in keV we obtain for the line intensity in phot cm^{-3} s^{-1} for the Maxwellian distribution:

$$I_M^{DR} = 5.24 \ 10^{-27} \ T^{-3/2}e^{-E_s/T}\beta \ . \quad (117)$$

For the power law distribution:

$$I_{PL}^{DR} = 4.64 \ 10^{-27} \ (\delta - 1)E_1^{\delta-1}E_s^{-\delta-\frac{1}{2}}\beta \ , \quad (118)$$

where $E_s > E_1$.
For a mono-energetic distribution:

$$I_{ME}^{DR} = 4.64 \ 10^{-27} \ (\Delta E)^{-1}E_s^{-1/2}\beta \ , \quad (119)$$

where $E_m = E_s$, and the autoionization width $\delta E_\zeta \ll \Delta E$.

For an IE line (or similarly for the resonance line) with excitation energy E_0 we obtain from Eqs (108) and (68) with the approximation for the Gaunt factor $g(E) \approx 0.1 + 0.276 \ln U$ $(U = E/E_0)$ for the Maxwell distribution:

$$I_M^{IE} = 5.0 \ 10^{-10} \ T^{-1/2}E_0^{-1}f \ \bar{g}_M \ e^y \ \gamma \ , \quad (120)$$

where $\bar{g}_M = 0.1+0.276e^y E_1(y)$ with $y = E_0/T$, $E_1(y)$ the exponential integral (Eq. 71), f the oscillator strength, and $\gamma = N_z n_e B R_s$. Again energies and T are in keV.

---

[12] $\int_{E_1}^{\infty} f(E)\,dE = 1$; $E_1 = 0$ for the Maxwell distribution.

We can integrate the excitation cross section over a power law distribution using Eqs (19) and (114) and derive:

$$I_{\text{PL}}^{\text{IE}} = 4.43 \ 10^{-10} \ \left(\frac{\delta - 1}{\delta - \frac{1}{2}}\right) E_1^{-1/2} E_0^{-1} f \ \bar{g}_{PL} \ \gamma \ , \tag{121}$$

where $\bar{g}_{\text{PL}} = 0.1 + 0.276[\ln(E_1/E_0) + (\delta - \frac{1}{2})^{-1}]$, and $E_1 > E_0$.

For the mono-energetic distribution:

$$I_{\text{ME}}^{\text{IE}} = 4.43 \ 10^{-10} \ E^{-1/2} E_0^{-1} f \ g_{\text{ME}} \ \gamma \ , \tag{122}$$

where $g_{\text{ME}} = g(E)$ and $E > E_0$.

Continuum emission

As an example I consider only ff emission and follow essentially the treatment of Brown (1971) who calculated the electron-proton bremsstrahlung spectrum for a power law distribution of non-thermal electrons in a solar flare. The ff emissivity at photon energy ε (in photons/sec per unit volume and per unit ε) for electron-ion (i) encounters can be written for an arbitrary electron distribution as:

$$P^{\text{ff}}(\varepsilon) = n_e n_i Z_i^2 \int_\varepsilon^\infty \sqrt{\frac{2E}{m_e}} Q(\varepsilon, E, Z_i) f(E) \, dE \ , \tag{123}$$

where the cross section (area per unit ε) is written as:

$$Q(\varepsilon, E, Z_i) = \left(\frac{C}{\varepsilon E}\right) \ g(\varepsilon, E, Z_i) \ , \tag{124}$$

where Z_i is the ion charge and

$$C = \frac{8\pi}{3\sqrt{3}} \alpha r_0^2 m_e c^2 \tag{125}$$

and where $r_0 = 2.8179 \ 10^{-13}$ cm is the classical electron radius, $\alpha = 1/137.04$ the fine-structure constant, and $g(\varepsilon, E, Z_i)$ is the Gaunt factor. Brown (1971) uses the Born-Heitler non-relativistic high-energy approximation

$$g(\varepsilon, E, Z_i) = \frac{\sqrt{3}}{\pi} \ln \left[\frac{1 + \sqrt{1 - \varepsilon/E}}{1 - \sqrt{1 - \varepsilon/E}}\right] \ . \tag{126}$$

The Born Gaunt factor becomes zero at threshold $\varepsilon = E$, whereas it should assume here a finite value (cf. Karzas & Latter 1961). On the basis of the results of Karzas & Latter I have corrected for this effect and averaged g for each ion over a power-law electron distribution (Eq. 114) assuming $\varepsilon > E_1$:

$$\bar{g}(\varepsilon, \delta, Z_i) = \left(\delta - \frac{1}{2}\right) \varepsilon^{\delta - \frac{1}{2}} \int_\varepsilon^\infty E^{-\delta - \frac{1}{2}} g(\varepsilon, E, Z_i) \, dE \tag{127}$$

Moreover, I calculated a total Gaunt factor G_{PL} by summing over all ions (i) in the plasma in a similar way as we did before (cf. Eq. 88) (Brown considered only protons and took $Z_i = 1$). We express all energies in keV, inserting all physical constants into C, take $m_e c^2 = 511.0$ keV then we obtain $C = 1.4321 \ 10^{-24}$, and take $\sqrt{2E/m_e} = 1.8755 \ 10^9 \sqrt{E}$. Integration of Eq. (123) yields finally for the free-free emissivity in phot cm^{-3} s^{-1} keV^{-1}:

$$P_{PL}^{ff}(\varepsilon) = 2.686 \ 10^{-15} G_{PL} \left(\frac{\delta - 1}{\delta - \frac{1}{2}}\right) \left(\frac{E_1}{\varepsilon}\right)^{\delta - 1} \varepsilon^{-3/2} n_e N_H \ . \qquad (128)$$

Comparing this formula with the corresponding one for a Maxwell distribution (Eq. 92) we find comparable results only when $\varepsilon \sim T$ and $\varepsilon \sim E_1$.

For a mono-energetic distribution ($E = \varepsilon$) we obtain:

$$P_{ME}^{ff}(\varepsilon) = 2.686 \ 10^{-15} G_{PL} \ \varepsilon^{-3/2} \ n_e N_H \ . \qquad (129)$$

The total Gaunt factors are of order unity and our calculations approximately give $G_{PL} \sim 2\varepsilon^{-0.13}\delta^{-0.33}$ and $G_{ME} \sim \varepsilon^{-0.3}$ for $\varepsilon \sim 1$–20 keV and $\delta \sim 2$–5. Finally, I have estimated that relativistic effects are less than about $15(\varepsilon/50)\%$, e.g., $\lesssim 15\%$ for $\varepsilon \lesssim 50$ keV.

16   Comparison of Calculated Spectra and Accuracy

Raymond (1988) has compared various spectral calculations and discussed the differences resulting from different ionization balance calculations and from different treatments of the line excitation. He comes to the conclusion that for the strongest X-ray lines from astrophysical plasmas, those of the H- and He-like ions, the agreement generally approaches about 20% (which is important because the He-like lines can be used for density diagnostics), whereas for other cases (e.g., iron lines around 10-12 Å and silicon and sulphur lines around 40-50 Å) discrepancies of a factor of two may exist.

The ionization balance strongly determines the overall appearance of the X-ray spectra. Mewe (1990) has made a few spectral calculations using different ionization balance calculations for a spectral resolution of 0.05 Å, typical for the high-resolution spectrometers to be flown on the *AXAF* and *XMM* missions (see the Chapter by Paerels). The use of different ionization balances may lead to appreciable differences in the derived plasma parameters as has been recently shown by Masai (1997) in an analysis of simulated *ASCA* spectra.

Raymond (1988, 1990) has made an attempt to test the existing models by comparing with high-resolution solar X-ray observations. From his comparison of a model calculation with the composite X-ray spectrum of a solar flare he concludes that uncertainties in atomic rates or the breakdown of simplifying model assumptions may lead to errors on the order of ~50 % in the predicted line strengths. A comparison of coronal models with *EXOSAT*

(Lemen et al. 1989) and *EUVE* (Mewe et al. 1995b; Schrijver et al. 1995) spectral X-ray observations with moderate resolution ($\sim$3 Å) of a few late-type stars by using differential emission measure distributions show a satisfactory agreement, but also indicate that for the interpretation of the future *AXAF* and *XMM* X-ray spectra better spectral model calculations will be needed.

Kaastra & Mewe have started a major undertaking to revise and extend all atomic data used in the current MEKAL code (cf. Sect. 3.2) to meet the demands of the analysis of the future data. This project includes a systematic search through the literature and a critical evaluation of the data used. A comparison of new and old data for the H-sequence (e.g., the $n \rightarrow 1$ transitions) shows that for the most important temperature ranges the newly calculated collision strengths are accurate to $\sim$10% for the Lyman α (2–1) transitions, but for Lyman β (3–1) and Lyman γ (4–1) the differences can be up to 40–70%, especially near threshold (low temperature) where resonance effects are important (cf. Kaastra 1998).

17   Summary

High-resolution X-ray spectroscopy has applications to a wide range of optically thin hot astrophysical and laboratory plasmas. Its significance as a tool in understanding the physics of these sources depends on the reliability of the theoretical models used to interpret the spectra. We have considered the coronal model in describing the ionization and excitation of hot plasmas. In particular, we have discussed the processes of ionization, recombination and excitation, including the formation of dielectronic recombination satellite lines. The accuracy with which the emergent X-ray spectrum can be predicted has been briefly considered. Various effects leading to deviations from the coronal model such as high density, optical depth, transient ionization, and non-Maxwellian electron distributions, have been discussed. It is obvious that the complexity of plasma physics and the atomic parameters involved are such that a sound verification of plasma theories and atomic physics which are applied will be required for the interpretation of future high-resolution spectra such as can be obtained with the future space missions *AXAF*, *XMM*, and *ASTRO-E*.

References

Abramowitz, M. & Stegun, I.A. (1970): *Handbook of Math. Functions*, (9th Ed., Dover)
Acton, L.W. & Brown, W.A. (1978): ApJ 225, 1065

Aggarwal, K.M., Berrington, K., Eissner, W. & Kingston, A.E. (1986): Report on Recommended Data, Atomic Data Workshop, Daresbury Lab.

Aggarwal, K.M. & Kingston, A.E. (1991): J. Phys. B 24, 4583

Aldrovandi, S.M.V. & Péquignot, D. (1973): A&A 25, 137; erratum 47, 321 (1976)

Allen, C.W. (1973): *Astrophys. Quantities* (3rd ed., The Athlone Press, London)

Anders, E. & Grevesse, N. (1989): Geochim. Acta 53, 197

Arnaud, M. & Raymond, J.C. (1992): ApJ 398, 394

Arnaud, M. & Rothenflug, R. (1985): A&AS 60, 425

Bates, D.R. & Dalgarno (1962): in *Atomic and Molecular Processes*, Ed. D.R. Bates, Academic Press Inc., New York, p. 245

Bates, D.R., Kingston, A.E. & McWhirter, R.W.P. (1962a): Proc. Roy. Soc. (London) A 267, 297

Bates, D.R., Kingston, A.E. & McWhirter, R.W.P. (1962b): Proc. Roy. Soc. (London) A 270, 155

Bell, R.H. & Seaton, M.J. (1985): J. Phys. B.: At. Mol. Phys. 18, 1589

Bely, O. & van Regemorter, H. (1970): ARA&A 8, 329

Bely-Dubau, F., Gabriel, A.H. & Volonté, S. (1979): MNRAS 189, 801

Blaha, M. (1971): Bull. Am. Astron. Soc. 3, 246

Brown, J.C. (1971): Solar Phys. 18, 489

Burgess, A. (1964): ApJ 139, 776

Burgess, A. (1965): ApJ 141, 1588

Burgess, A. et al. (1977): MNRAS 179, 275

Burgess, A. & Chidichimo, M.C. (1983): MNRAS 203, 1269

Burgess, A. & Summers, H.P. (1969): ApJ 157, 1007

Burgess, A. & Tworkowski, A.S. (1976): ApJ 205, L105

Butler, S.E. & Dalgarno, A. (1980): ApJ 241, 838

Carson, T.R. (1988): A&A 189, 319

Condon, E.U. & Shortley, G.H. (1970): *The Theory of Atomic Spectra*, Cambridge University Press, U.K., 9th ed.

Cooper, J. (1966): Rep. Progr. Phys. 29, 35

Dalgarno, A. & Drake, G.W.F. (1969): in *Les Transitions Interdites dans les Spectres des Astres*, Les Congrès et Colloques de l'Université de Liège, Belgium Vol. 54, p. 69

Dolder, K. & Peart, B. (1986): Adv. At. Mol. Phys. 22, 197

Drawin, H.-W. (1961): Z. Physik 164, 513; 168, 238

Dreicer, H. (1960): Phys. Rev. 117, 343

Dubau, J. & Volonté, S. (1980): Rep. Prog. Phys. 43, 199

Düchs, D. & Griem, H.R. (1966): Phys. Fluids 9, 1099

Dunford, R.W., Church, D.A. & Liu, C.J. et al. (1990): Phys. Rev. A 41, 4109

Edlén, B. & Tyrén, F. (1939): Nature 143, 940

Elwert, G. (1952): Z. Naturf. 7a, 432; 703

Fabian, A.C. & Ross, R.R. (1981): MNRAS 195, 29P

Feldman, U. (1981): Physica Scripta 24, 681

Gabriel, A.H. & Jordan, C. (1972): *Case Studies in Atomic and Collisional Physics* 2, Eds E.W. McDaniel & M.R.C. McDowell, N.-H. Publ. Co., Amsterdam, p. 209

Gabriel, A.H. (1972): MNRAS 160, 99

Gabriel, A.H. & Phillips, K.J.H. (1979): MNRAS 189, 319

Gallagher, J.H. & Pradhan, A.K. (1985): JILA Data Center Report No. 30 (JILA, Univ. of Colorado, Boulder)

Gaunt, J.A. (1930): Proc. Roy. Soc. (London), Ser. A 126, 654

Gregory, D.C. et al. (1987): Phys. Rev. A 34, 3657; A 35, 3526

Griem, H.R. (1964): *Plasma Spectroscopy*, McGraw-Hill, New York; Univ. Microfilms Internatl. 212 00000 7559, Ann Arbor, Mich.

Griem, H.R. (1988): *Principles of Plasma Spectroscopy*, Cambridge Monographs on Plasma Physics 2, Cambridge Univ. Press, Cambridge, UK

Griem, H.R. (1997): J. Quant. Spectr. Rad. Transf. 40, 403

Gronenschild, E.H.B.M. & Mewe, R. (1978): A&AS 32, 283

Gronenschild, E.H.B.M. & Mewe, R. (1982): A&AS 48, 305

Güdel, M., Guinan, E.F. & Mewe, R. et al. (1997): ApJ 479, 416

Hahn, Y. (1985) : Adv. At. Mol. Phys. 21, 123

Hahn, Y. et al. (1980): J. Quant. Spectr. Rad. Transf. 23, 65

Hahn, Y. & LaGattuta, K.J. (1988): Phys. Rep. 166, 195

Hamilton, A.J.S., Sarazin, C.L.S. & Chevalier, R.A. (1983): ApJS 51, 115

Hearn, A.G. (1966): Proc. Phys. Soc. 88, 171

Herzberg, G. (1944): *Atomic Spectra & Atomic Structure*, Dover Publications, New York, 2nd Ed.

Holt, S. & McCray, R. (1982): ARA&A 20, 323

Huaguo Teng, Baifei Sheng, Wengqi Zhang & Zhizhan Xu (1994a): Phys. Scr. 49, 463

Huaguo Teng, Baifei Sheng, Wengqi Zhang & Zhizhan Xu (1994b): Phys. Scr. 49, 468

Huaguo Teng, Baifei Sheng, Wengqi Zhang & Zhizhan Xu (1994c): Phys. Scr. 49, 696

Huaguo Teng, Baifei Sheng, Wengqi Zhang & Zhizhan Xu (1994d): Phys. Scr. 50, 55

Huaguo Teng & Zhizhan Xu (1996): J. Quant. Spectr. Rad. Transf. 56, 443

Itikawa, Y. (1991): At. Data Nucl. Data Tables 49, 209

Itikawa, Y., Kato, T. & Sakimoto, K. (1995): The Inst. of Space and Astronautical Sc. Report No. 657 (Kanagawa, Japan)

Itikawa, Y., Takayanagi, K. & Iwai, T. (1984): At. Data Nucl. Data Tables 31, 215

Itoh, H. (1984a): Physica Scripta T7, 19

Itoh, H. (1984b): ApJ 285, 601

Jacobs, V.L. et al. (1977): ApJ 211, 605; 215, 690

Kaastra, J.S. (1992): *An X-ray spectral code for optically thin plasmas*, Internal SRON-Leiden report, version 2.0.

Kaastra, J.S. (1998): in *The Hot Universe*, Eds M. Itoh, S. Kitamoto & K. Koyama, Proc. IAU Symp. No. 188, Kluwer Academic Publishers, p. 43

Kaastra, J.S. & Jansen, F.A. (1993): A&AS 97, 873

Kaastra, J.S. & Mewe, R. (1993): Legacy 3 (Journal of HEASARC, NASA/GSFC (Greenbelt), p. 16

Kaastra, J.S. & Mewe, R. (1998): in preparation

Kaastra, J.S., Mewe, R. & Liedahl, D.A. et al. (1996): A&A 314, 547

Kaastra, J.S., Mewe, R. & Nieuwenhuijzen, H. (1996): in *UV and X-ray Spectroscopy of Astrophysical and Laboratory Plasmas*, (Eds. K. Yamashita & T. Watanabe, Universal Academy Press, Inc., Tokyo, p. 411

Kahn, S.M. & Liedahl, D.A. (1995): in *Physics with Multiply Charged Ions*, Ed. D. Liesen, NATO Advanced Study Institute Series, Plenum Press, New York, p. 169

Kallman, T.R. & McCray, R. (1982): ApJS 50, 263

Karim, K.R. & Bhalla, C.P. (1988): Phys. Rev. A 37, 2599

Karim, K.R. & Bhalla, C.P. (1989): Phys. Rev. A 39, 3548

Karzas, W.J. & Latter, R. (1961): ApJS 6, 167

Kato, T., Masai, K. & Arnaud, M. (1991): Research Report Nucl. Inst. Fusion Science-Data Ser. No. 14

Keenan, F.P. (1992): in *UV and X-ray Spectroscopy of Astrophysical and Laboratory Plasmas*, Eds E.H. Silver & S.M. Kahn, Cambridge University Press, Cambridge, p. 44

Keenan, F.P. (1995): Space Sc. Rev. 75, 537

Kingston, A.E. & Tayal, S.S. (1983): J. Phys. B. 16, 3465

Kramers, H.A. (1923): Philos. Mag. J. Sci. 46, 836

Kunze, H.-J. (1972): Space Sci. Rev. 13, 565

Kylafis, N.D. & Lamb, D.Q. (1982): ApJS 48, 239

Landini, M. & Monsignori Fossi, B.C. (1990): A&AS 82, 229

Lang, J. (ed.) (1994): At. Data Nucl. Data Tables 57, 1-332

Lemen, J.R., Mewe, R., Schrijver, C.J. & Fludra, A. (1989): ApJ 341, 474

Lemen, J.R. et al. (1986): J. Appl. Phys. 60 (6), 1960

Liedahl, D.A., Kahn, S.M., Osterheld, A.L. & Goldstein, W.H. (1991): ApJ 350, L37

Liedahl, D.A., Osterheld, A.L. & Goldstein, W.H. (1995): ApJ 438, L115

Lightman, A.P., Lamb, D.Q. & Rybicki, G.B. (1981): ApJ 248, 738

Lin, C.D., Johnson, W.R. & Dalgarno, A. (1977): Phys. Rev. A 15, 154

Lotz, W. (1968): Z. Physik 216, 441

Masai, K. (1984): Ap&SS 98, 367

Masai, K. (1994a): ApJ 437, 770

Masai, K. (1994b): J. Quant. Spectr. Rad. Tranf. 51, 211

Masai, K. (1997): A&A 324, 410

Mason, H.E. & Monsignori Fossi, B.C. (1994): A&AR 6, 123

Massey, H.S.W. & Bates, D.R. (1942): Rep. Progr. Phys. 9, 62

McCray, R. (1984): Physica Scripta T7, 73

McWhirter, R.W.P. (1965): in *Plasma Diagnostic Techniques*, Eds R.H. Huddlestone & S.L. Leonard, Acad. Press, New York, p. 201

McWhirter, R.W.P. & Hearn, A.G. (1963): Proc. Phys. Soc. 82, 641

Merts, A.L., Cowan, R.D. & Magee, N.H. (1976): Los Alamos Sci. Lab. Rep. LA-6220-MS

Mewe, R. (1967): Brit. J. Appl. Phys. 18, 107

Mewe, R. (1970): Z. Naturf. 25a, 1798

Mewe, R. (1972): A&A 20, 215

Mewe, R. (1984): Physica Scripta T7, 5

Mewe, R. (1988): in *Astrophysical and Laboratory Spectroscopy*, Eds R. Brown & J. Lang, Scottish Univ. Summer School in Phys. Publ. 33, p. 129

Mewe, R. (1990): in *Physical Processes in Hot Cosmic Plasmas*, Eds W. Brinkmann, A.C. Fabian & F. Giovanelli, Kluwer Acad. Publ., Dordrecht-Holland, p. 39

Mewe, R. (1991): A&AR 3, 127

Mewe, R. (1992): in *The Physics of Chromospheres, Coronae and Winds*, Eds C.S. Jeffery & R.E.M. Griffin, Cambridge University Printing Service, p. 33

Mewe, R. & Gronenschild, E.H.B.M. (1981): A&AS 45, 11

Mewe, R., Gronenschild, E.H.B.M. & van den Oord, G.H.J. (1985a): A&AS 62, 197

Mewe, R. & Kaastra, J.S. (1994): European Astron. Soc. Newsletter 8, p. 3

Mewe, R., Kaastra, J.S. & Liedahl, D.A. (1995a): Legacy 6, 16

Mewe, R., Kaastra, J.S., Schrijver, C.J., van den Oord, G.H.J. & Alkemade, F.J.M. (1995b): A&A 296, 477

Mewe, R., Kaastra, J.S., White, S.M. & Pallavicini, R. (1996): A&A 315, 170

Mewe, R., Lemen, J.R. & van den Oord, G.H.J. (1986): A&AS 65, 511

Mewe, R., Lemen, J.R., Peres, G. et al. (1985b): A&AS 152, 229

Mewe, R., Lemen, J.R. & Schrijver, C.J. (1991): Ap&SS 182, 35

Mewe, R. & Schrijver, J. (1975): Astrophys Space Sci. 38, 345

Mewe, R. & Schrijver, J. (1978a): A&A 65, 99

Mewe, R. & Schrijver, J. (1978b): A&A 65, 115

Mewe, R. & Schrijver, J. (1978c): A&AS 33, 311

Mewe, R. & Schrijver, J. (1980): A&A 87, 261

Mewe, R., Schrijver, J. & Sylwester, J. (1980): A&AS 40, 323

Milne, E.A. (1924): Philos. Mag. J. Sci. 47, 209

Moores, D.L. (1988): in *Astrophysical and Laboratory Spectroscopy*, Eds R. Brown & J. Lang, Scottish Univ. Summer School in Phys. Publ. 33, p. 75

Müller, T. et al. (1987): Phys. Rev. A 36, 599

Munger, C.T. & Gould, H. (1986): Phys. Rev. Lett. 57, 2927

Nussbaumer, H. & Storey, P.J. (1983): A&A 126, 75

Owocki, S.P. & Scudder, J.D. (1983): ApJ 270, 758

Pal'chikov, V.G. & Shevelko, V.P. (1995): *Reference Data on Multicharged Ions:*, Springer-Verlag, Berlin

Peacock, N.J. (1996): Ap&SS 237, 341

Pradhan, A.K. (1985): ApJ 288, 824

Pradhan, A.K. (1987): Physica Scripta 35, 840

Raymond, J.C. (1988): in *Hot Thin Plasmas in Astrophysics*, Ed. R. Pallavicini, Kluwer Acad. Publ., Dordrecht, p. 3

Raymond, J.C. (1990): in *High Resolution X-ray Spectroscopy of Cosmic Plasmas*, Eds P. Gorenstein & M.V. Zombeck, Proc. IAU Coll. 115, Cambridge, U.S.A., Reidel Publ. Co.

Raymond, J.C. & Brickhouse, N.S. (1996): Ap&SS 237, 321

Raymond, J.C. & Smith, B.W. (1977): ApJS 35, 419

Reilman, R.F. & Manson, S.T. (1979): ApJS 40, 815

Romanik, C.J. (1988): ApJ 330, 1022

Ross, R.R. (1979): ApJ 233, 334

Rybicki, G.B. & Lightman, A.P. (1979): *Radiative Processes in Astrophysics:*, Wiley InterSc. Publ., New York

Sampson, D.H. (1982): J. Phys. B 15, 2087

Sampson, D.H., Goett, S.J. & Clark, R.E.H. (1983): At. Data Nucl. Data Tables 29, 467

Sampson, D.H. & Zhang, H.L. (1988): Phys. Rev. A 37, 3765

Schrijver, C.J., Mewe, R., van den Oord, G.H.J. & Kaastra, J.S. (1995): A&A 302, 438

Seaton, M.J. (1959): MNRAS 119, 81

Seaton, M.J. (1962): in *Atomic and Molecular Processes*, Ed. D.R. Bates, Academic Press Inc., New York, p. 414

Seaton, M.J. (1975): Adv. At. Mol. Phys. 11, 83

Seely, J.F., Feldman, U. & Doschek, G.A. (1987): ApJ 319, 541

Shapiro, P.R. & Moore, R.T. (1977): ApJ 217, 621

Smith, B.W. et al. (1985): ApJ 298, 898

Spitzer, L., Jr. (1962): *Physics of Fully Ionized Gases*, 2nd Ed., Intersc. Publ., New York

Spitzer, L., Jr. & Greenstein, J.L. (1951): ApJ 114, 407

Summers, H.P. (1974): MNRAS 169, 663; Appleton Lab. Rep. AL-R-5

Summers, H.P. (1988): in *Astrophysical and Laboratory Spectroscopy*, Eds R. Brown & J. Lang, Scottish Univ. Summer School in Phys. Publ. 33, p. 15

Sylwester, B. et al. (1986): Solar Phys. 103, 67

Unsöld, A. (1955): *Physik der Sternatmosphären:*, 2nd Ed., Springer-Verlag, Berlin

van Regemorter, H. (1962): ApJ 136, 906

Vernazza, J.E. & Raymond, J.C. (1979): ApJ 228, L29

Verner, D.A., &Ferland, G.J. (1996): ApJS 103, 467

Verner, D.A. & Yakovlev, D.G. (1995): A&AS 109, 125

Verner, D.A., Yakovlev, D.G., Band, I.M. & Trzhaskovskaya, M.B. (1993): At. Data Nucl. Data Tables 55, 233

Vrtilek, S.D., McClintock, J.E., Seward, F.D. et al. (1991): ApJS 76, 1127

Wang, J.-S. et al. (1986): Phys. Rev. A 33, 4293

Wang, J.-S. et al. (1987): Phys. Rev. A 36, 951

Wang, J.-S. et al. (1988): Phys. rev. A 38, 4761

Wiese, W.L., Fuhr, J.R. & Deters, T.M. (1996): J. Phys. Chem. Ref. Data, Monograph No. 7

Wilson, R. (1962): J. Quant. Spectr. Rad. Transf. 2, 477

Younger, S. (1981): J. Quant. Spectr. Rad. Transf. 26, 329

Zhang, H.L. & Sampson, D.H. (1987): ApJS 63, 487

Zygelman, B. & Dalgarno, A. (1987): Phys. Rev. A 35, 4085